NEW TRENDS IN BIOMATHEMATICS

Applications in Oncology and Immunology

ONE-DAY WORKSHOP
June 21, 2024, 8:30 a.m.

Aula Magna - Ingegneria "*Italo Falcomatà*"
Università degli Studi Mediterranea
Via R. Zehender, 1 - Reggio Calabria

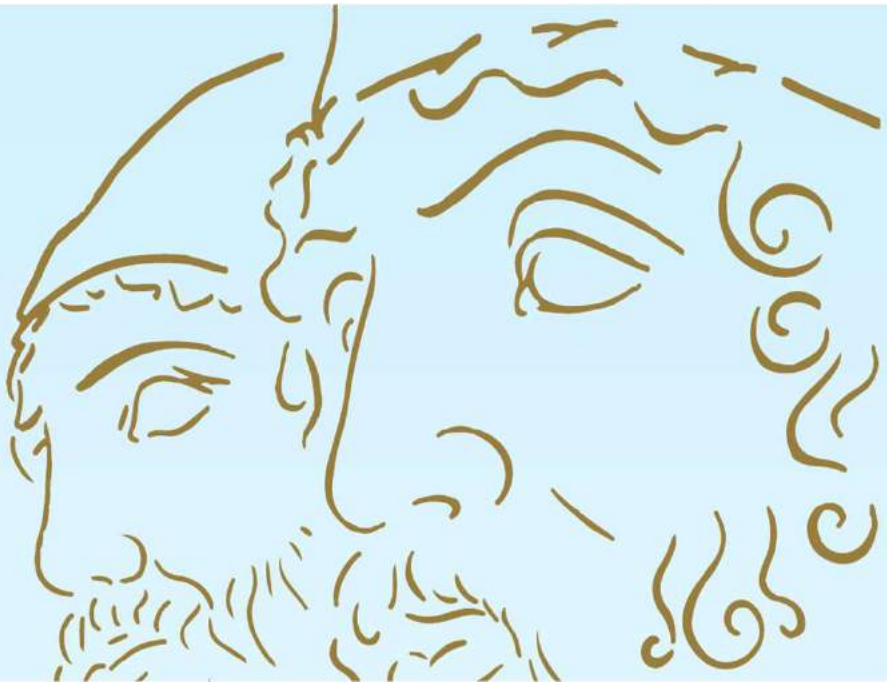

Model and data fusion: physics-driven learning in cancer research

Pasquale Ciarletta

MOX Laboratory, Dept. Mathematics, Politecnico di Milano
CNRS, Sorbonne Université, Paris

MODELLISTICA E CALCOLO SCIENTIFICO
MOX
MODELING AND SCIENTIFIC COMPUTING

POLITECNICO MILANO

OUTLINE

- **Model-based versus Data-based learning in biomedicine**

- **Model and data fusion and physics-driven learning**

  - **multi-scale modeling of glioblastoma in precision oncology**

Model-driven learning in biomedicine: an example

Theory-driven learning in biomedical research has the potential to unveiling the **CAUSALITY** that governs the biological processes. The most successful example is the Hodgkin-Huxley model for cell excitability

Figure 1. The cover of the 1963 Nobel Prize Programme

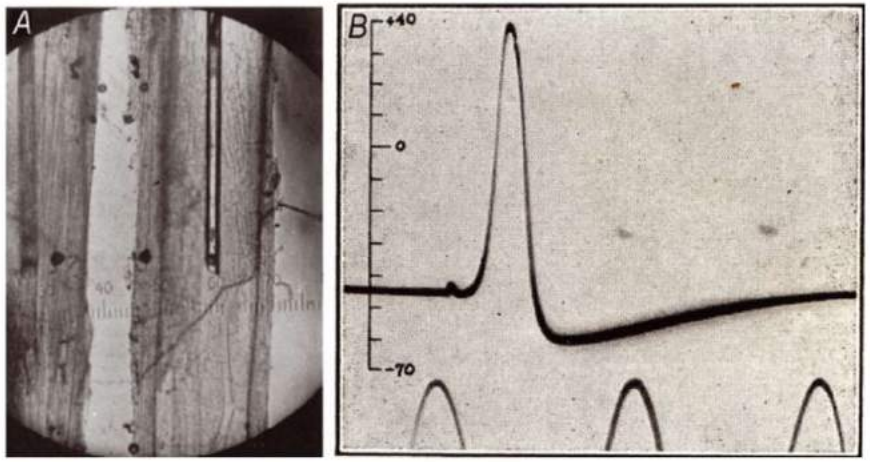

Figure 3. Intracellular recording of the squid giant axon action potential

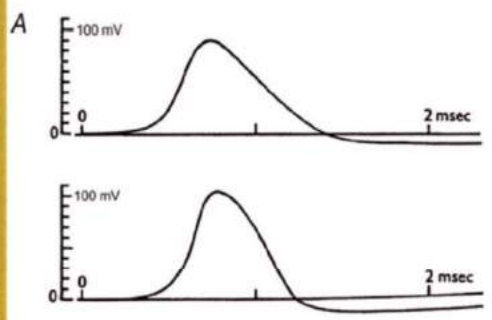

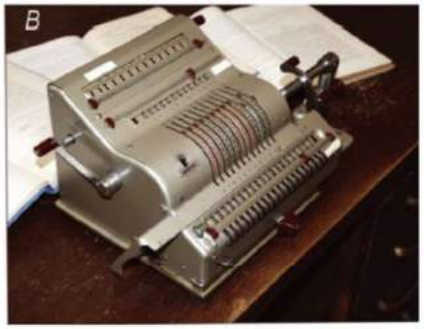

Figure 6. Modelling the action potential

The era of big data and the advent of precision medicine

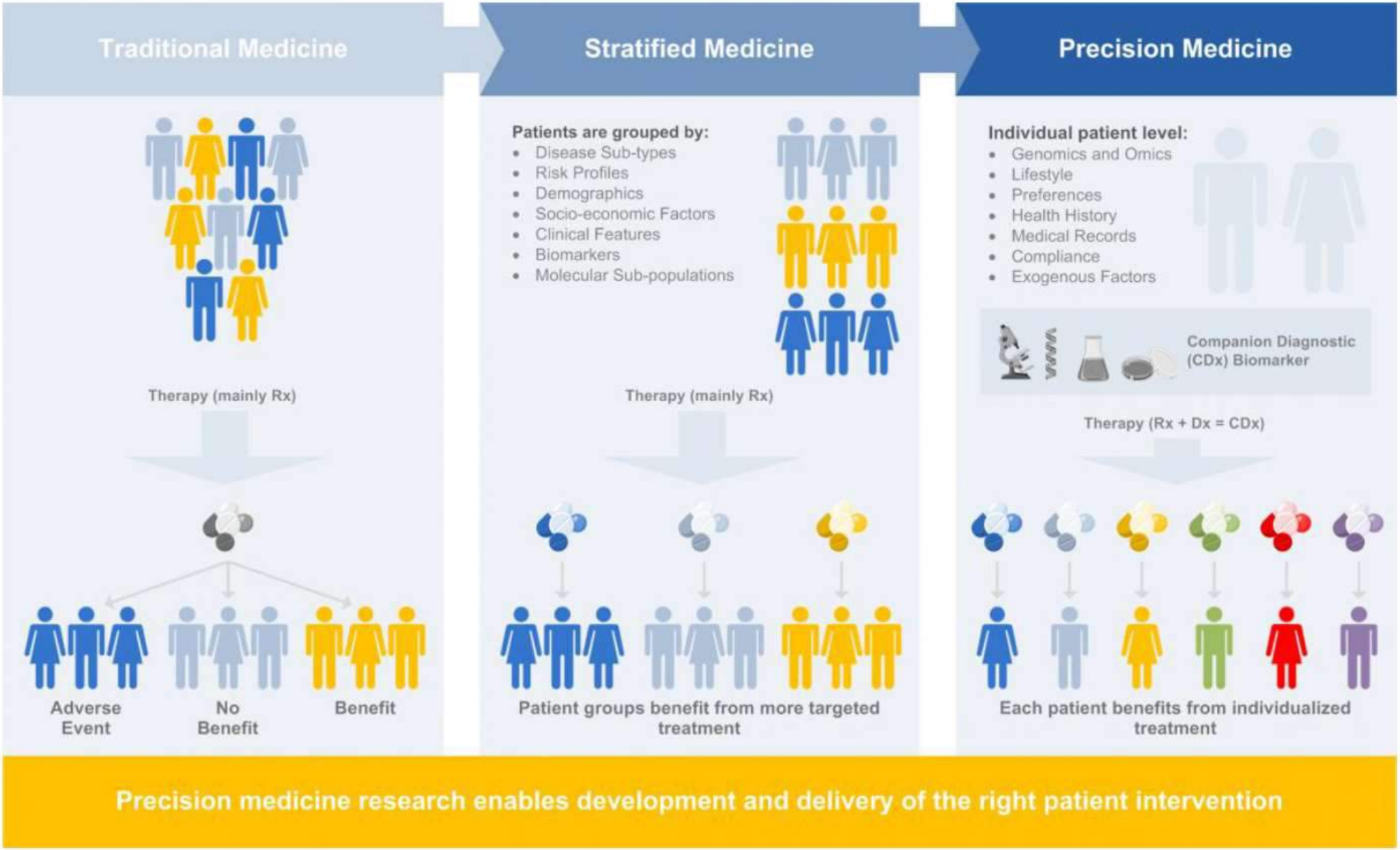

Data-driven learning in biomedicine

Data-driven learning has the objective to infer correlations among big data, that result from different modalities and different level of fidelity. Machine learning is a subfield of AI which uses algorithms to automatically learn insights and recognize patterns from data, applying that learning to make increasingly better decisions

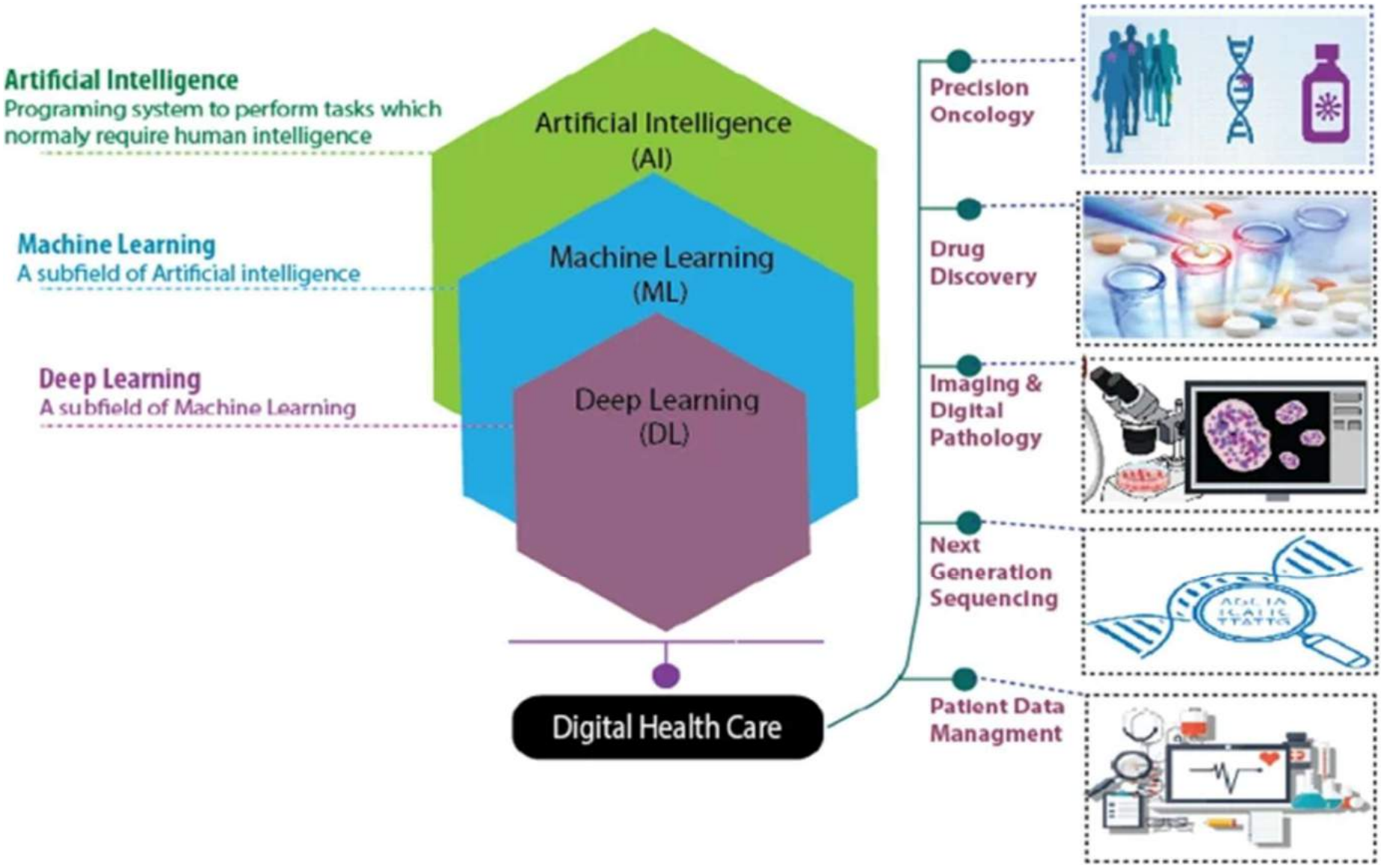

Supervised vs unsupervised learning

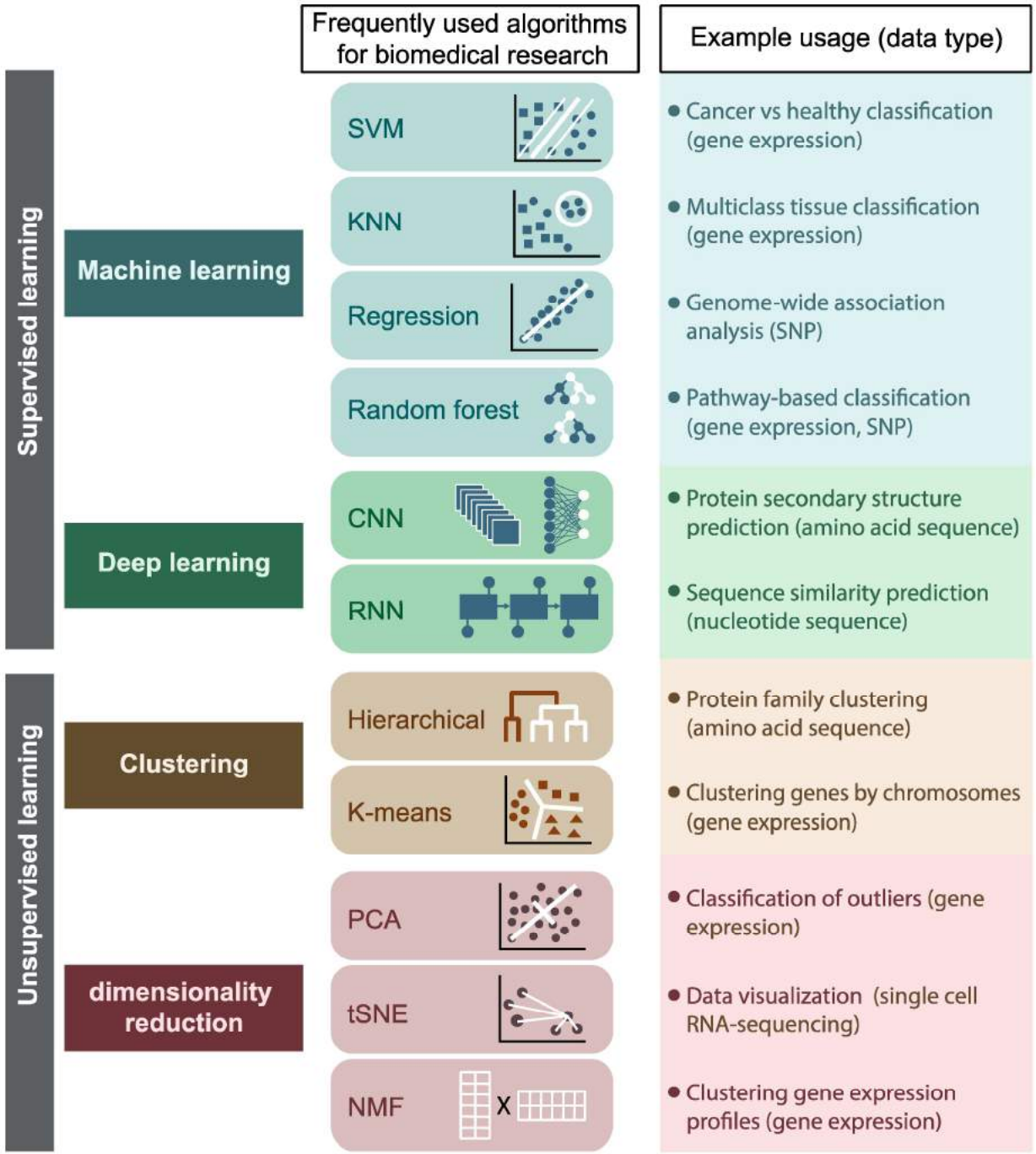

OUTLINE

- Model-based versus Data-based learning in biomedicine

- **Model and data fusion and physics-driven learning**

    - multi-scale modeling of glioblastoma in precision oncology

Integration of ML and multiscale modelling

ML learning alone infers correlations without imposing any law of physics. Multiscale simulations indeed seek to infer the behavior of the system, if we have access to massive amounts of data, while the governing equations/parameters are not precisely known.
Their integration is crucial to build physics-driven knowledge of the biological processes.

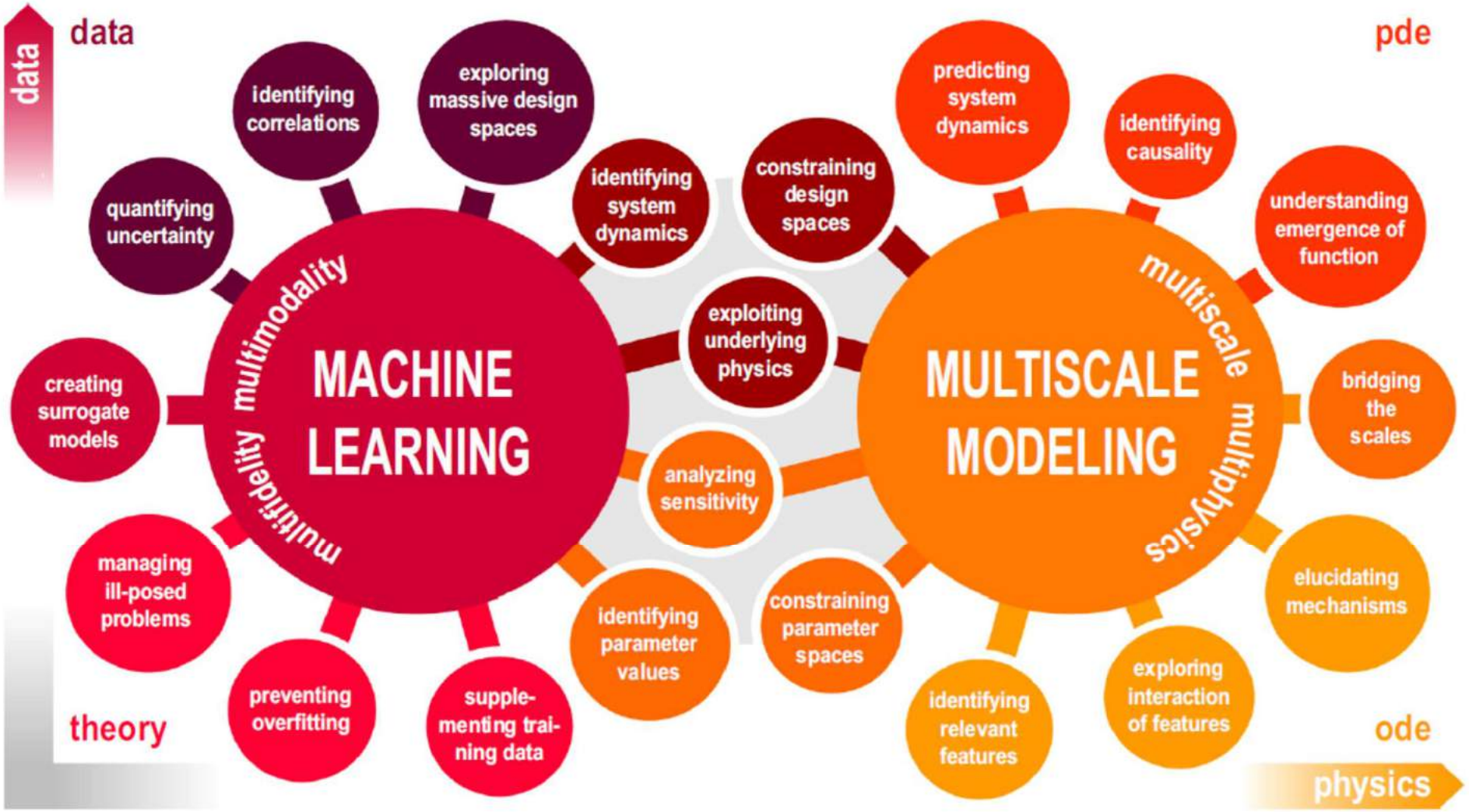

[Alber at al., 2019, Dig Med]

Integration of ML and multiscale modelling: a workflow

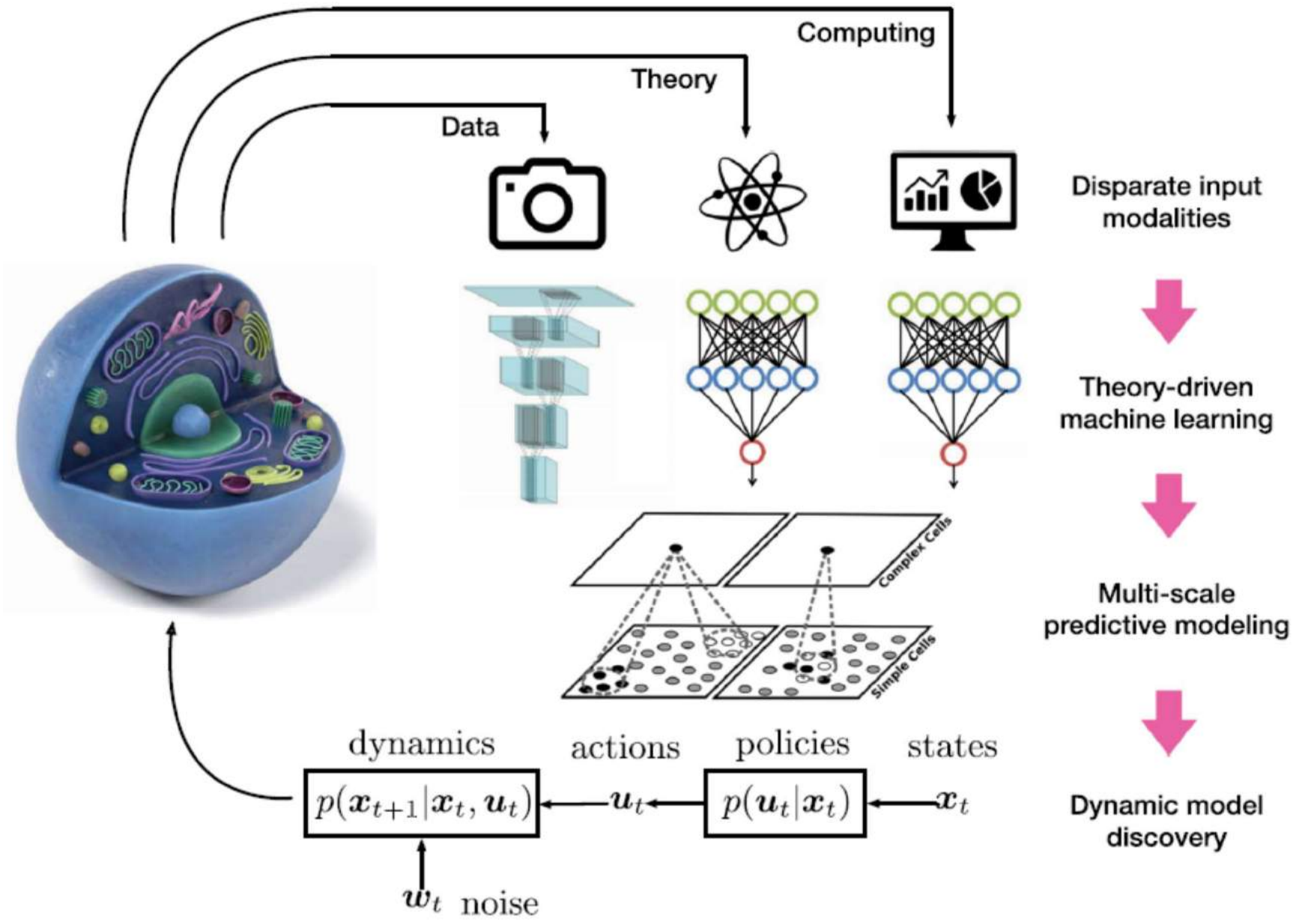

Cells feel their environment through physical forces

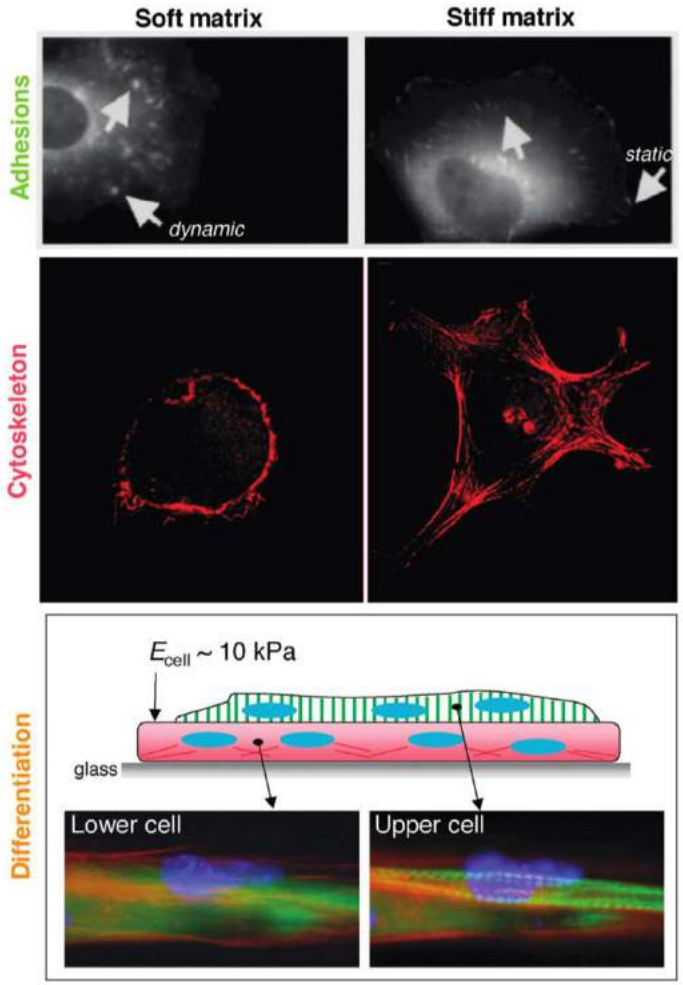

Fig. 2. Substrate stiffness influences adhesion structures and dynamics (*14*), cytoskeleton assembly and cell spreading (*17, 42*), and differentiation processes such as striation of myotubes (*28*). (Top) The arrows point to dynamic adhesions on soft gels and static, focal adhesions on stiff gels. [Adapted from (*14*)] (Middle) The actin cytoskeleton. (Bottom) A cell-on-cell layering in which the lower layer is attached first to glass so that the upper layer, which fuses from myoblasts that are added later, perceives a soft, cellular substrate.

[Discher et al., 2005, Science]

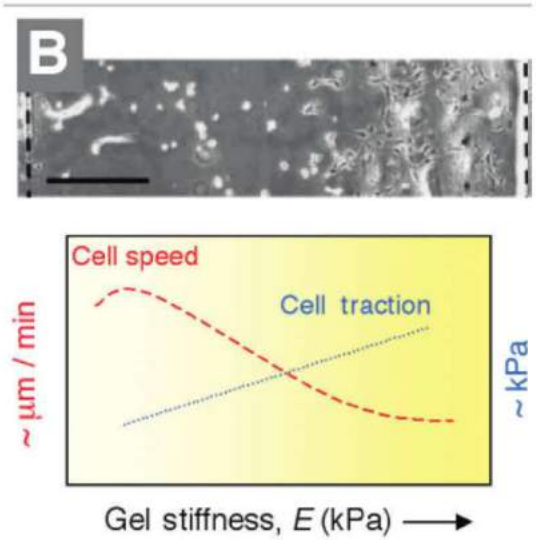

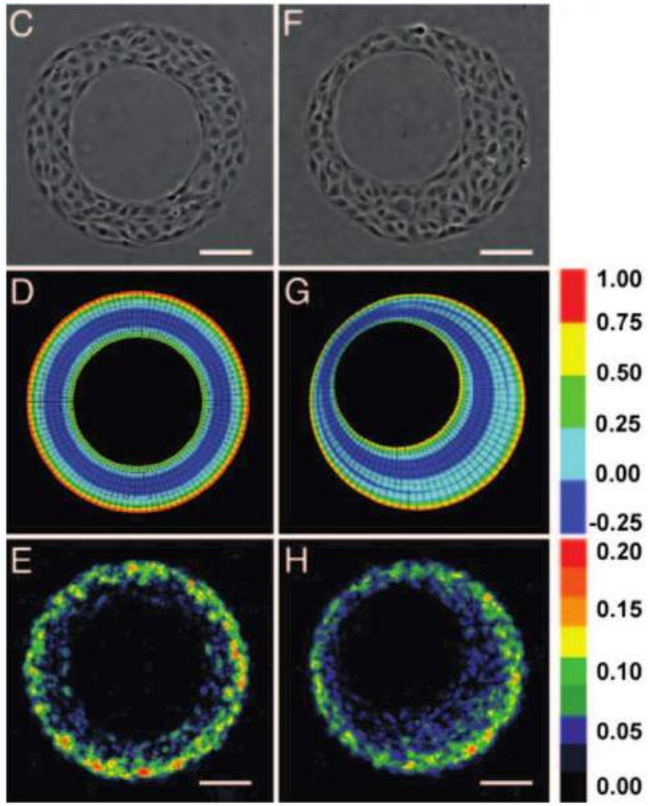

Fig. 2. The pattern of proliferation corresponds to predicted local mechanical stresses. (*A*) FEM mesh of contracting monolayer. (*B*) FEM calculations of relative maximum principal tractional stress exerted by cells in a small square island. (*C–E*) Cells cultured on annulus. Shown are phase contrast (*C*), FEM results (*D*), and colorimetric stacked image of cell proliferation (*E*). (*F–H*) Cells cultured on asymmetric annulus. Shown are phase contrast (*F*), FEM results (*G*), and colorimetric stacked image of cell proliferation (*H*). Outer diameter is 346 µm; inner diameter is 200 µm; center of asymmetric hole is 30 µm from the center of the island. Statistical analysis is presented in Fig. 5. (Scale bars, 100 µm.)

[Nelson et al., 2005, PNAS]

Mechano-biology of tumour cells *in-vitro*

Understanding how mechanical and physical cues influence the invasive strategies of a malignant tissue is crucial for curing many cancers. Numerous in-vitro system models have been proposed to capture the complex features of cancer cells (e.g. migration, proliferation, aggregation and resistance to therapies) , but also the dynamic and evolving feedbacks between cancer and their surroundings, i.e. **mechano-reciprocity** (Friedl)**.**

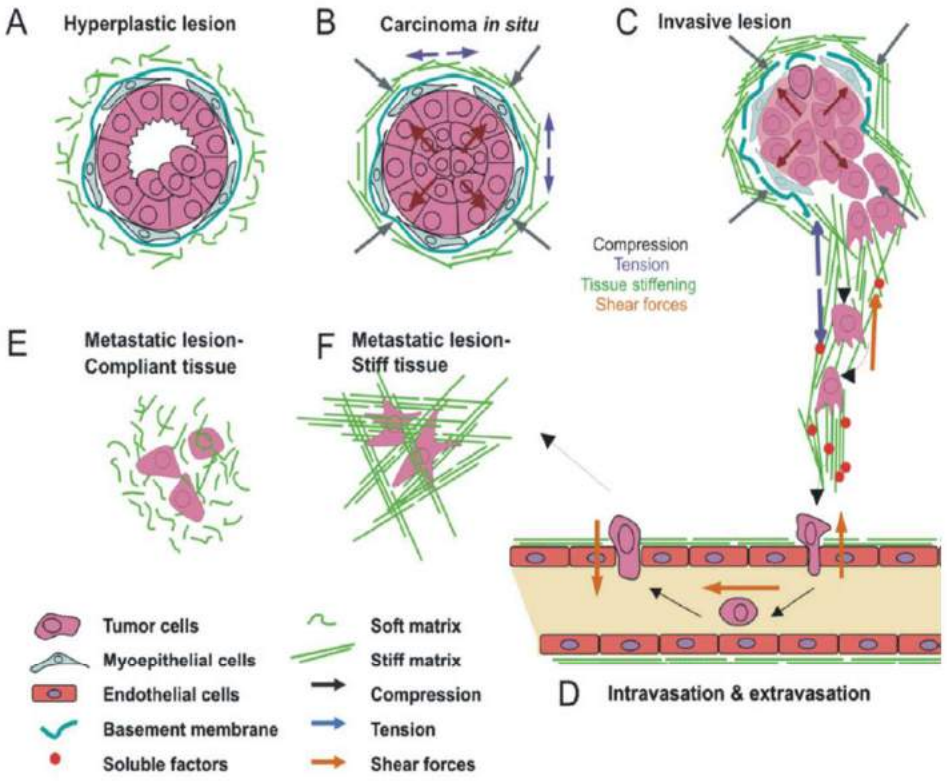

Figure 3. Tumor progression is associated with continuous alterations in tissue and cell mechanics

[Weaver at al 2007, Friedl et al 2009]

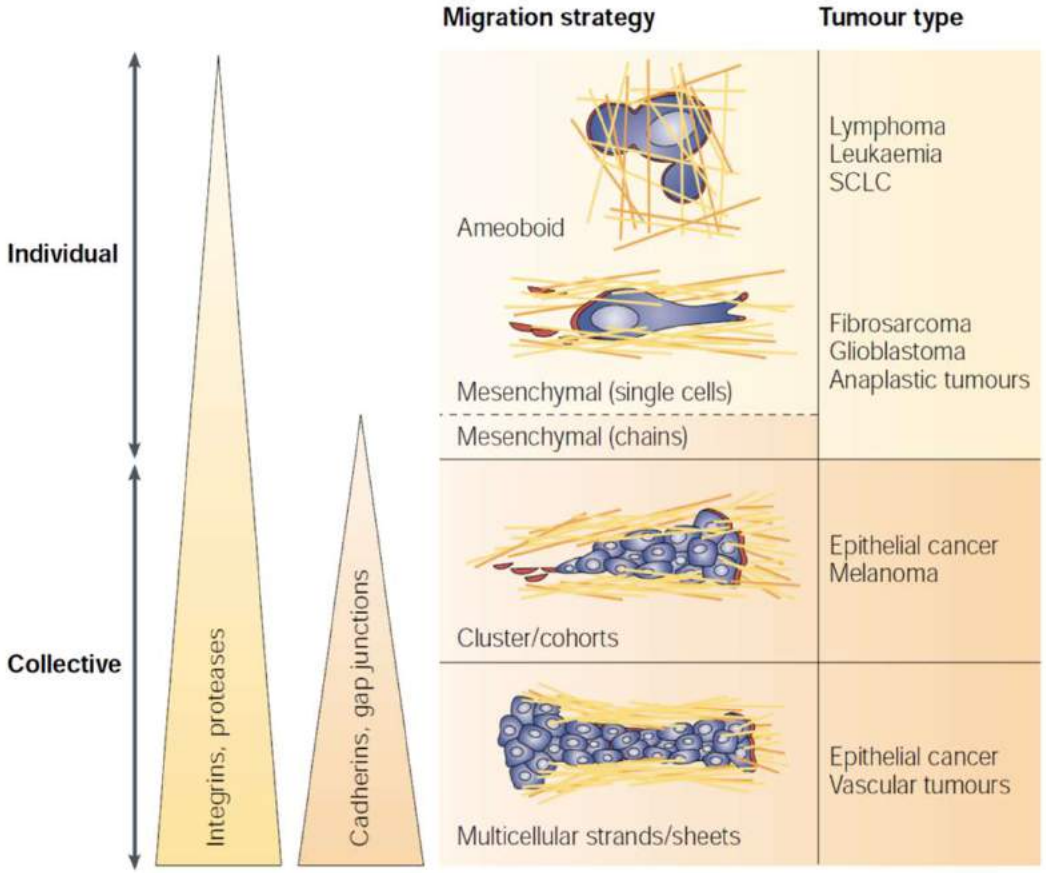

Figure 1 | **Diversity of tumour invasion mechanisms.** Individual or collective tumour-cell migration strategies are determined by different molecular programmes (triangles). From individual (top) to collective (bottom) movements, increased control of cell–ECM interaction is provided by integrins and matrix-degrading proteases. Cell–cell adhesion through cadherins and other adhesion receptors, as well as cell–cell communication, via gap junctions, are specific characteristics of collective cell behaviour. Haematopoietic neoplasia (leukaemia and

OUTLINE

- Model-based versus Data-based learning in biomedicine

- Model and data fusion and physics-driven learning

    - **multi-scale modeling of glioblastoma in precision oncology**

Some clinical facts about Glioblastoma multiforme (GBM)

GBM is a multifactorial disease representing the most common type of primary malignant brain tumors, being charcterized by high invasiveness and complex clinical phenotypes.

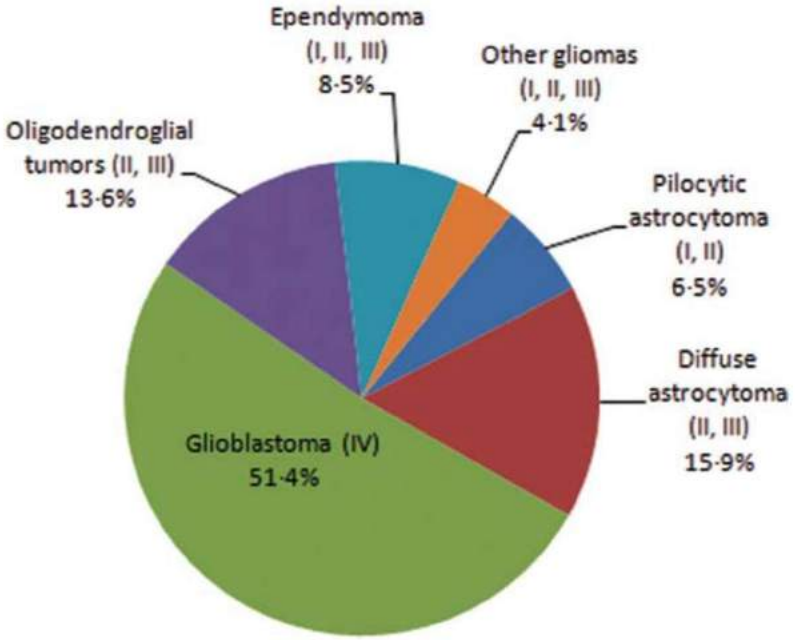

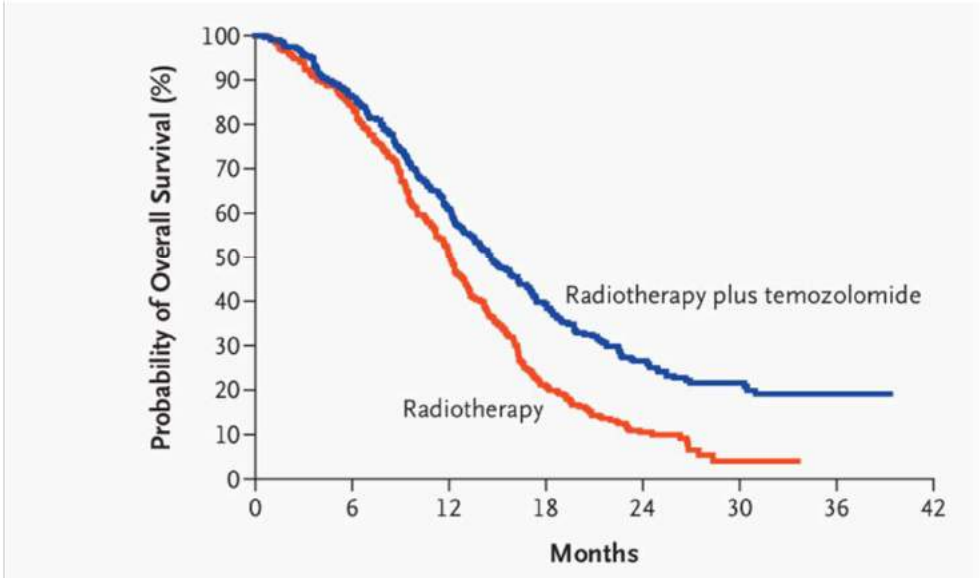

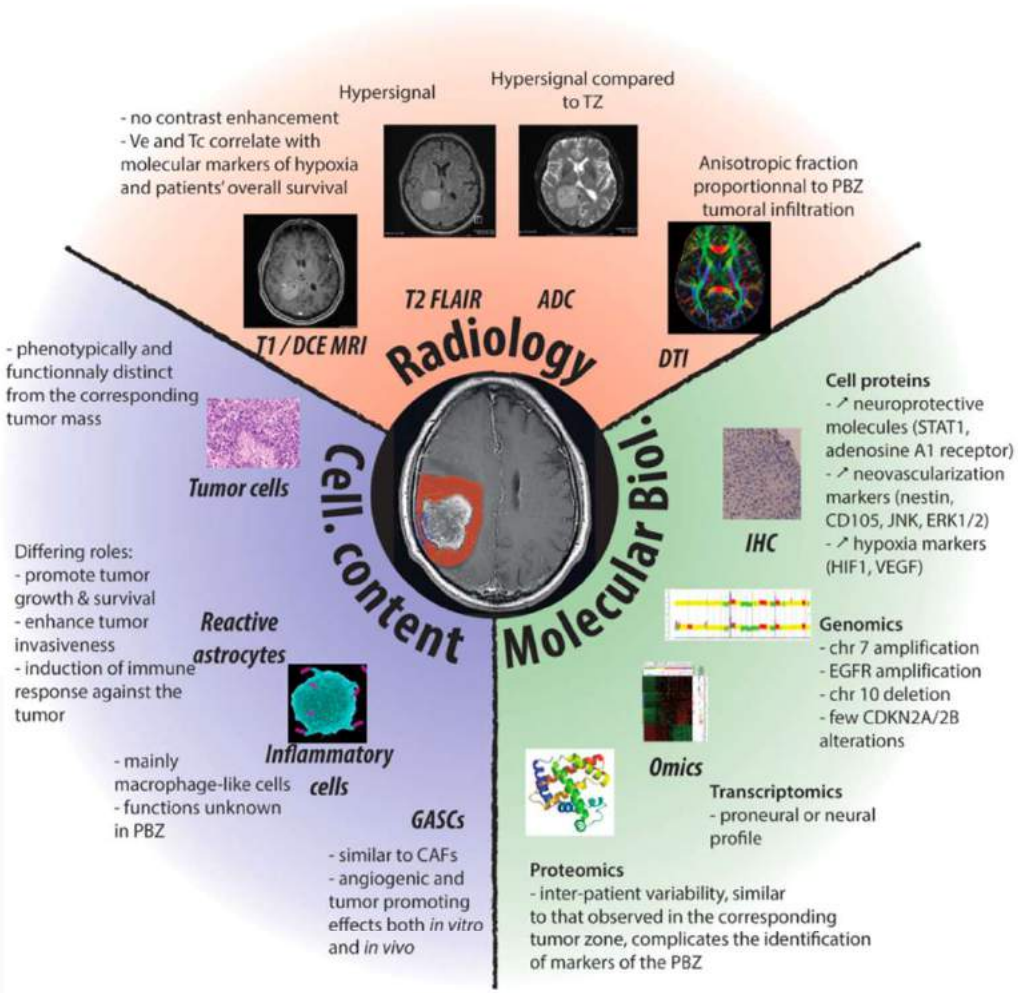

The open problem to identify the resection margin from MRI

The magnetic resonance imaging (MRI) is based on signals from hydrogen ^{1}H nuclei (i.e. protons) under pulsed sequences of a strong magnetic field.

Brain tissues:

- Cerebrospinal Fluid (CSF)
- Grey matter (GM): neuron's soma anc dendrites, blood vessels
- White Matter (WM): neuron's axons

Failure pattern following complete resection plus radiotherapy and temozolomide is at the resection margin in patients with glioblastoma

Kevin Petrecca · Marie-Christine Guiot · Valerie Panet-Raymond · Luis Souhami

Intratumoral heterogeneity in glioblastoma: don't forget the peritumoral brain zone

Jean-Michel Lemée, Anne Clavreul, and Philippe Menei

	1.5 T			3.0 T			
	T_1	T_2	T_2^*	T_1	T_2	T_2^*	PD
White matter	510	67	78	1080	70	50	0.61
Grey matter	760	77	69	1820	100	50	0.69
Arterial blood	1441	290	55	1932	275	46	0.72
CSF	2650	280	/	3817	1442	/	1.0

TABLE 2.1 – Approximate values of T_1, T_2, T_2^* (in ms) and proton density (non-dimensional) for various tissues of the brain and for two different magnetic field strengths (1.5 T and 3.0 T) [34].

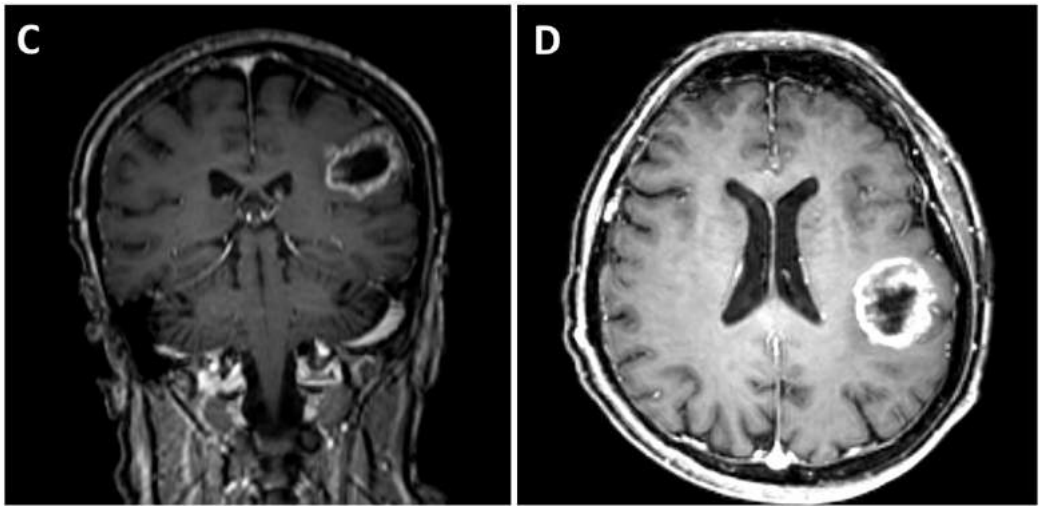

The GLIOMATH project

I will present some research activities funded by the Associazione Italiana per la Ricerca sul Cancro (AIRC) through the grant MFAG 17412.

The GLIOMATH project concerned a multi-disciplinary collaboration between mathematicians, oncological biologists and medical doctors with the aim to translate the patient-specific modeling of glioblastoma into clinics.

F. Acerbi, Prof, MD

A. Bizzi, MD

G. Scita, Prof.

S. Marchesi, PhD

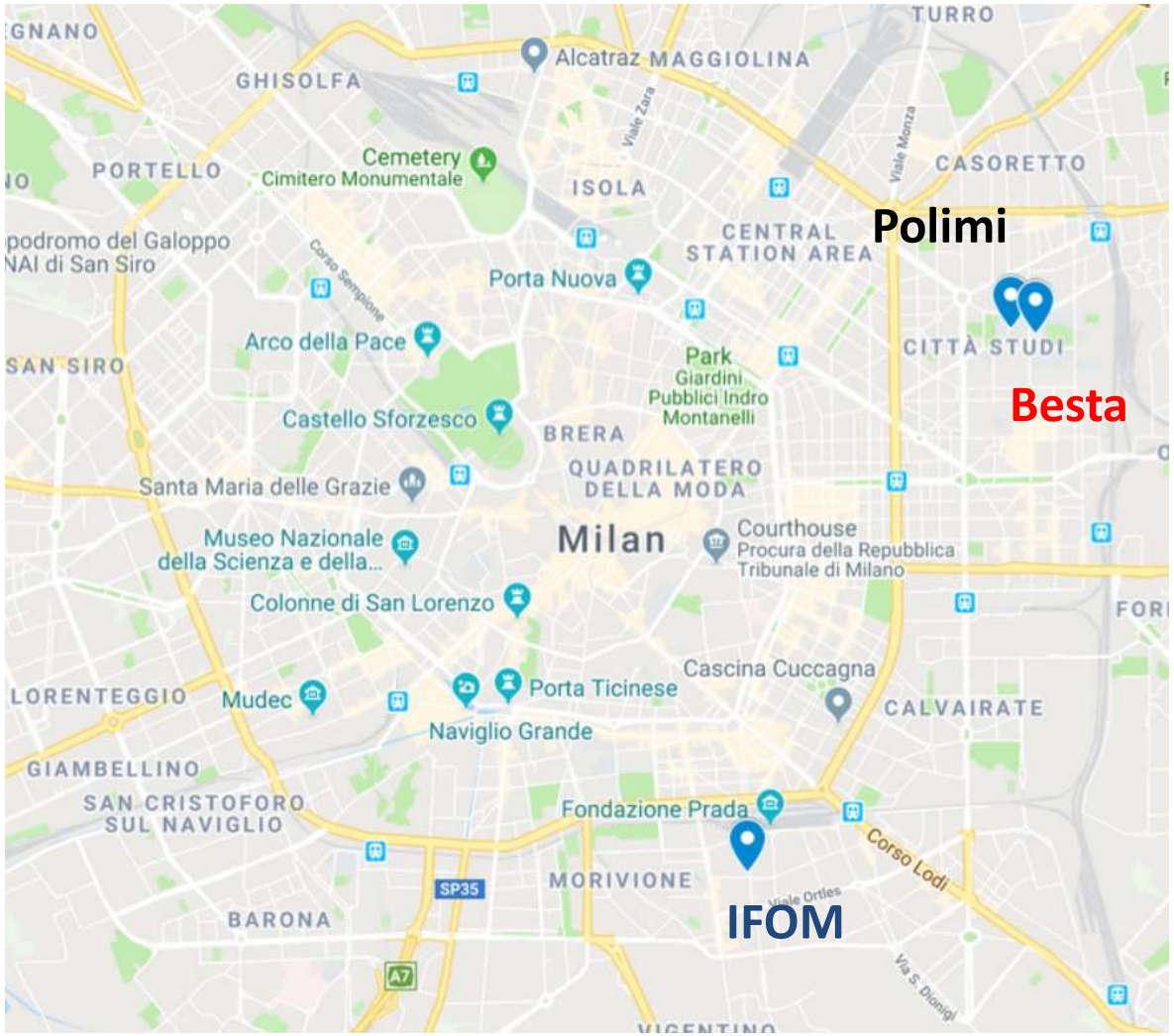

Scientific objectives of the GLIOMATH project

The scientific objectives of the project are:

- to develop a novel mathematical framework for modelling GBM invasion learning its mechano-biological characteristics.;
- to investigate *in-vitro* the impact of chemo-mechanical cues on the growth of glioblastoma (GBM) cell lines (@ IFOM);
- To perform a clinical study, collecting a database of neuroimaging data (e.g. about pre-operative clinical screening, surgical procedures, and post-operative follow-up) on 30 patients with Intracranial GBM (@ Besta);
- To build a computational platform for the patient-specific modeling of GBM growth and recursion, its response to surgery and adjuvant therapies.

AIRC

For this purpose, the mathematical activities involved several **young researchers** with complementary skills ranging from numerical analysis to statistics and image reconstruction.

A. Agosti, PhD
MOX, PoliMi

E. Faggiano, PhD
Univ. Pavia

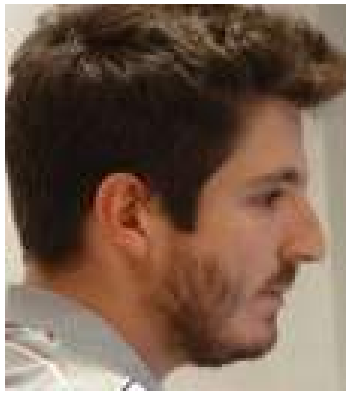

A. Stamm, PhD
Human Technopole

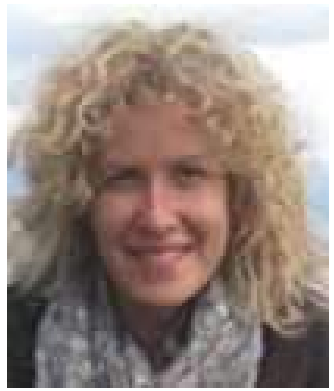

C. Giverso, PhD
Politecnico Torino

Experiments @IFOM

Stress-driven proliferation of GBM cells *in vitro*

To understand the long-term effects of prolonged mechanical stimulation on the morphology and proliferation capacity of glioblastoma cells, we cultured T98G cells with Dextran-containing or hypotonic medium for 6 days..

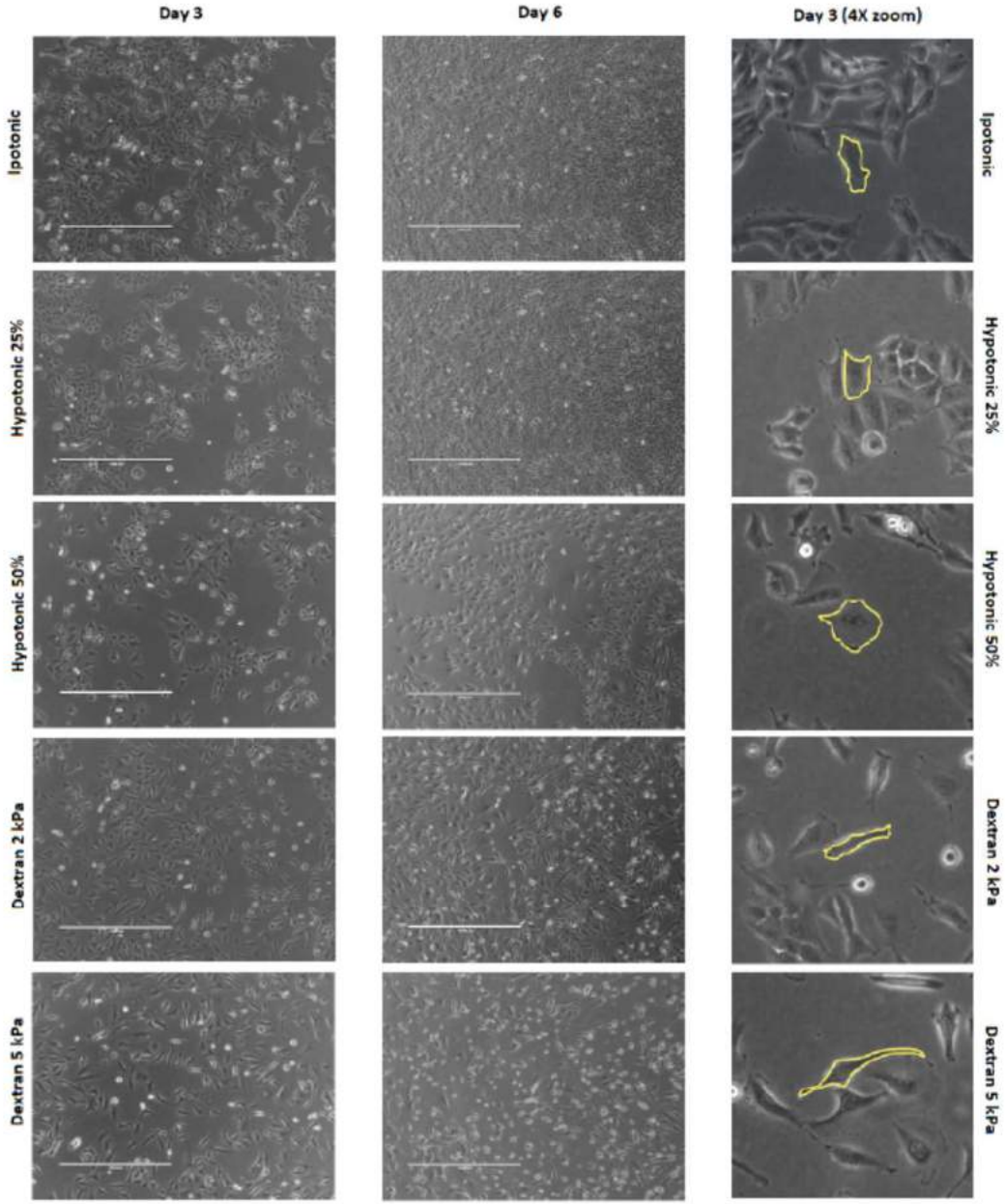

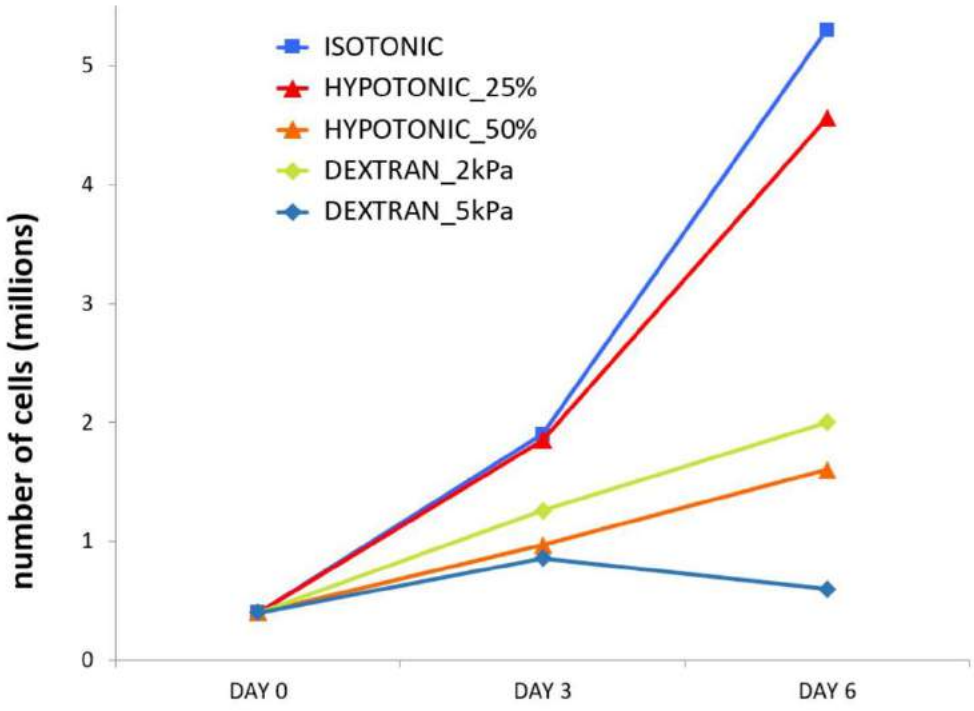

[Pozzi et al 2019, MBE]

Effects of osmotic pressure on cell cycle

We highlight that prolonged mechanical stimuli impinge on the growth properties of glioblastoma cells on specific cell cycle phases, ultimately limiting the proliferative capacity of tumor cells.

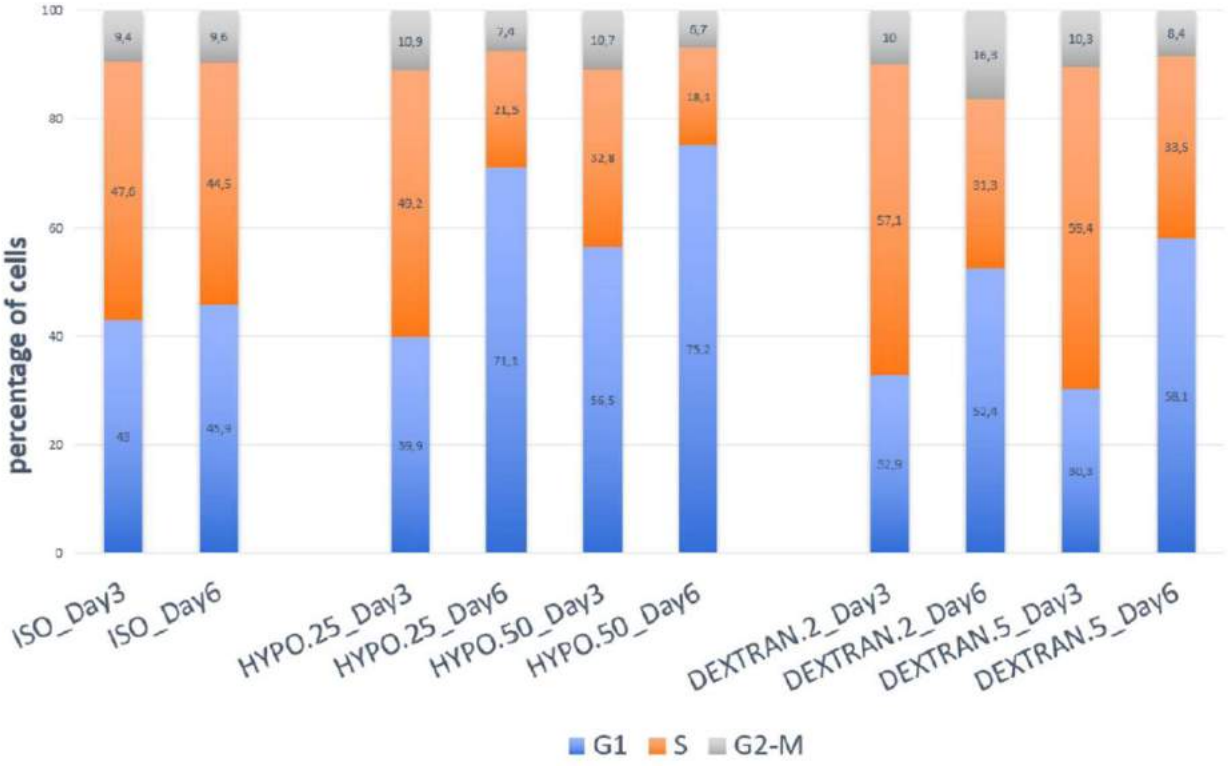

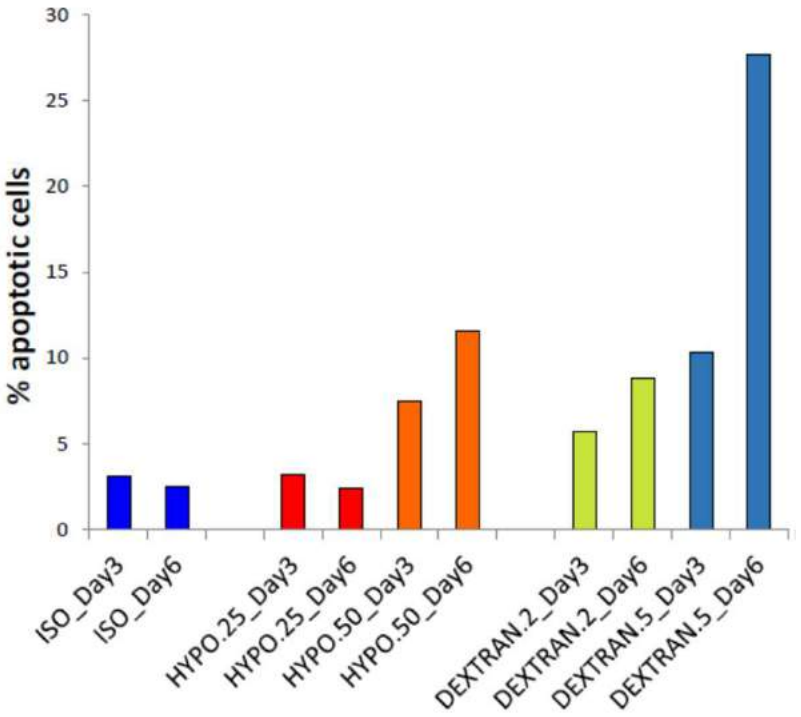

[Pozzi et al 2019, MBE]

Effects of osmotic pressure on cell morphology

Through energetic considerations we suggested a plausible explanation of the morphology crossover between the two solutions, based on a competition between the isotropic response and the splay contribution given by the cytoskeletal fibers.

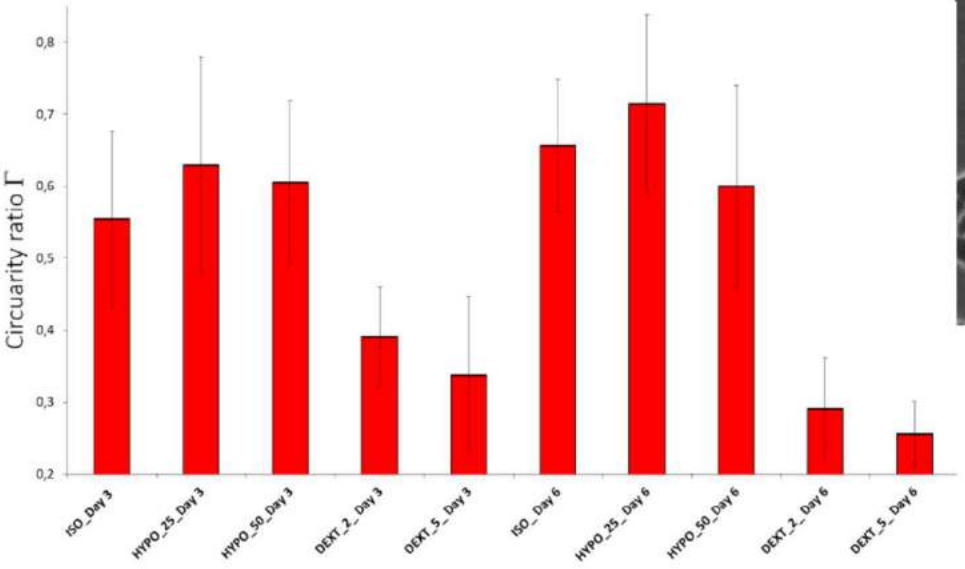

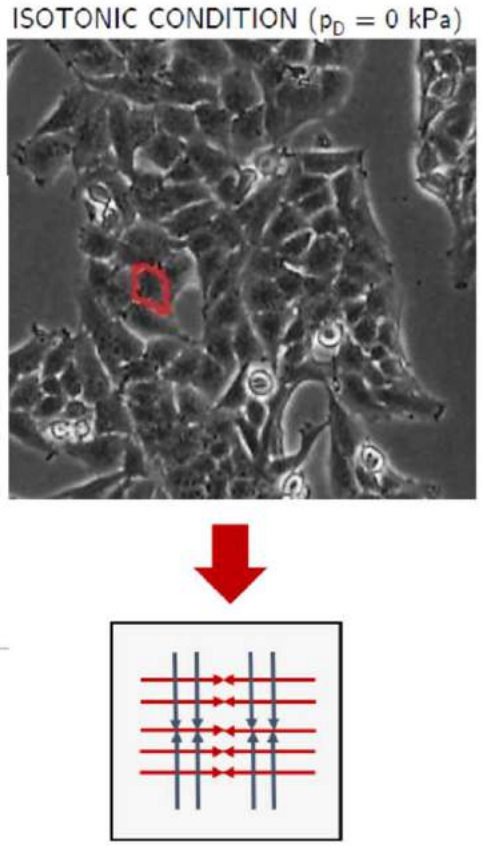

[Pozzi et al 2019, MBE]

3D *in-vitro* systems models: multicellular tumour spheroids

Since the pioneering experiments of Sutherland and co-workers, MCTs have been used as 3D system models to study the resistance to radiation therapies, displaying similar features in term of growth properties and structural heterogeneity as avascular tumoral nodules.

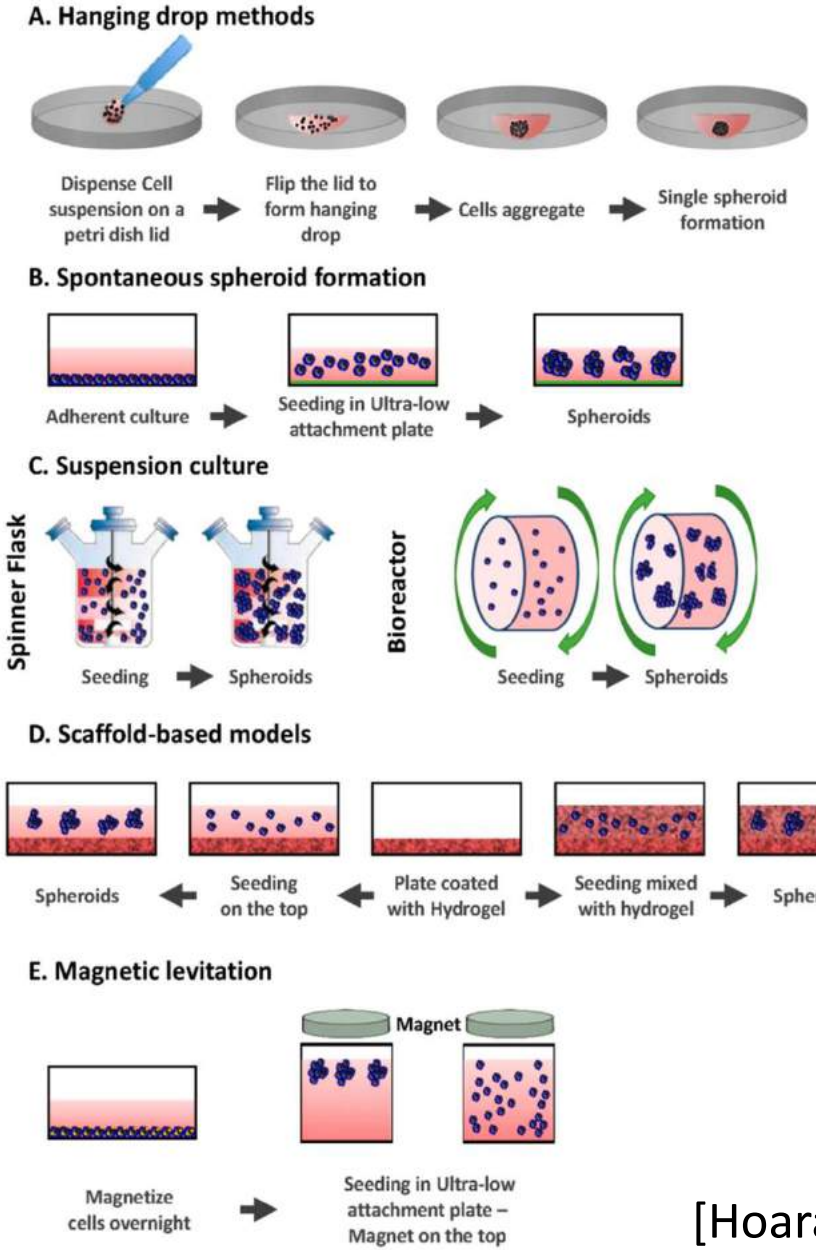

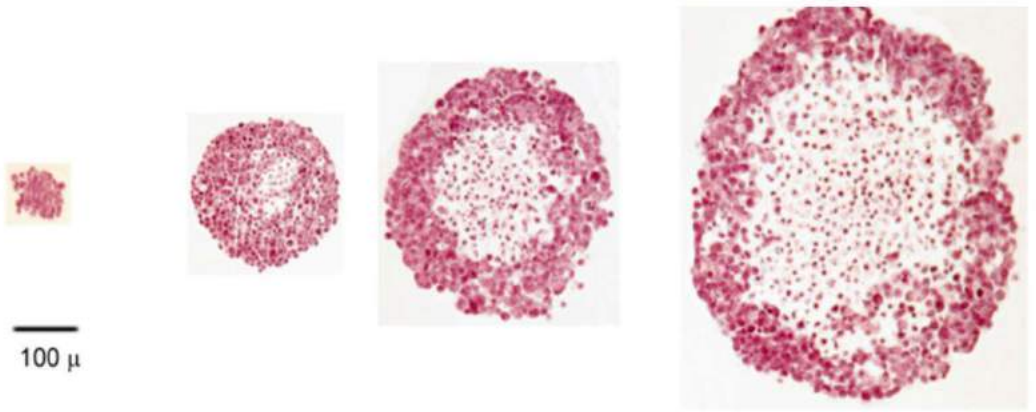

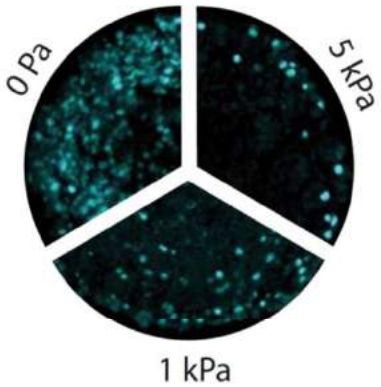

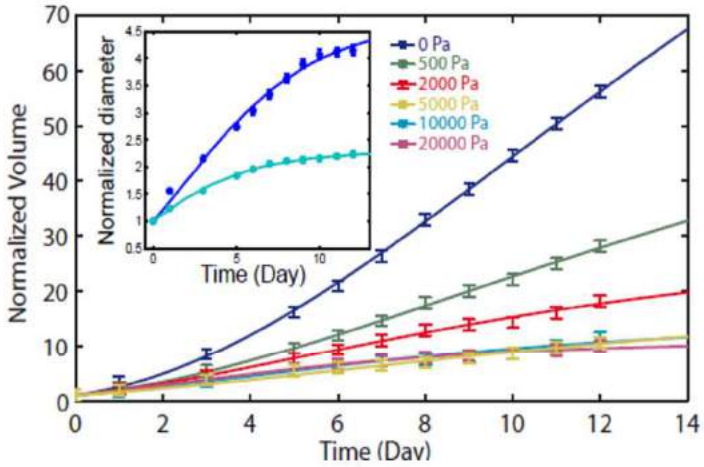

[Hoarau at al 2018, Espinosa et 2012, Montel et al 2009,2011]

From 2D to 3D migration: budding of GBM cells *in-vitro*

We seeded Glioblastoma cells (UG-87) in a Petri dish within a nutrient-rich medium, observing a spontaneous aggregation into clusters.

diameter: 8.6 cm; thickness: 0.17 cm

43.100 cells/cm^2

5% CO_2 modified Dulbecco medium

Which are the mechano-biological cues triggering tumour budding?

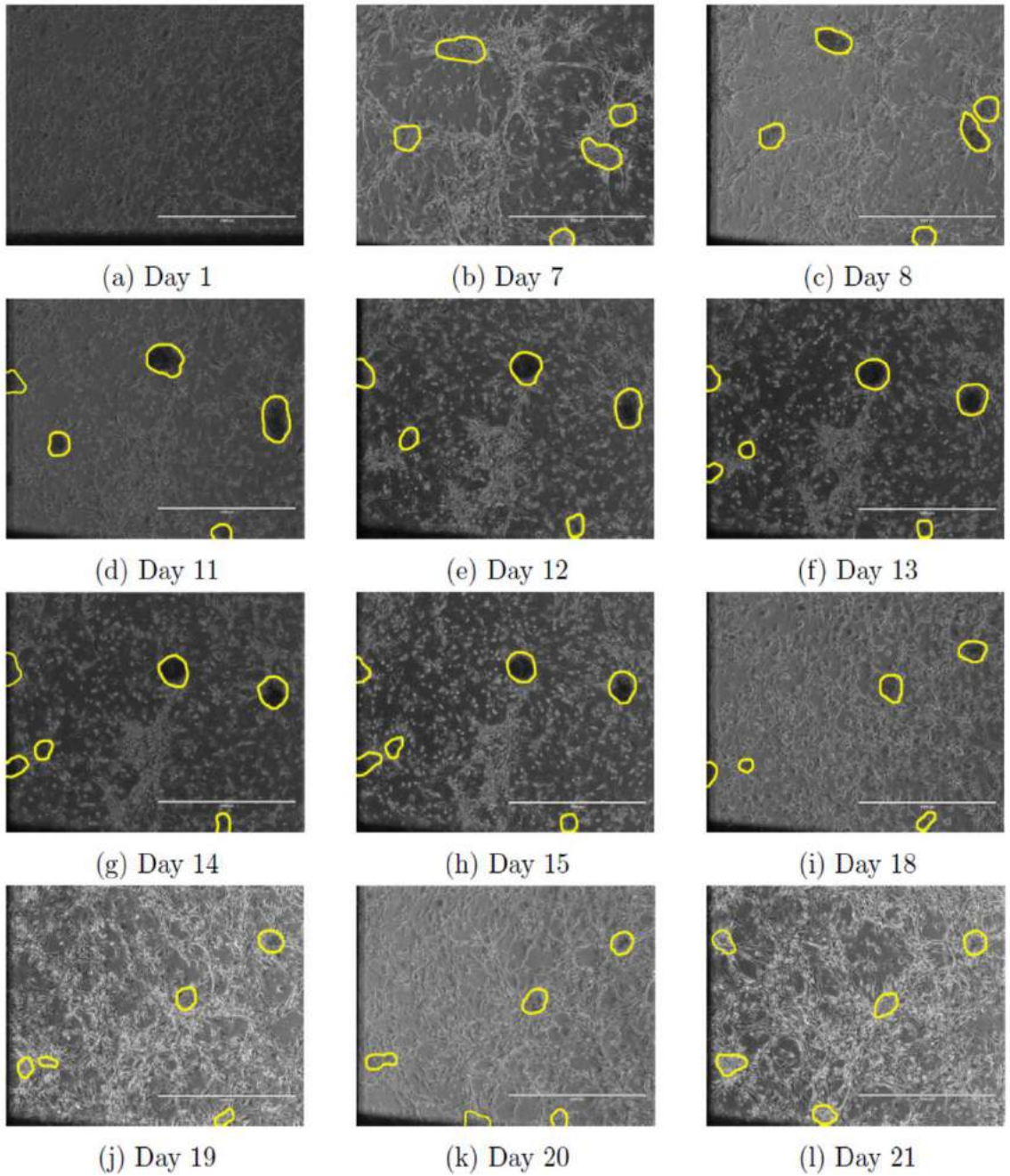

From 2D to 3D migration: budding of tumour cells *in-vitro*

We employ our diffuse interface model with linear growth and reaction terms:

$$\frac{\partial \phi_c}{\partial t} - \mathrm{div}\Big(D(\phi_c)\mathrm{grad}(\mu)\Big) = \Gamma_c = \rho\gamma_c\phi_c\left(\frac{n}{n_s} - \delta_c\right)$$

$$\frac{\partial n}{\partial t} = D_n\nabla^2 n + S_n(n_s - n) - \delta_n\phi_c n$$

with:

$$\begin{aligned} D(\phi_c) &= \phi_c(1-\phi_c)^2/M \\ \mu &= (\chi_c\psi'(\phi_c) - \epsilon^2\nabla^2\phi_c) \end{aligned}$$

The nonequilibrium tumour growth is dominated by the following dimensionless parameters:

$$D = \frac{\chi}{M\gamma_c l_n^2}, \quad \gamma^2 = \frac{\epsilon^2}{\chi l_n^2}, \quad \frac{1}{v} = \frac{\gamma_c}{\delta_n}, \quad \beta = \frac{S_n}{\delta_n}.$$

We expect that budding occurs if **D=O(1)** with a coarsening dynamics influenced by the diffusive nutrient length **ln** and the nutrient growth rate β.

Numerical FE simulations

We perfomed FE simulations using the following ensemble of initial conditions:

C in
s 6
t e
c

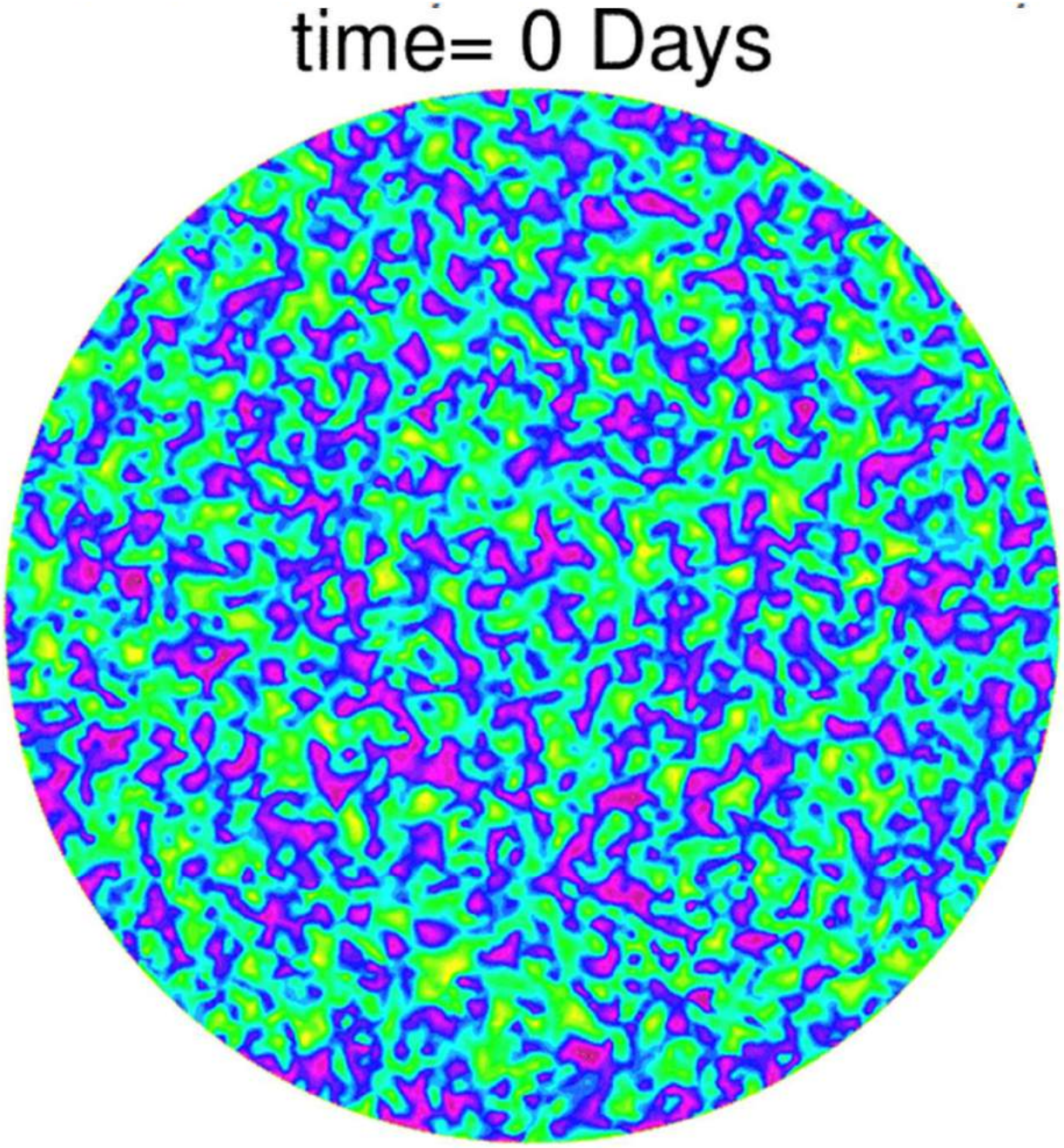

[Agosti Marchesi Scita PC, *under review*]

Numerical simulations versus experiments

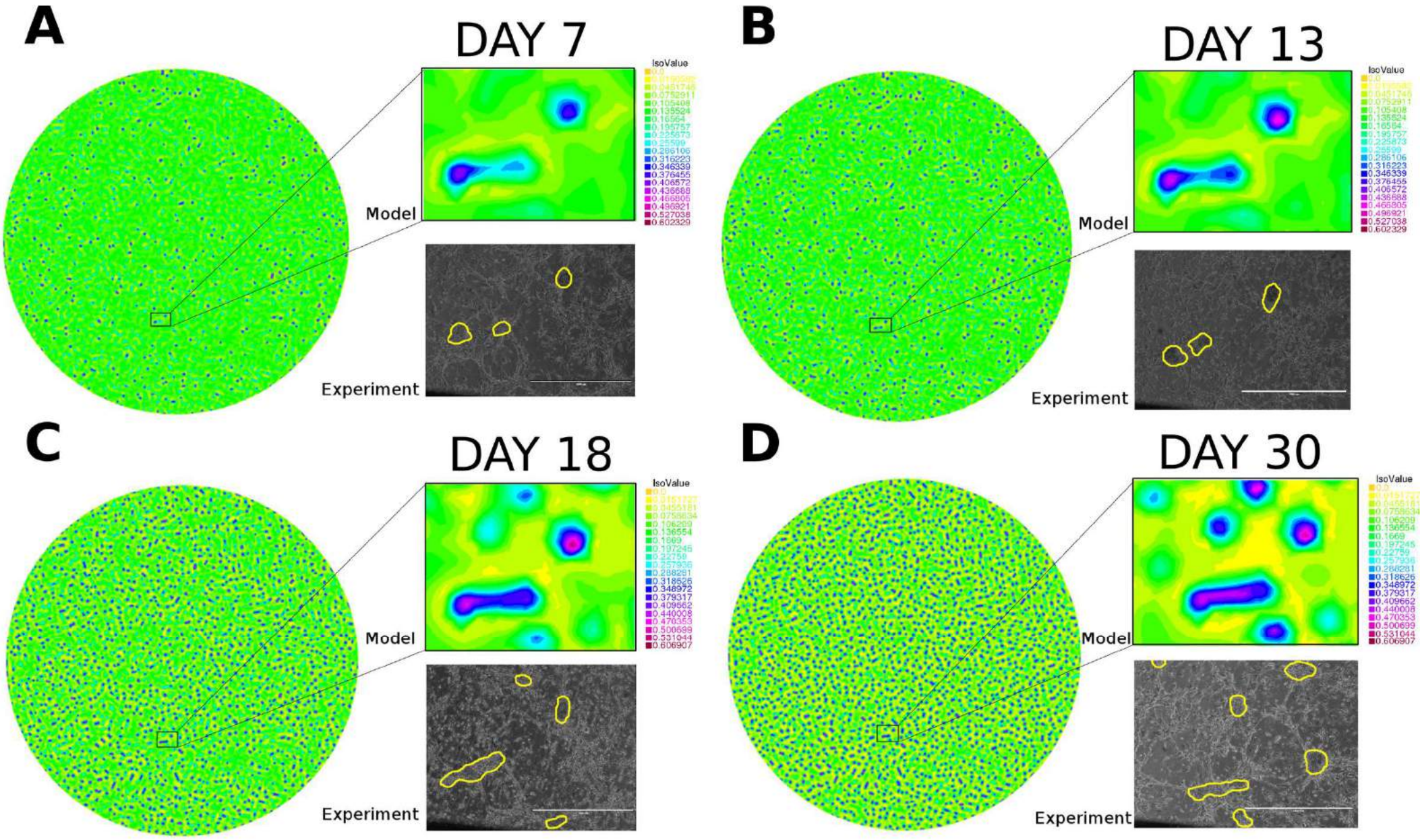

Tumour budding is a self-similar coarsening phenomenon

We study the far-from-equilibrium kinetics of phase ordering of tumour using statistical mechanics tools to highlight its universal features. The tumour clusters become a self-similar ensemble at late times, we assume frame-invariance by a single characteristic length L(t), that grow over time as the different clusters compete to select the equilibrium state.

$$C(\mathbf{h}, \phi_c(\mathbf{x}, t)) = \langle \phi_c(\mathbf{x}+\mathbf{h}, t)\phi_c(\mathbf{x}, t)\rangle = f\left(\frac{|\mathbf{h}|}{L(t)}\right)$$

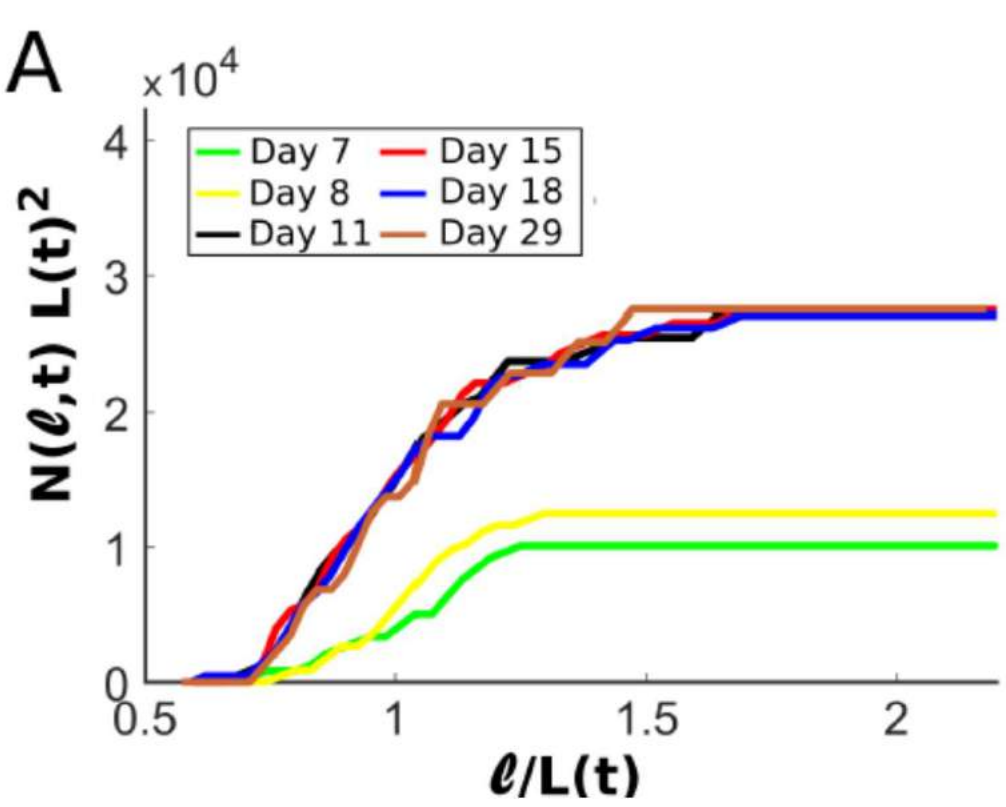

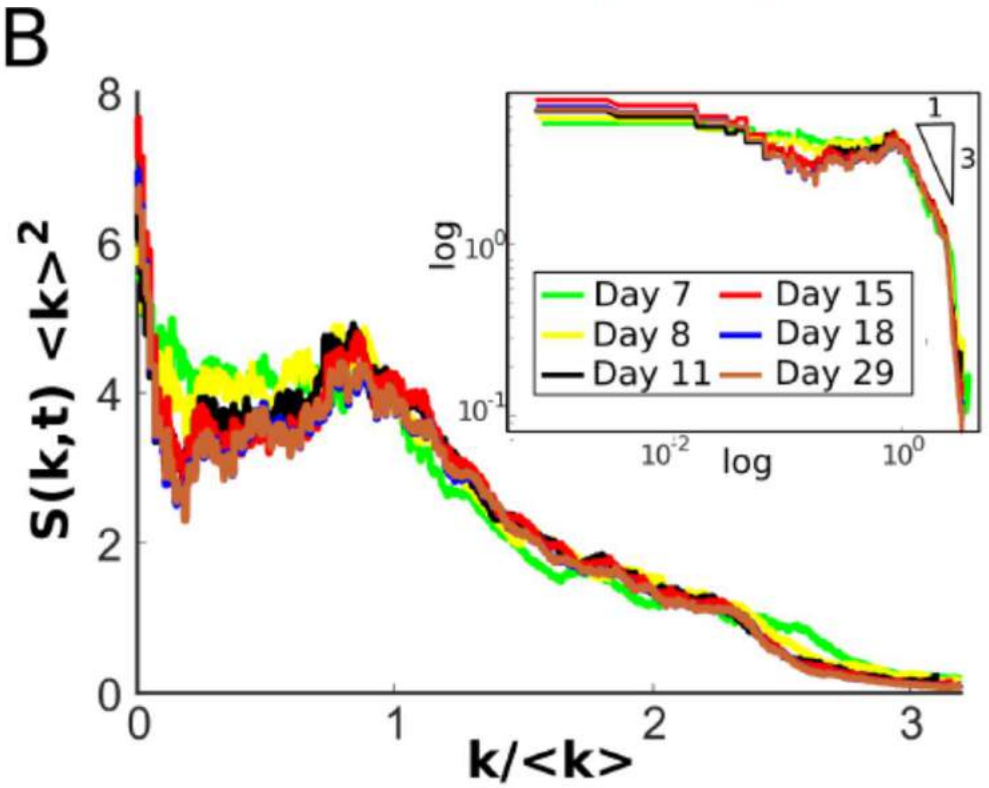

Number of cluster with size smaller or equal to ℓ.

$$L(t) = \langle k \rangle^{-1}$$

$$S(\mathbf{k}, t)\langle k \rangle^2 = g(\langle k \rangle / k)$$

Clinical study @BESTA

The clinical study @Besta

After obtained the approval of the Ethical Committee of IRCCS Besta, we performed a clinical study on a cohort of 30 patients diagnosed with GBM.
The clinical study concerned the following steps:

- **Enrollment:** Signed consensus of patients at first diagnosis, later confirmed from bioptic analysis.
- **Pre Surgery:** Acquisition of MRI and DTI data
- **Surgery:** using either fluorescin or neuro-navigation tools. Bioptic results.
- **Post Surgery** (within 72h) : MRI and, possibly, DTI data depending on the condition of the patient.
- **Therapy:** Radiotherapy (RT) and Chemo-therapy (CT) according to the Stupp protocol
- **Follow-up:** MRI and DRI after 1 month after the end of RT, and every 2 months afterwards.

Centro N.: BESTA

FONDAZIONE I.R.C.C.S. ISTITUTO NEUROLOGICO CARLO BESTA

Titolo dello studio

"Analisi matematica del glioblastoma multiforme: un approccio meccano-biologico per la creazione di strumenti oncologici personalizzati"

Summary of the clinical study

Patient	Age	Tumor localization and characteristics	Surgical resection	Histology	Preop MRI	DOS	Early postop MRI	Late postop MRI
1 – F	60	Corpus callosum	Maximal safe	GBM (WHO IV)	23/05/2017	30/05/2017	31/05/2017	DEAD
2 – F	56	Left frontal	Maximal safe	GBM (WHO IV)	23/05/2017	24/05/2017	31/05/2017	02/10/2017
3 – M	72	Left occipital	Maximal safe	GBM (WHO IV)	07/06/2017	14/06/2017	16/06/2017	DEAD
4 – M	37	Right temporal	Maximal safe	Pleomorphic xanthoastrocytoma (WHO II)	/	/	/	/
5 – M	63	Right temporal (Multifocal)	Partial	GBM (WHO IV)	26/06/2017	03/07/2017	04/07/2017	DEAD
6 – M	54	Right temporal (Multifocal)	Partial	GBM (WHO IV)	05/07/2017	06/07/2017	07/07/2017	DEAD
7 – F	82	Right temporo-occipital	Maximal safe	GBM (WHO IV)	18/07/2017	11/08/2017	16/08/2017	DEAD
8 – F	76	Left parieto-occipital	Maximal safe	GBM (WHO IV)	01/08/2017	07/08/2017	09/08/2017	DEAD
9 – F	47	Corpus callosum	Maximal safe	GBM (WHO IV)	01/08/2017	02/08/2017	04/08/2017	20/10/2017
10 – F	75	Left fronto-parietal	Maximal safe	GBM (WHO IV)	02/08/2017	18/08/2017	21/08/2017	17/11/2017
11 – M	56	Left frontal	Maximal safe	GBM (WHO IV)	05/09/2017	14/09/2017	19/09/2017	09/01/2018
12 – M	55	Left temporo-parietal (2 procedures)	Partial Maximal safe	GBM (WHO IV)	10/10/2017 (06/12/2017)	15/11/2017 15/12/2017	16/11/2017 19/12/2017	17/04/2018
13 – M	55	Right temporal	Maximal safe	GBM (WHO IV)	31/10/2017	02/11/2017	03/11/2017	22/01/2018
14 – F	74	Left fronto-parietal	Maximal safe	GBM (WHO IV)	07/11/2017	24/11/2017	25/11/2017	DEAD
15 – F	73	Right parietal	Maximal safe	GBM (WHO IV)	21/11/2017	22/11/2017	23/11/2017	DEAD
16 – F	35	Right temporal	Maximal safe	GBM (WHO IV)	28/11/2017	30/11/2017	04/12/2017	20/03/2018
17 – M	75	Left temporal (Multifocal)	Partial	GBM (WHO IV)	12/12/2017	21/12/2017	22/12/2017	03/04/2018
18 – M	73	Right fronto-parietal	Maximal safe	GBM (WHO IV)	19/12/2017	21/12/2017	22/12/2017	DEAD
19 – M	62	Left temporal	Maximal safe	AA (WHO III)	/	/	/	/
20 – M	57	Right frontal	Maximal safe	GBM (WHO IV)	06/02/2018	07/02/2018	09/02/2018	08/05/2018
21 – M	54	Left thalamic	Maximal safe	GBM (WHO IV)	07/02/2018	08/02/2018	19/02/2018	DEAD
22 – F	53	Corpus callosum	Biopsy	AA (WHO III)	/	/	/	/
23 – F	60	Right parieto-occipital	Maximal safe	GBM (WHO IV)	26/02/2018	27/02/2018	01/03/2018	
24 – M	55	Right parietal	Maximal safe	GBM (WHO IV)	27/03/2018	29/03/2018	30/03/2018	
25 – M	45	Left frontal	NO SURGERY	/	/	/	/	/
26 – F	70	Right temporal	Maximal safe	GBM (WHO IV)	15/05/2018	15/05/2018	17/05/2018	
27 – M	49	Left frontal	Maximal safe	GBM (WHO IV)	21/05/2018	22/05/2018	23/05/2018	
28 – M	55	Left temporal	Maximal safe	Pleomorphic xanthoastrocytoma (WHO II)	/	/	/	/

Table 2 – Patients included in the GLIO.MATH study up to May 31st, 2018

A patient-specific model integrating DTI data

$$\frac{\partial \phi_c}{\partial t} - \operatorname{div}\left(\frac{\phi_c(1-\phi_c)^2}{M}\mathbf{T}\nabla\Sigma\right) = \underbrace{\nu\phi_c[n-\delta]_+(1-\phi_c) - \nu_d\phi_c[\delta-n]_+}_{\text{proliferation and death}} - \underbrace{k_R(t)\phi_c - k_C(t)\phi_c}_{\text{radioterapy and chemoterapy}},$$

$$\Sigma = -\epsilon^2\Delta\phi_c + \psi'(\phi_c) - \chi_c n, \qquad \text{chemotaxis}$$

$$\frac{\partial n}{\partial t} - \operatorname{div}(\mathbf{D}\nabla n) = \underbrace{S_n(1-n)(1-\phi_c) - \delta_n\phi_c n}_{\text{source and consumption}},$$

$$\nabla\phi_c\cdot\boldsymbol{\nu} = \nabla\mu\cdot\boldsymbol{\nu} = \nabla n\cdot\boldsymbol{\nu} = 0 \quad \text{on } \partial\Omega \quad + \text{ IC.}$$

From DTI we make a patient-specific estimation of the local values of **T** (the tensor of preferential direction) and **D** (the oxygen diffusion tensor)

$$\boldsymbol{T} = \frac{1}{\hat{T}_{av}}\hat{\boldsymbol{T}}, \quad \text{with} \quad \hat{T}_{av} = \frac{1}{3}tr(\hat{\boldsymbol{T}}) \quad \text{and} \quad \hat{\boldsymbol{T}} = a_1(r)\lambda_1\boldsymbol{e}_1\otimes\boldsymbol{e}_1 + a_2(r)\lambda_2\boldsymbol{e}_2\otimes\boldsymbol{e}_2 + a_3(r)\lambda_3\boldsymbol{e}_3\otimes\boldsymbol{e}_3,$$

where $a_i(r)$ are functions of the anisotropy controlling factor r and depend on the linear (c_ℓ), planar (c_p) and spherical anisotropy coefficients (c_s), defined as follows

$$\begin{pmatrix} a_1(r) \\ a_2(r) \\ a_3(r) \end{pmatrix} = \begin{pmatrix} r & r & 1 \\ 1 & r & 1 \\ 1 & 1 & 1 \end{pmatrix} \begin{pmatrix} c_\ell \\ c_p \\ c_s \end{pmatrix}, \qquad c_\ell = \frac{\lambda_1-\lambda_2}{\lambda_1+\lambda_2+\lambda_3}, \qquad c_p = \frac{2(\lambda_2-\lambda_3)}{\lambda_1+\lambda_2+\lambda_3}, \qquad c_s = \frac{3\lambda_3}{\lambda_1+\lambda_2+\lambda_3}.$$

[Agosti et al. IJNLM 2018]

Modelling the effect of therapies

$$- \underbrace{k_R(t)\phi_c - k_C(t)\phi_c}_{\text{radioterapy and chemoterapy}},$$

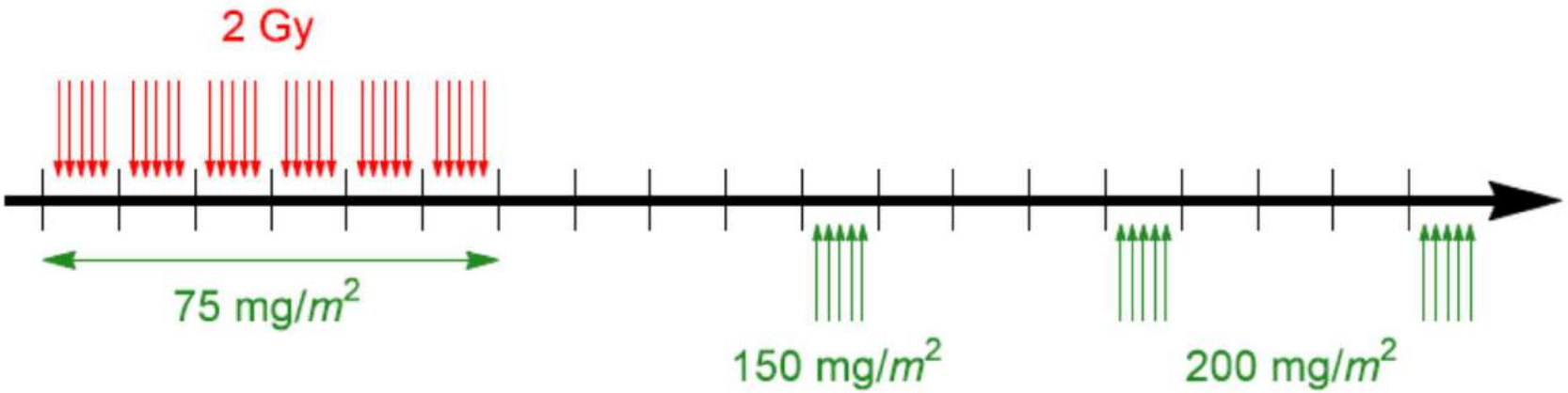

$$R(\phi, t) = k_R(t)\phi, \qquad G(\phi, t) = k_C(t)\phi.$$

$$k_R(t) = \begin{cases} R_{eff} & t_i \le t \le t_{i+1} \\ 0 & \text{otherwise} \end{cases}$$

$$k_C(t) = \begin{cases} k_{C1} & s_0 \le t \le s_1 \\ k_{C2} & s_2 \le t \le s_3 \\ k_{C3} & s_j \le t \le s_{j+1} \\ 0 & \text{otherwise} \end{cases}$$

$$R_{eff} = \alpha md + \beta md^2$$

[Agosti et al. ZAMM 2018]

Further model parameters

E	Brain Young modulus	694 Pa	[18]
ν	Tumour cells proliferation rate	$0.012 - 0.5\ \text{day}^{-1}$	[54,74]
ν_d	Tumour cells death rate	$0.06 - 0.15\ \text{day}^{-1}$	[35]
M_{0h}	Healthy tissue inter-phase friction	$1753.64 - 5032.2\ (\text{Pa day})/\text{mm}^2$	[72]
M_0	Tumour inter-phase friction	$1377.86 - 3991.06\ (\text{Pa day})/\text{mm}^2$	[72]
ϕ_e	Equilibrium cell volume fraction	0.389	[12]
r	Tumour cell radius	0.005 – 0.01 mm	[77,79]
χ_h	Healthy tissue interstitial fluid pressure	106.66 Pa	[10]
χ	Tumour interstitial fluid pressure	866.7 – 1533.3 Pa	[10]
ϵ	Diffuse interface thickness, $2r\sqrt{\chi}$	$0.29 - 0.78\ \text{Pa}^{1/2}\text{mm}$	
k_n	Chemotactic coefficient	$1296\ \text{mm}^2/(\text{mM day})$	[28]
δ	Hypoxia threshold	0.15 – 0.5	[31,35]
n_s	Oxygen concentration in vessels	0.07 mM	[79]
S_n	Oxygen supply rate	$10^4\ \text{day}^{-1}$	[15]
D_n	Oxygen diffusion coefficient	$86.4\ \text{mm}^2/\text{day}$	[54]
l_n	Oxygen penetration distance	0.1 mm	[31]
δ_n	Oxygen consumption rate, D_n/l_n^2	$8640\ \text{day}^{-1}$	
m	Radiation fractions per day	$1\ \text{day}^{-1}$	[70]
N_{days}	Total radiotherapy treatment days	30 day	[70]
N_d	Total radiation doses, nN_{days}	30	
d	Radiation dose	2 Gy	[70]
α	Linear coefficient for RT induced cell kill	$0.027\ \text{Gy}^{-1}$	[59,62]
α/β	Alpha-beta ratio	10 Gy	[29,59,63]
β	Quadratic coefficient for RT induced cell kill, $\alpha(\alpha/\beta)^{-1}$	$0.0027\ \text{Gy}^{-2}$	
R_{eff}	Radiotherapy death rate, $\alpha md + \beta md^2$	$0.0648\ \text{day}^{-1}$	
k_{C1}	Concomitant chemotherapy death rate	$0.00735\ \text{day}^{-1}$	[59]
k_{C2}	First cycle of adjuvant CHT death rate	$0.0147\ \text{day}^{-1}$	[59]
k_{C3}	Remaining cycles of adjuvant CHT death rate	$0.0196\ \text{day}^{-1}$	[59]

[Agosti et al. ZAMM 2018]

Step 1: MRI segmentation

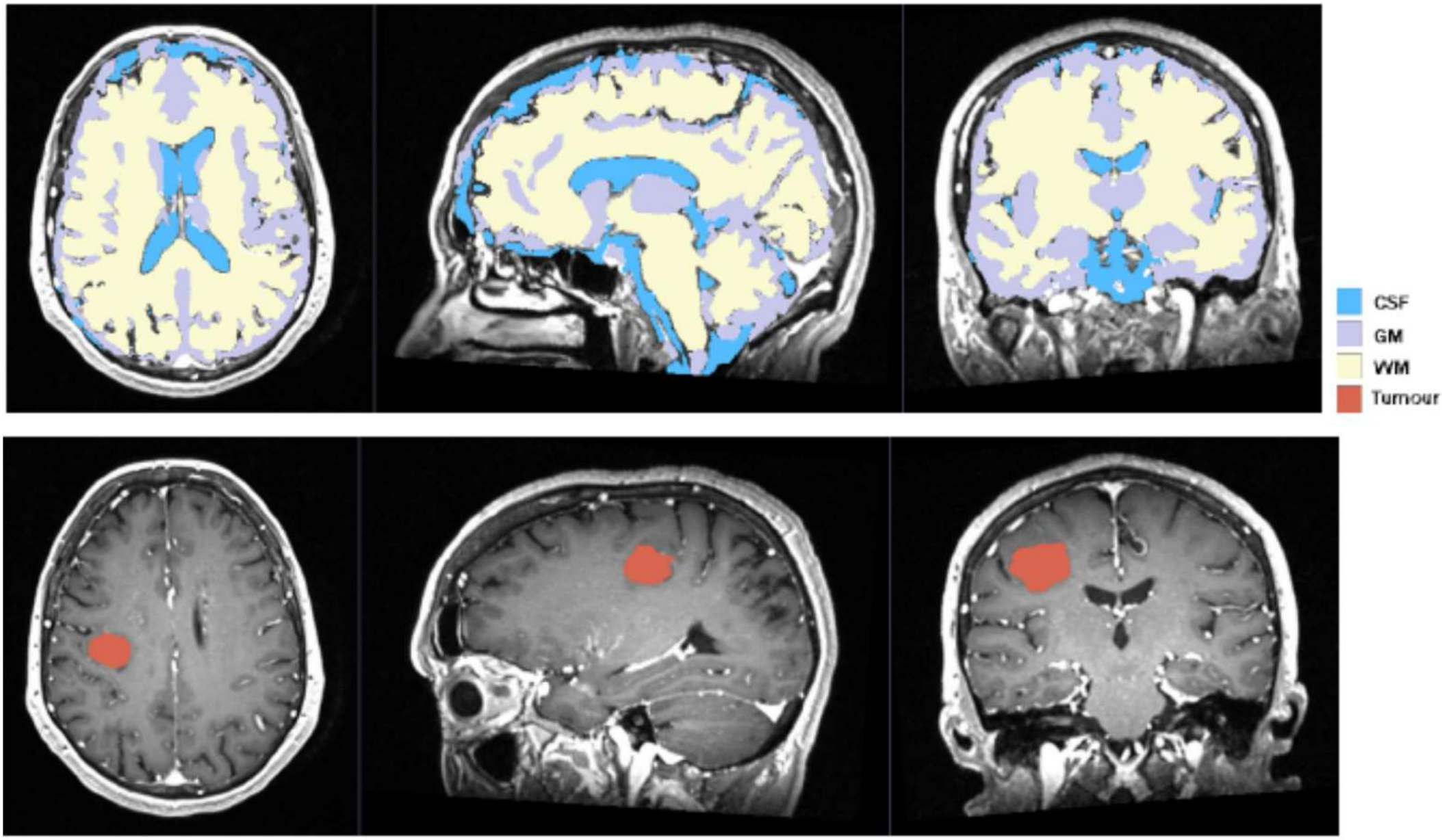

[Colombo PC et al. PloSOne 2016]

Step 2: Mesh refining and labelling

- **extraction** of the external surfaces from the segmented maps
- **smoothing** of the external surfaces
- **generation** of the tetrahedral meshes
- **refinement** of the brain mesh in the area surrounding the tumour
- creation of the labelled brain mesh

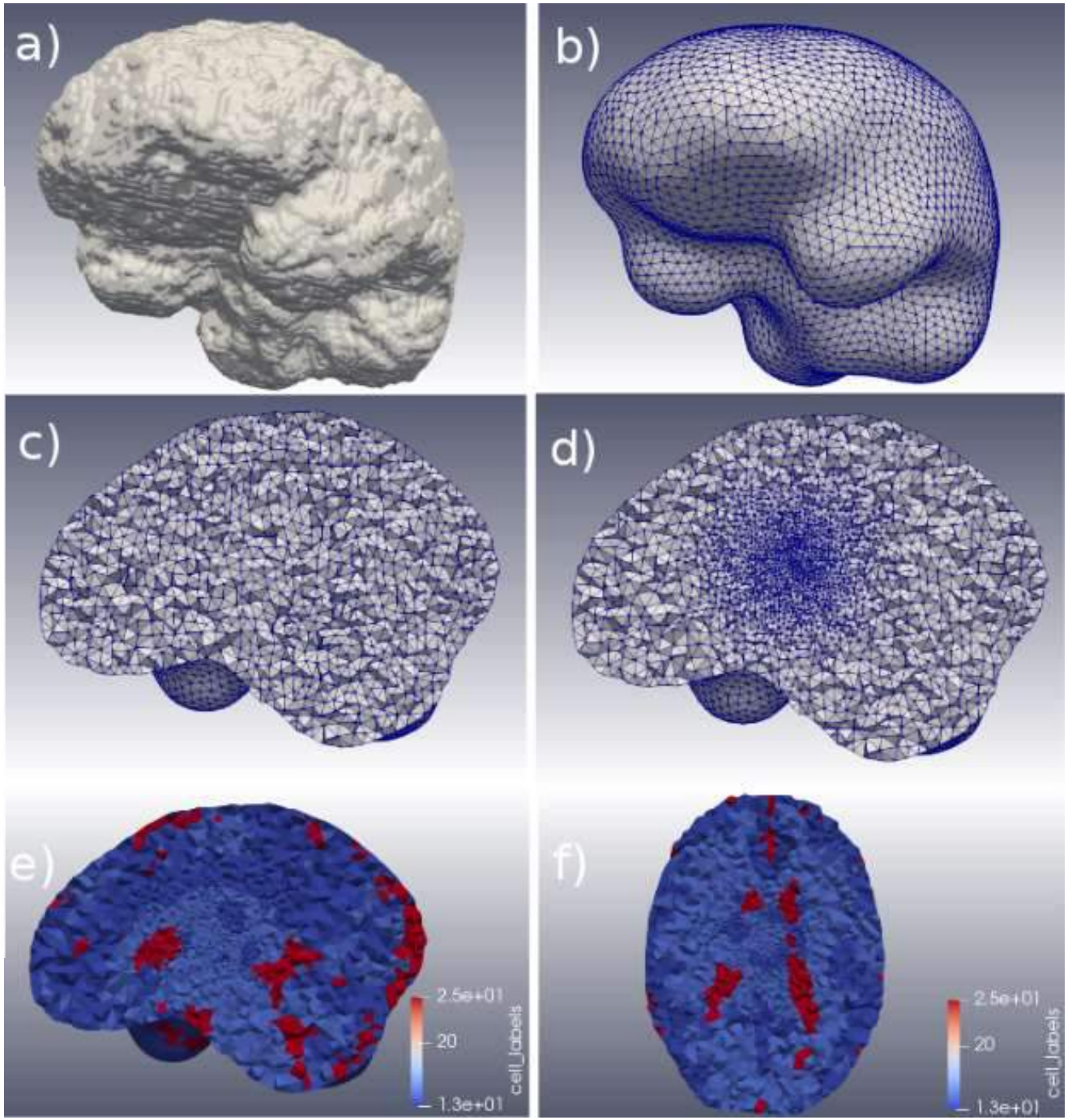

Step 3: DTI registration

- **registration** of the DTI (Diffusion Tensor Imaging) images

$$\boldsymbol{D} = \begin{pmatrix} D_{xx} & D_{xy} & D_{xz} \\ D_{xy} & D_{yy} & D_{yz} \\ D_{xz} & D_{yz} & D_{zz} \end{pmatrix}$$

- creation of six $\boldsymbol{D}$ meshes (nutrient diffusion)
- creation of six $\boldsymbol{T}$ meshes (cells preferential directions of movement)

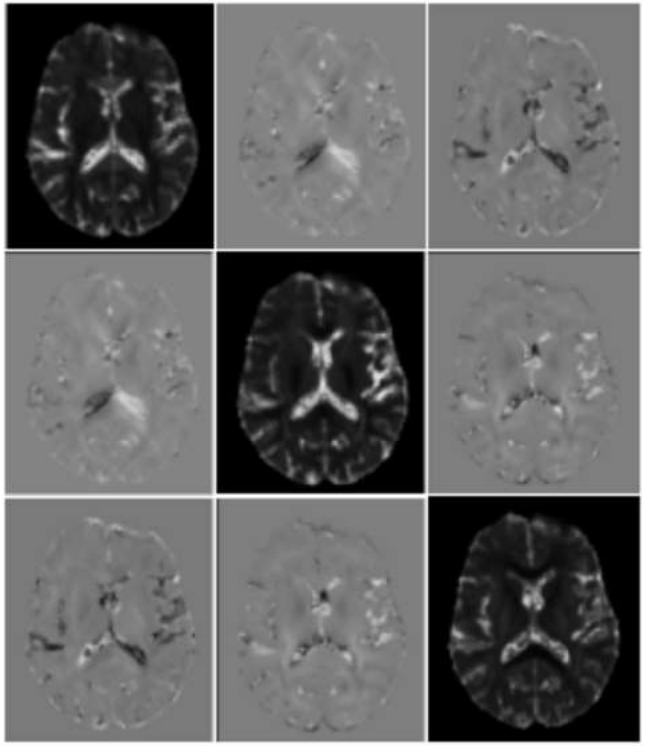

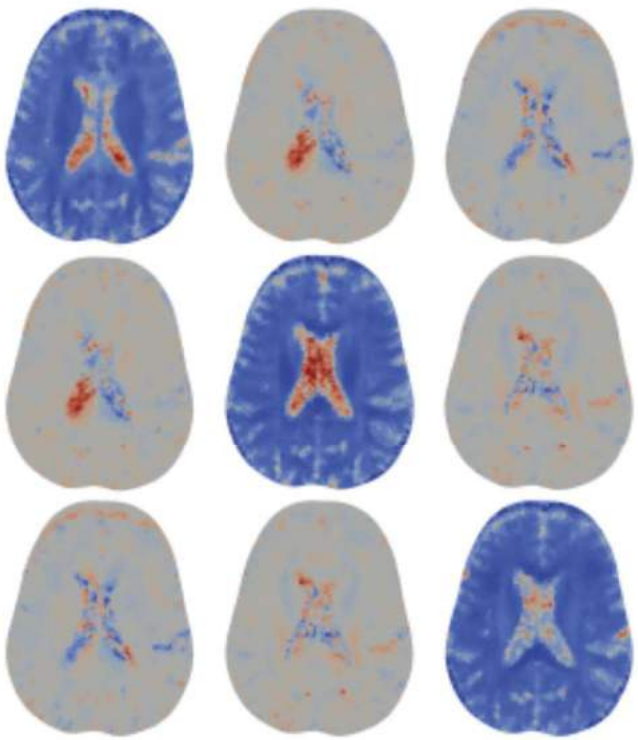

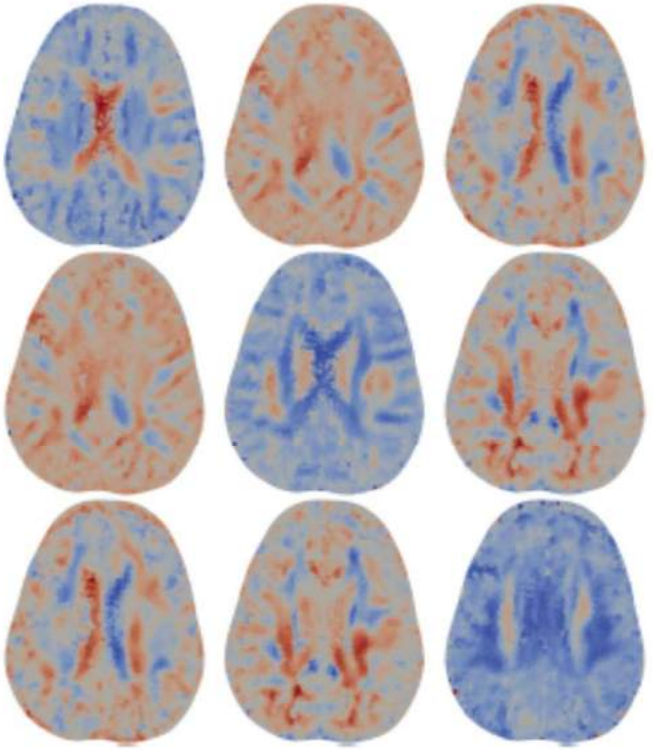

Step 4: Surgical removal and re-meshing

Pre-Surgery

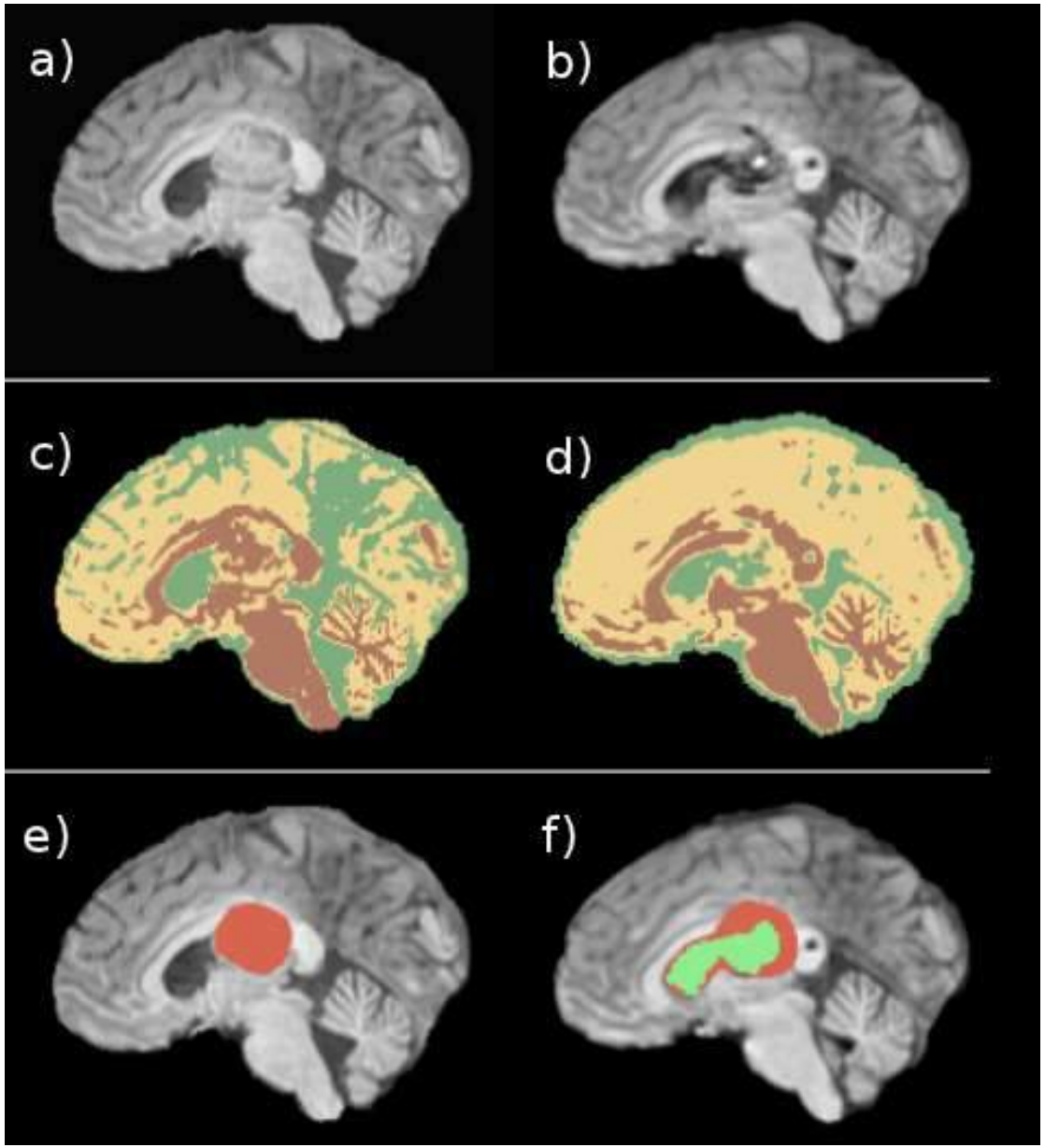

Post-Surgery

a), **b)** x-slice MRI;

c) tissue labels from segmentation;

e), **f)** tumor and deformed ventricle segmentation.

In some cases we need to reconstruct the DTI after surgery considering the deformation of the ventricle

Step 5: Numerical simulations

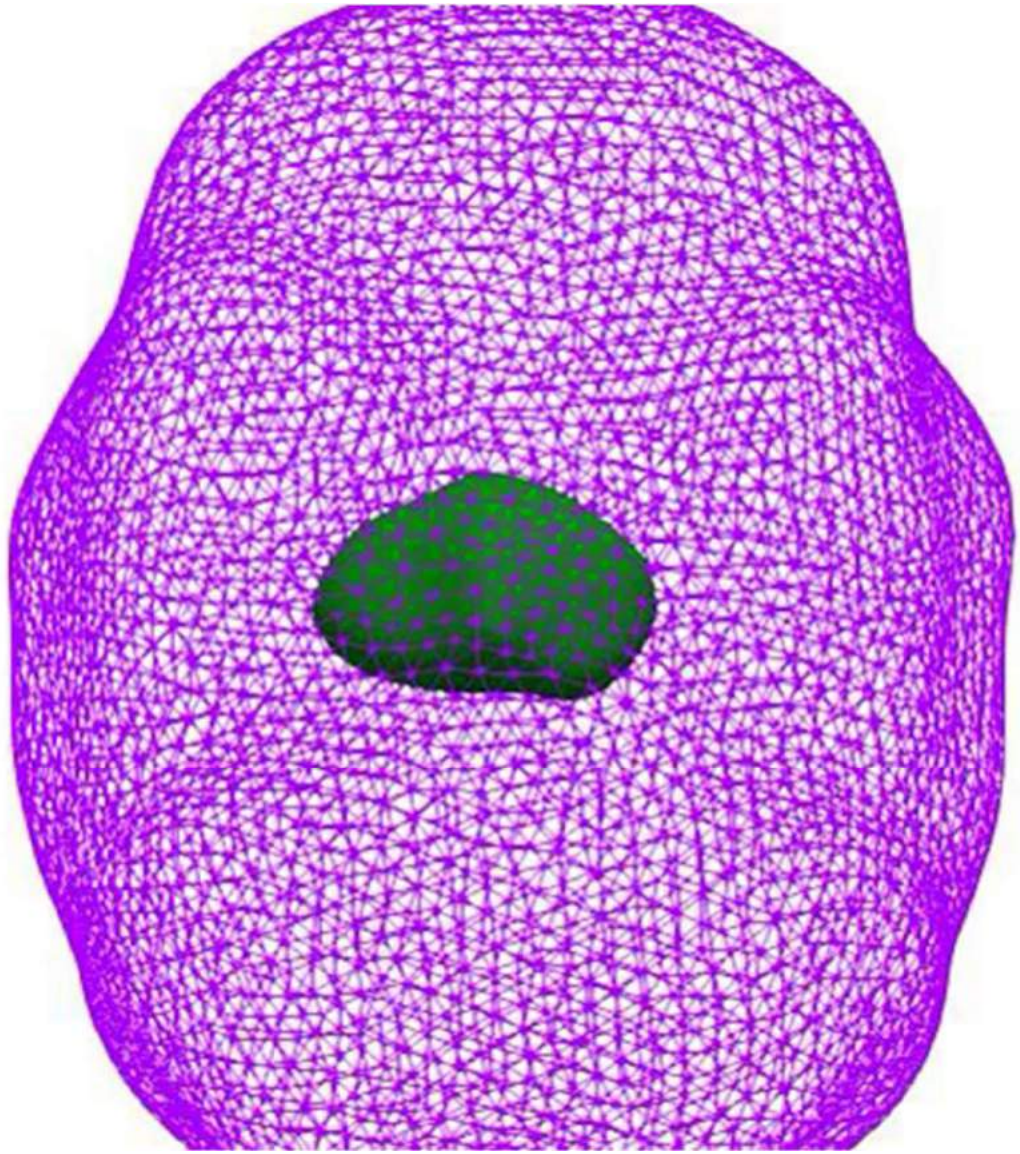

PreSurg

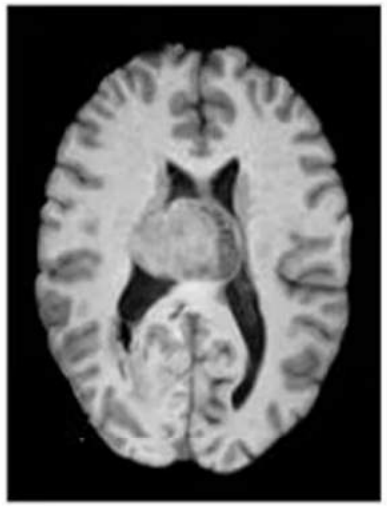

Step 6: Learning from simulations and clinical data

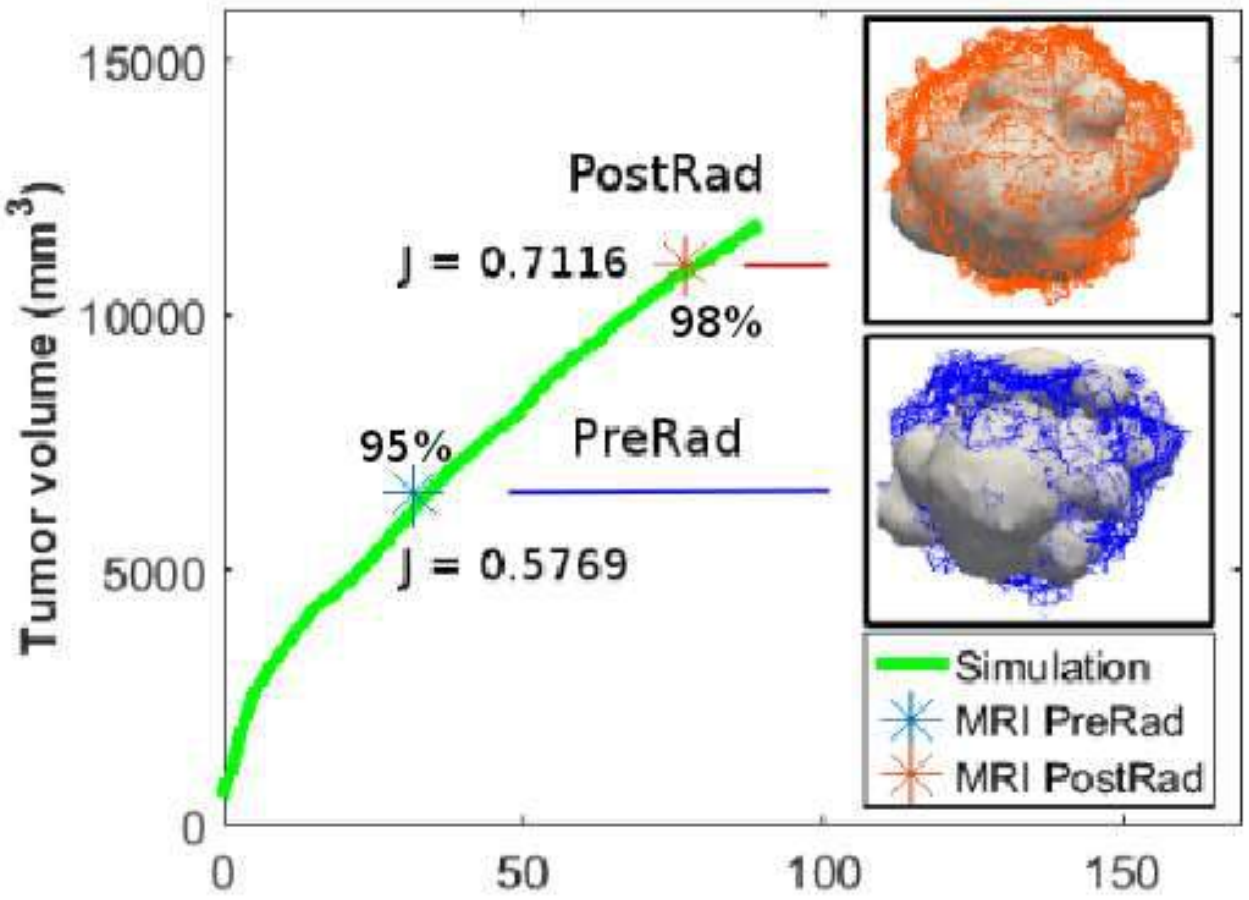

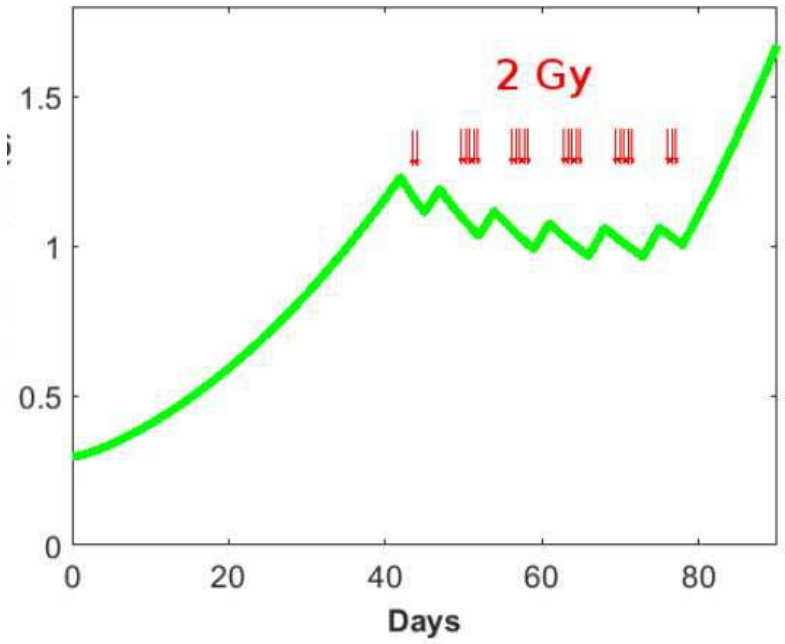

$$J := \frac{\int_\Omega \chi_{A\cap B}}{\int_\Omega \chi_{A\cup B}}$$

Jaccard index J between simulated (A) and experimental (B) tumour mass. It ranges tipically between 0.45 and 0.66 in 3D simulations of parabolic anisotropic model based on DTI (Swanson et al. 2017)

Model-based learning from neuroimaging data

The direct simulation is very expensive from a computational viewpoint, so a trial-and-error approach to calibrate the model results with the neuroimaging data is unfeasible.

To cut the computational cost, we implemented a model order reduction (MOR) based on the proper orthogonal decomposition (POD).

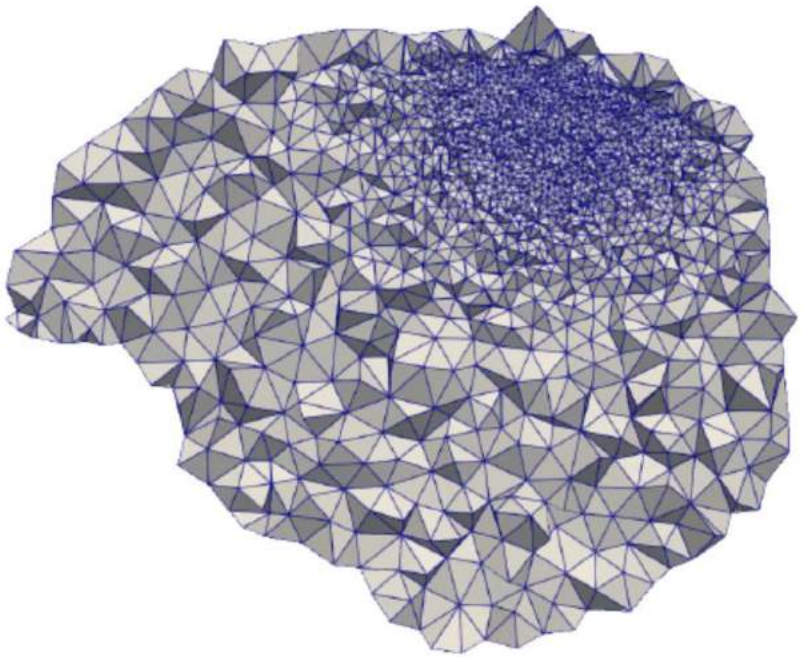

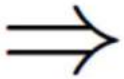

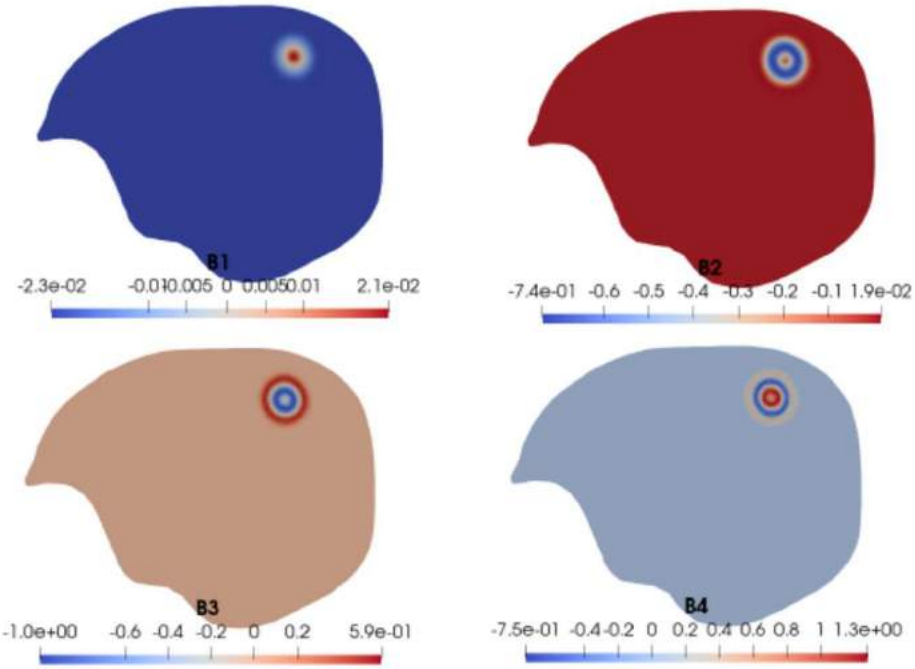

32293 d.o.f.

40 d.o.f.

Basic idea of Model Order Reduction (MOR)

For a given snapshot matrix $F = [f_h^0, \dots, f_h^N]$

- prescribe the required information content to be covered by the POD basis as $ic \in (0, 1]$;
- compute the trace $tr(F^tF)$ of the correlation matrix $F^tF = (f_h^m, f_h^l)_{ml} \in M(N+1, \mathbb{R})$, where $(\cdot, \cdot)$ denotes the chosen inner product;
- set $N_f^{\text{POD}} := \min \left\{ m, \left(\sum_{i \le m} \lambda_i \right) / tr(F^tF) \ge ic \right\}$;
- (successively) compute the eigensystem $\{v^i, \lambda_i\}_{i=1,\dots,N_f^{\text{POD}}}$ of F^tF;
- set $\xi_s^f := \frac{1}{\sqrt{\lambda_s}} \sum_j v_j^s f_h^j \ (1 \le s \le N_f^{\text{POD}})$.

Now we reason similarly as before but this time we let k vary, in the sense that until this point, we only endowed the ROM basis of parameter-specific information of the evolution over time, but we want a basis able to capture the GBM dynamics over the parameters. In order to build up such a basis, we consider the matrices

$$F_\theta = \left[\xi_{11}^\theta, \dots, \xi_{1N_{\text{POD}}^1}^\theta, \dots, \xi_{M1}^\theta, \dots, \xi_{MN_{\text{POD}}^M}^\theta \right]$$

And we repeat the previous algorithm to derive the ROM basis that we use to derive the ROM system that we solve by Newton's method with DEIM interpolation for treating the nonlinearities

[Agosti, PC, Garcke, Hinze, M2AS, 2021

Optimization algorithm

Algorithm 1 Optimization Algorithm

Require: MRI(t=0), DTI(t=0), MRI(t=T), $\mathcal{P}_0, \mathcal{P}_{\text{bio}}, \mathcal{P}_{\text{av}}$;

Initialisation(MRI(t=0), DTI(t=0)) (Problem (7));
Target(MRI(t=T)) (Problem (20));
for $k \geq 0$ **do**
  Step 1–FOM: $\mathbf{F}_k$(**Initialisation**, $\mathcal{P}_k$) (Problem (8));
  Compute $J(\mathbf{F}_{1k}, \mathcal{P}_k)$;
  if $k \geq 1$ **and** $J((\mathbf{F}_{1k}, \mathcal{P}_k) \geq J((\mathbf{F}_{1k-1}, \mathcal{P}_{k-1})$ **then**
    $\mathcal{P}_{\text{opt}} \leftarrow \mathcal{P}_{k-1}$;
    break;
  else if $k \geq 1$ **and** $|J(\mathbf{F}_{1k}, \mathcal{P}_k) - J(\mathbf{F}_{1k-1}, \mathcal{P}_{k-1})| \leq \text{tol}_F |J(\mathbf{F}_{11}, \mathcal{P}_1) - J(\mathbf{F}_{10}, \mathcal{P}_0)|$ **then**
    $\mathcal{P}_{\text{opt}} \leftarrow \mathcal{P}_k$;
    break;
  end if
  Step 2–POD: $\mathbf{P}_k(\mathbf{F}_k)$
  Step 3–Assemble the ROM systems: $\mathbf{A}_k(\mathbf{P}_k)$ (problem (16));
  Step 4–ROM Optimization:
  for $l \geq 0$ **do**
    $\mathcal{P}_l \leftarrow \mathcal{P}_k$,
    Step A: $\mathbf{RN}_l(\mathbf{A}_l, \mathcal{P}_l, \phi_h^0, n_h^0)$; $\mathbf{RL}_l(\mathbf{A}_l, \mathcal{P}_l, \mathbf{RN}_l)$ (problems (17),(18));
    Step B Compute $J(\mathbf{RN}_{1l}, \mathcal{P}_l)$;
    Step C: $\mathcal{P}_{l+1} = \mathbf{PWG}(\mathbf{RN}_l, \mathbf{RL}_l, \mathcal{P}_l)$ (problem (25));
    if $\max_{i=1,\ldots,|\mathcal{P}|} \left((\mathcal{P}_{i,l+1} - \mathcal{P}_{i,l})/\mathcal{P}_{i,l}\right) \leq \text{tol}_{Ra}$ **and**
$|J(\mathbf{RN}_{1l+1}, \mathcal{P}_{l+1}) - J(\mathbf{RN}_{1l}, \mathcal{P}_l)| \leq \text{tol}_{Rb} |J(\mathbf{RN}_{11}, \mathcal{P}_1) - J(\mathbf{RN}_{10}, \mathcal{P}_0)|$**and**
$|\mathcal{P}_{l+1}(1) - \mathcal{P}_{l+1}| \leq \text{tol}_{Pa} |\mathcal{P}_0| + \text{tol}_{Pr} |\mathcal{P}_0(1) - \mathcal{P}_0|$ **then**
      $\mathcal{P}_{k+1} \leftarrow \mathcal{P}_{l+1}$;
      break.
    end if
  end for
end for

Application 1: growth prediction of a primary GBM

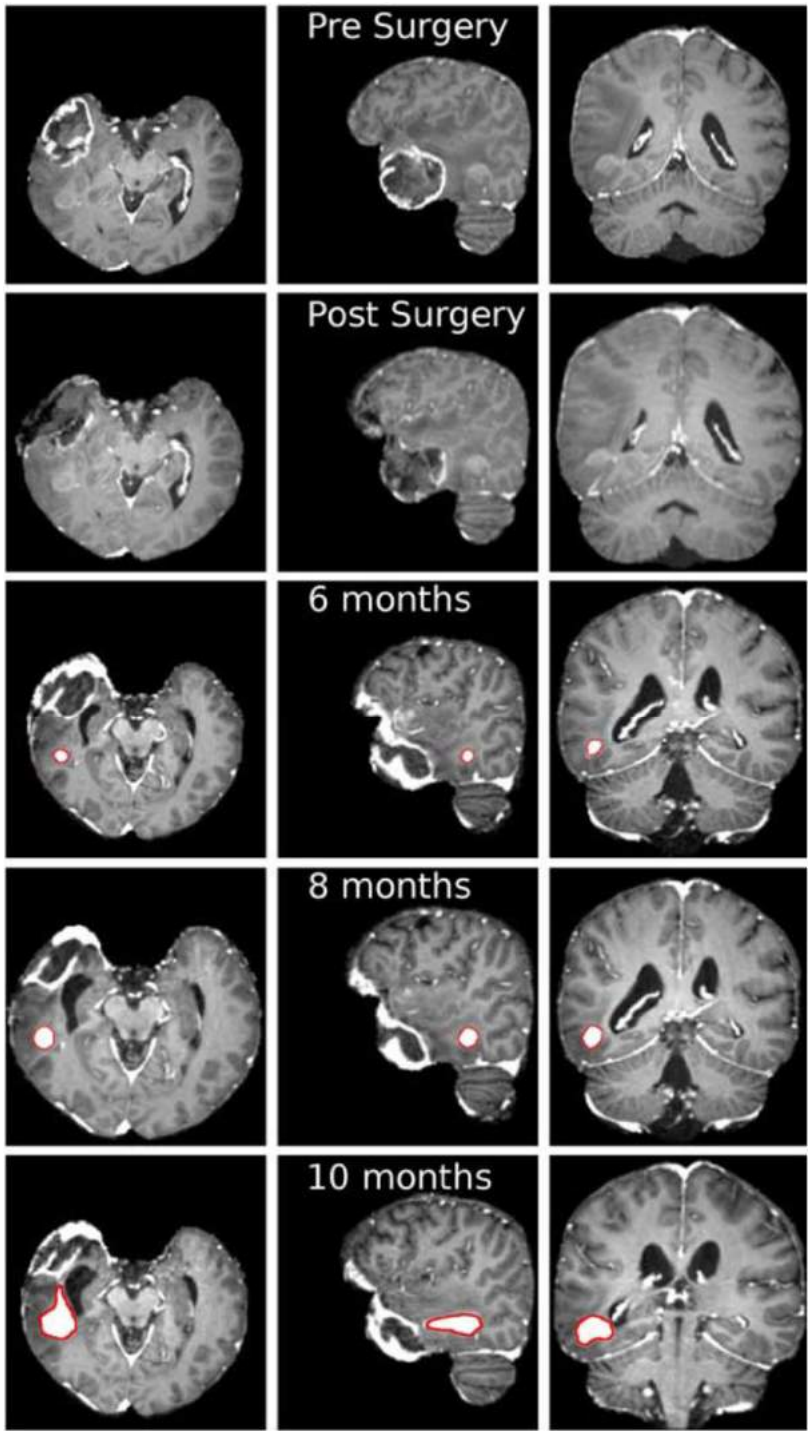

Iteration	$J(\mathcal{P}_0)$	L_0	ν_0	k_{n0}	S_{n0}	δ_{n0}	γ_0^2	E_0	δ_0	c_{e0}
k=0	0.32328	0.0002	0.08	2	10000	8640	0.1225	694	0.3	0.611

MRI FOM Comparison

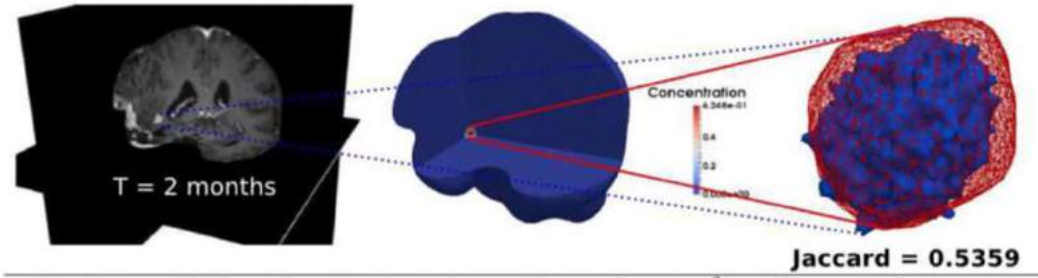

Iteration	$J(\mathcal{P}_1)$	L_1	ν_1	k_{n1}	S_{n1}	δ_{n1}	γ_1^2	E_1	δ_0	c_{e0}
k=1	0.08001	0.0002	0.02352	1.9769	9999.99	8640.00	0.1225	693.99	0.3237	0.5755

MRI FOM Comparison

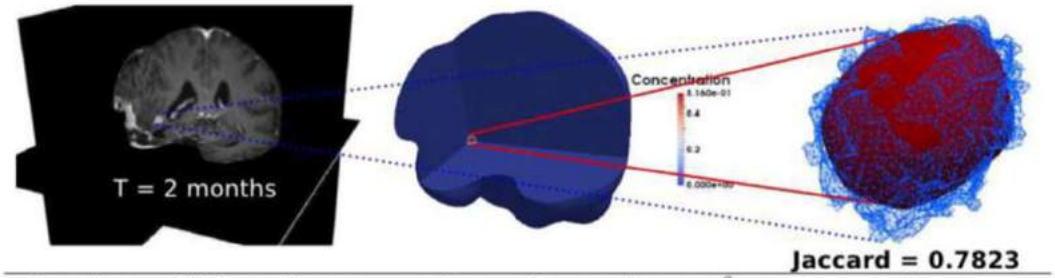

Iteration	$J(\mathcal{P}_2)$	L_2	ν_2	k_{n2}	S_{n2}	δ_{n2}	γ_2^2	E_2	δ_0	c_{e0}
k=2	0.07167	0.0002	0.0213	1.9842	10000.04	8639.95	0.1225	693.99	0.3271	0.611

MRI FOM Comparison

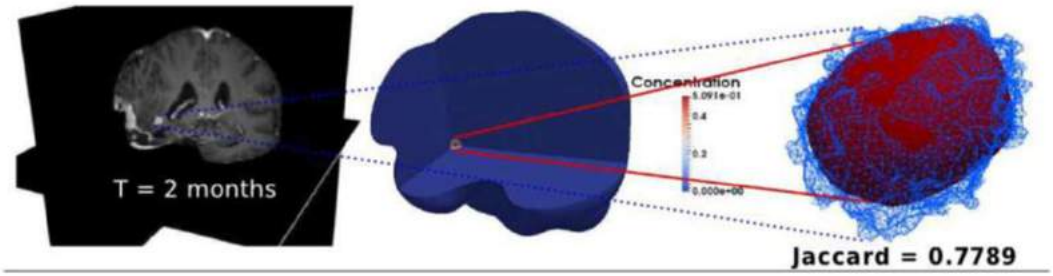

Iteration $k = 0$	**Step 1 201914.27**	**Step 2 12.42**	**Step 3 6281.31**	**Step 4 157.8289**
Iteration $k = 1$	Step 1 201425.71	Step 2 12.89	Step 3 2600.37	Step 4 587.07
Iteration $k = 2$	Step 1 213040.53	Step 2 11.44	Step 3 2544.43	Step 4 42.53

Application 2: recurrence prediction after surgery

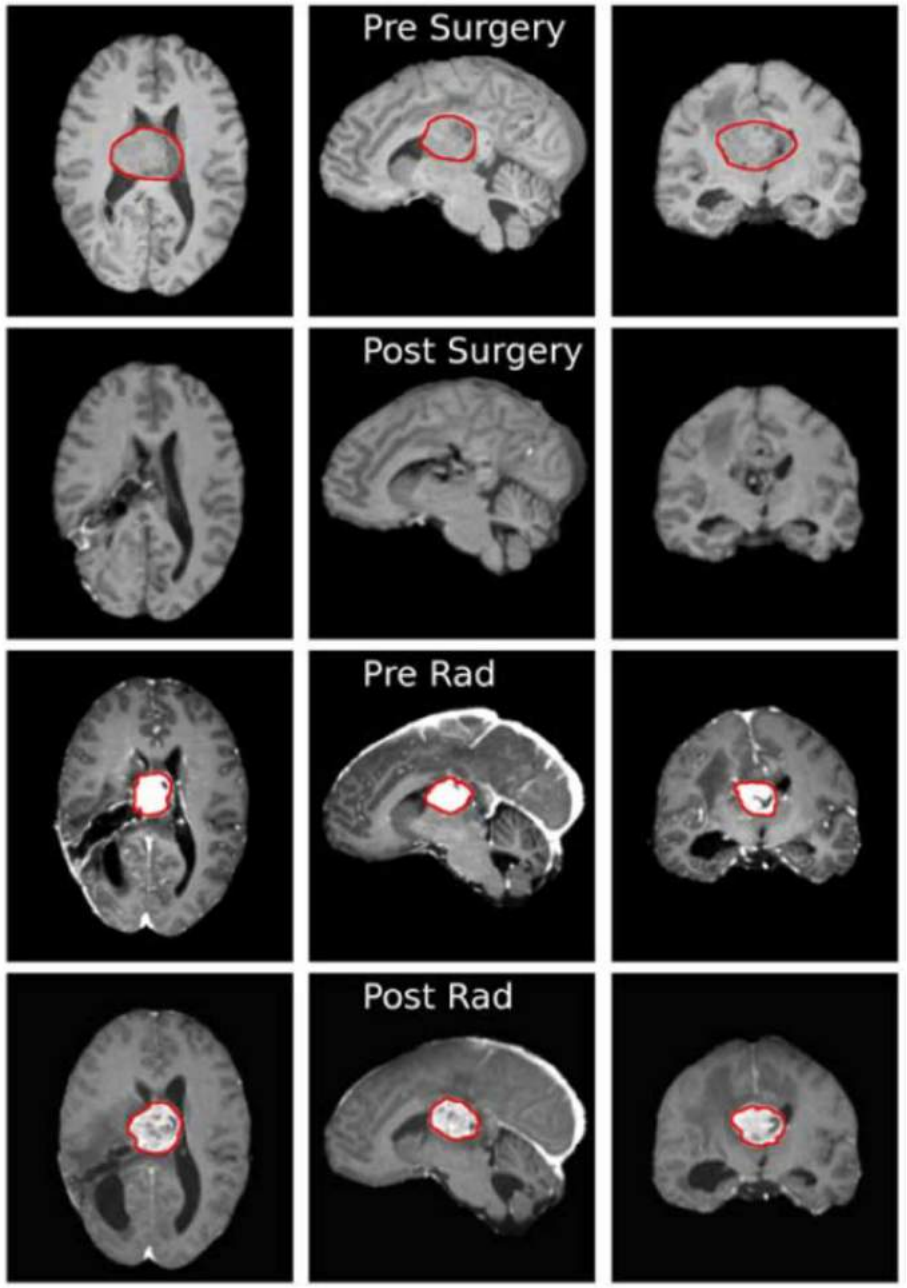

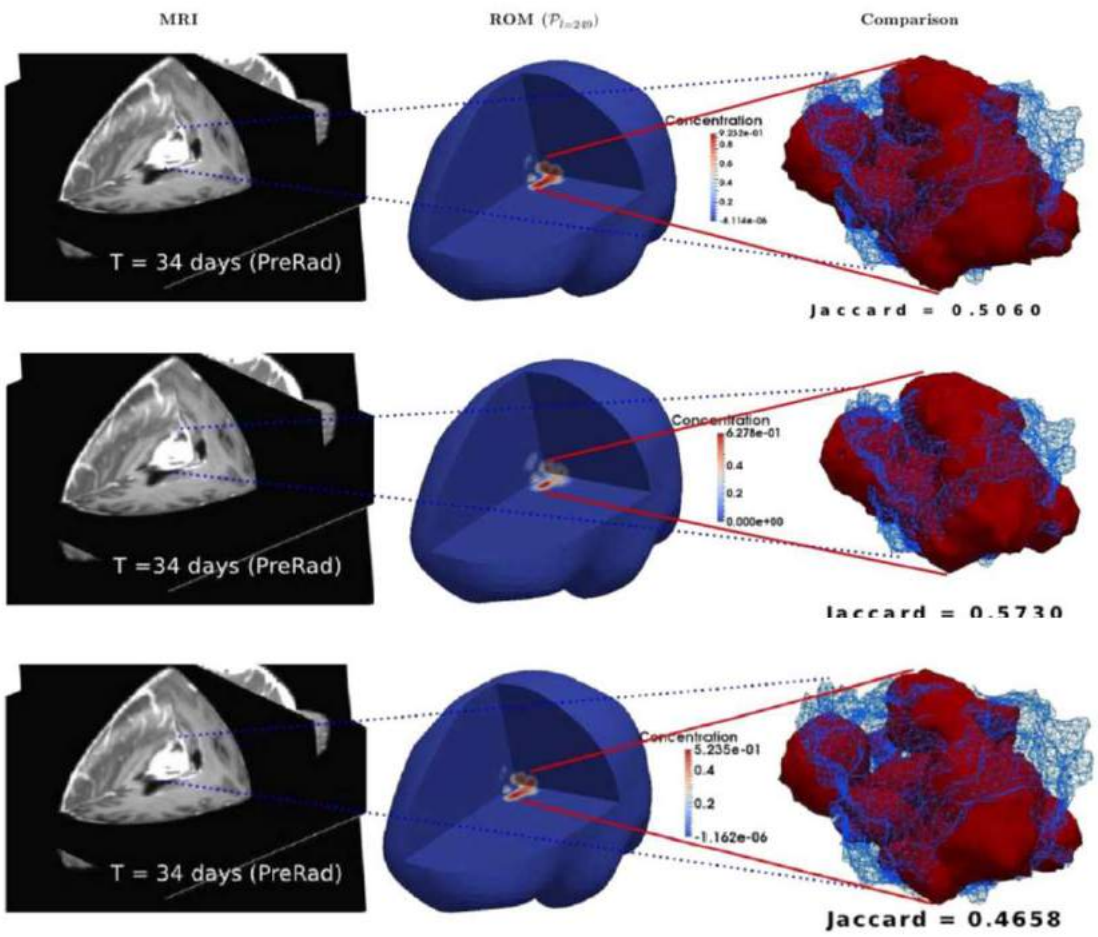

Iteration $k = 0$	**Step 1 144575.36**	**Step 2 8.58**	**Step 3 2438.42**	**Step 4 3431.52**
Iteration $k = 1$	Step 1 164645.5 Step 2 11.75	Step 3 6453.26	Step 4 336.09	
Iteration $k = 2$	Step 1 135222.43	Step 2 7.75	Step 3 2416.61	Step 4 45.14

Model and data fusion: a deep learning approach

The MOR reduces the computational complexity compared to the FOM, but the optimization algorithm may require many iterations to converge, which limits its usage in clinical settings.

Thus, we proposed a deep learning approach to achieve the same accuracy at a fraction of the computational cost of the ROM.

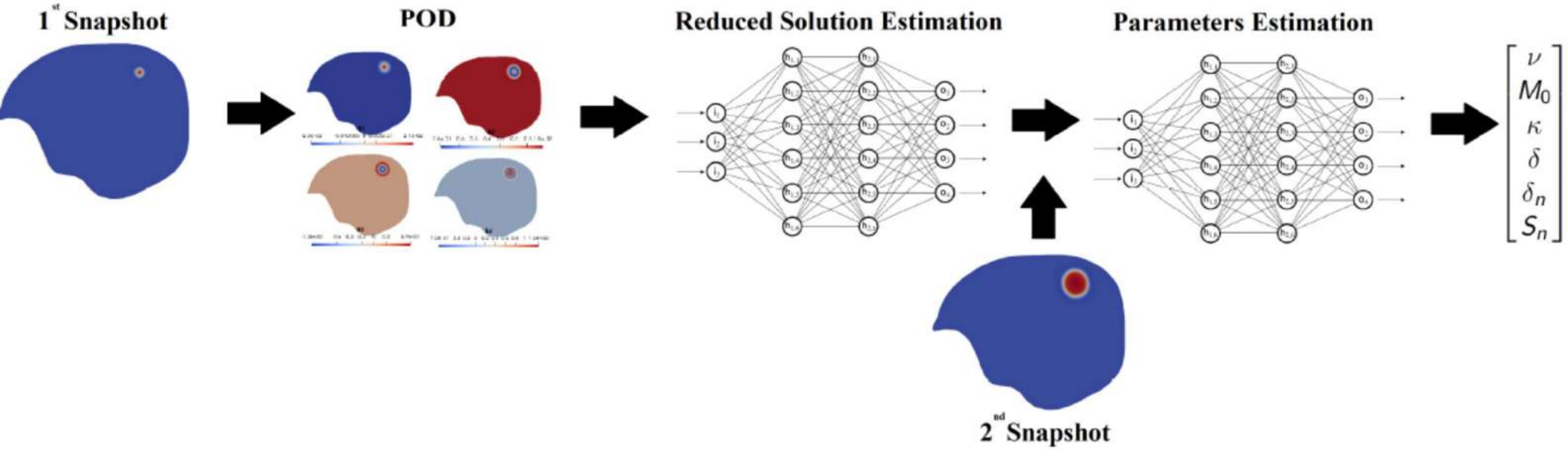

Neural networks and deep learning: basic concepts

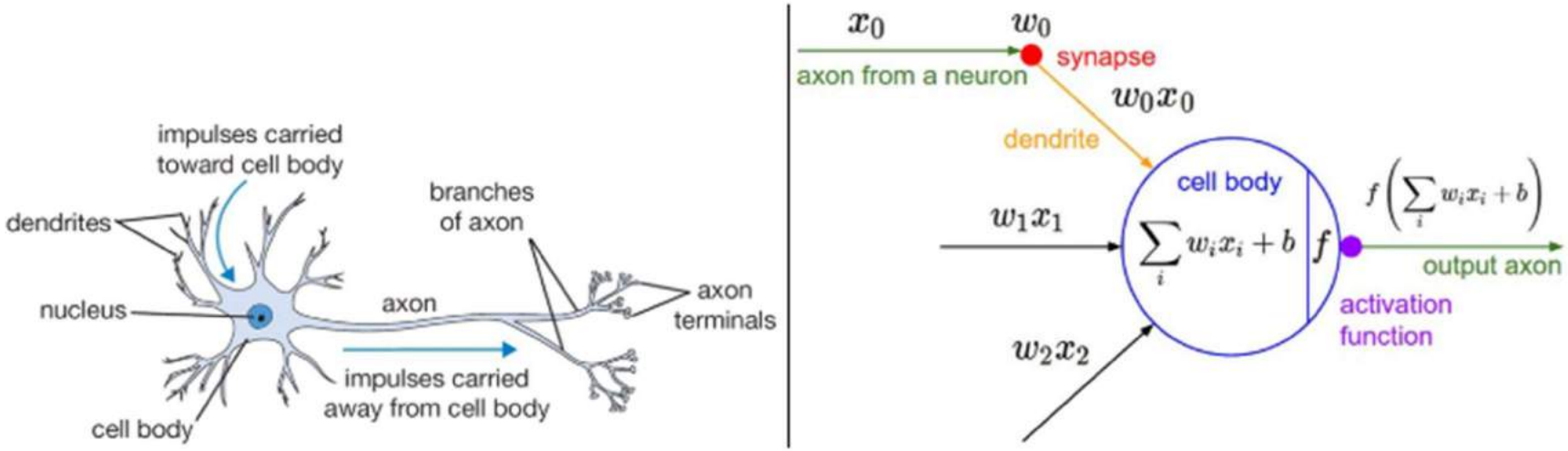

A cartoon drawing of a biological neuron (left) and its mathematical model (right).

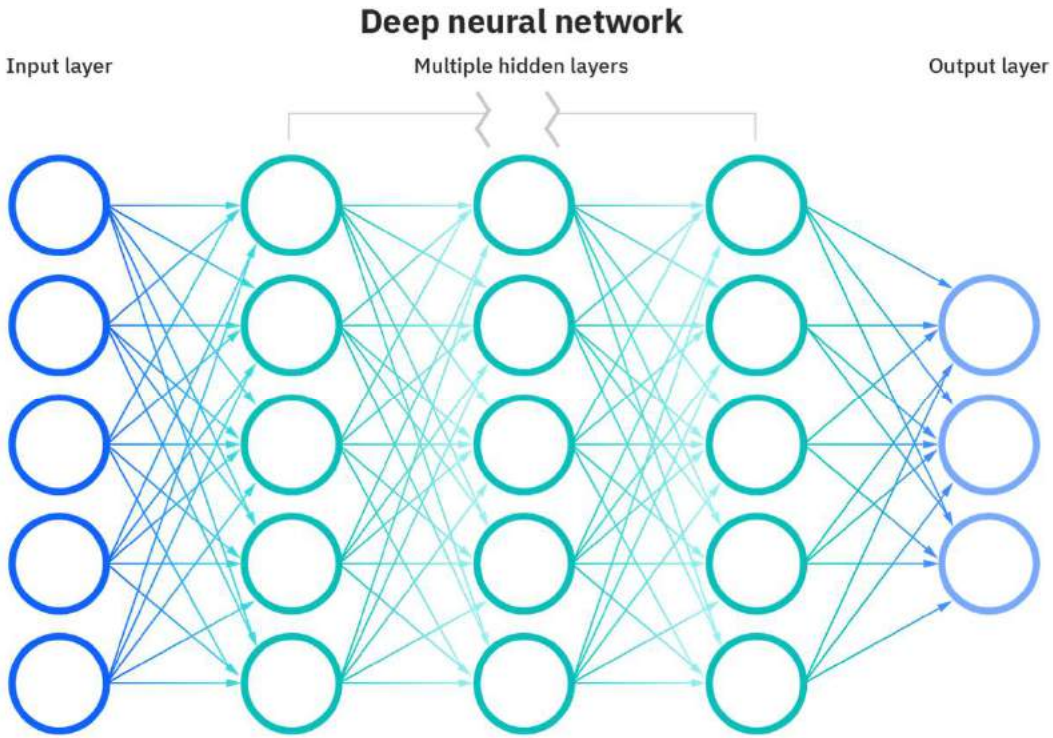

Direct problem: learning the ROM solution

The neural network $\mathbf{NN}_\phi$ approximate the map between the **parameters of the model** at a specific time t and the **coefficients of the reduced solution** at that time instant.

$$\begin{bmatrix} \nu \\ M_0 \\ \kappa \\ \delta \\ \delta_n \\ S_n \\ t \end{bmatrix}$$

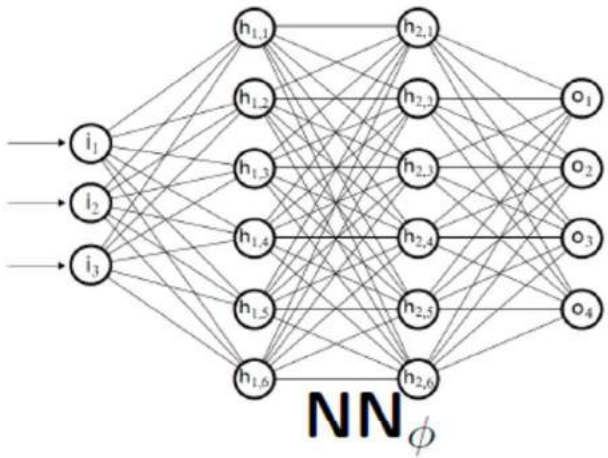

$$\begin{bmatrix} a_1^t \\ a_2^t \\ \vdots \\ a_{N_{\text{POD}}-1}^t \\ a_{N_{\text{POD}}}^t \end{bmatrix}$$

- **Propagation function**: $f_{\text{prop}} = \sum_{k=1}^{m} w_{s_k,j} y_{s_k}$
- **Actvation function**: $\text{LeakyReLU}(x) = x\,\mathbb{I}_{x\geq 0} + 0.1x\,\mathbb{I}_{x<0}$
- **Output function** is the identity function
- 3 **lavers** with **100 neurons** each

Inverse problem: patient-specific parameter estimation

The small number of d.o.f for the reduced-ordel model justify the idea of training a neural network for estimating the parameters of the model.

The neural network $\mathbf{NN}_{\text{inv}}$ approximate the map between the **coefficients of a pair of reduced solutions** and the **parameters of the model that entail that evolution** at that time instant.

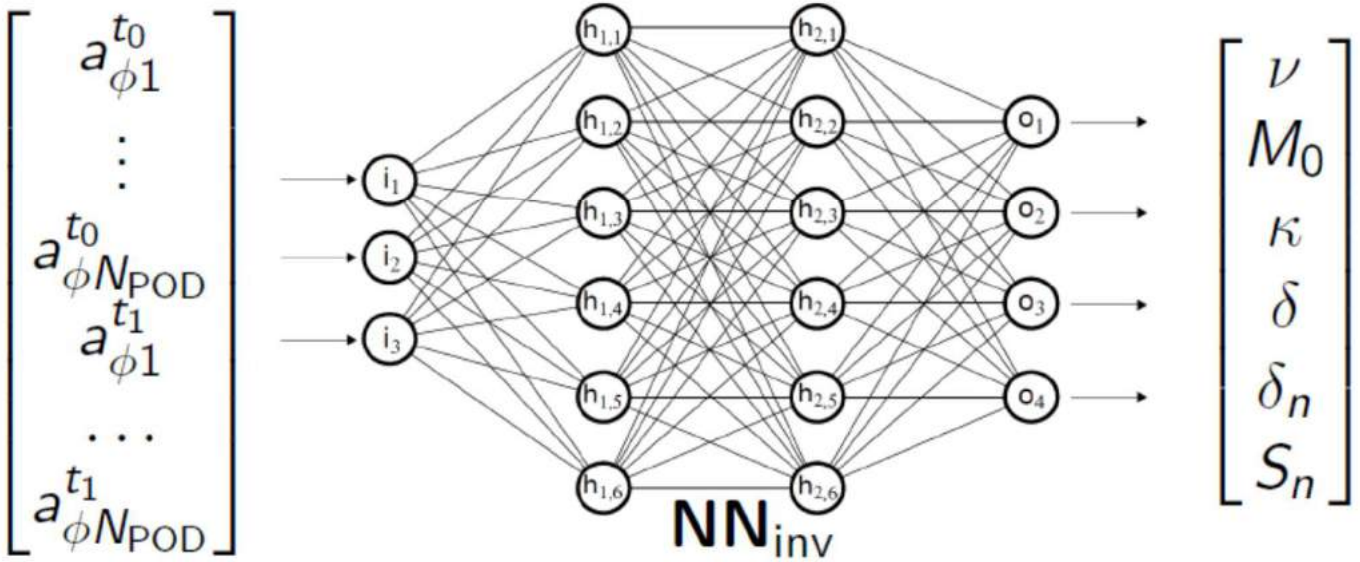

FOM versus NN solution: estimated volume

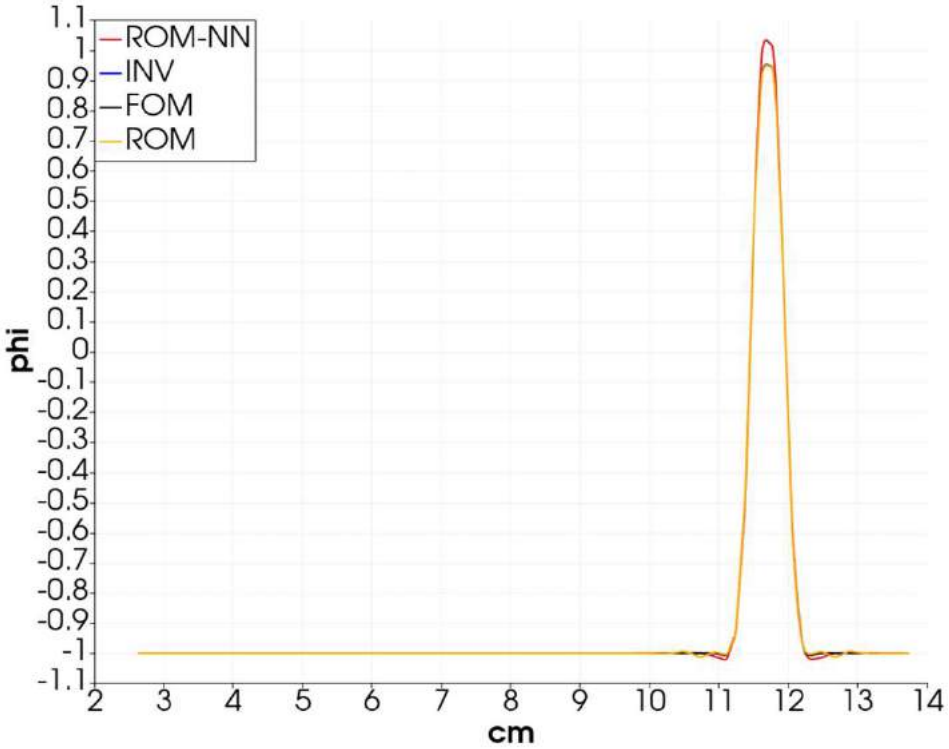

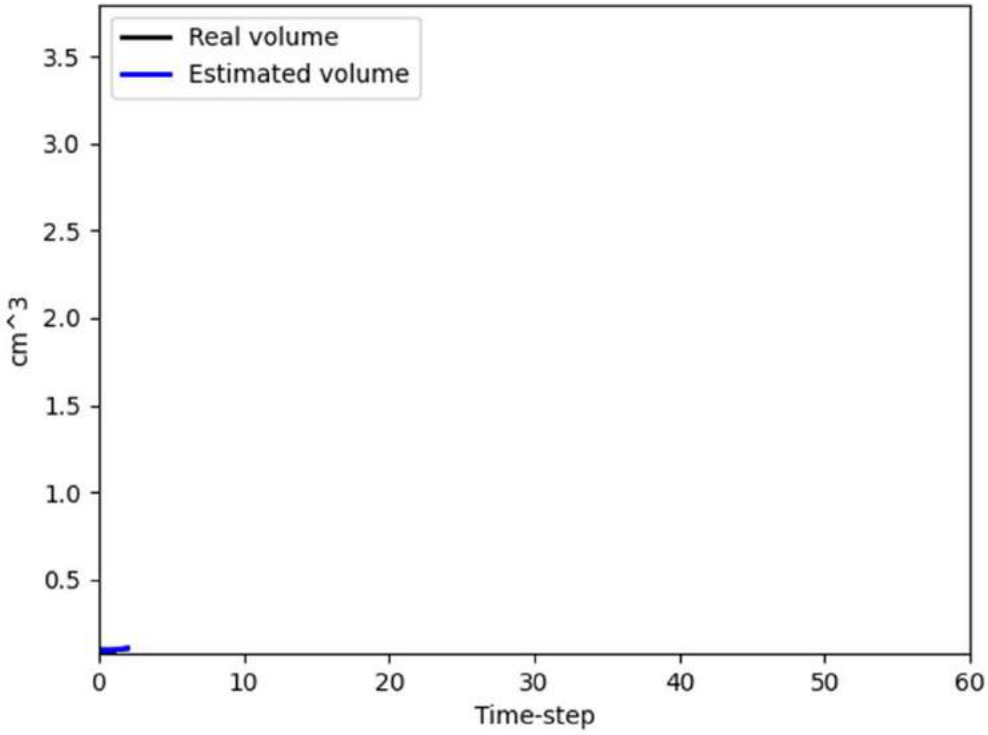

- Number of parameters set for the base construction $\mathbf{M = 64}$
- Number of elements in the base $\mathbf{N_{POD} = 40}$
- Number of simulations $\mathbf{N_S = 750}$

FOM versus NN solution: computational effort

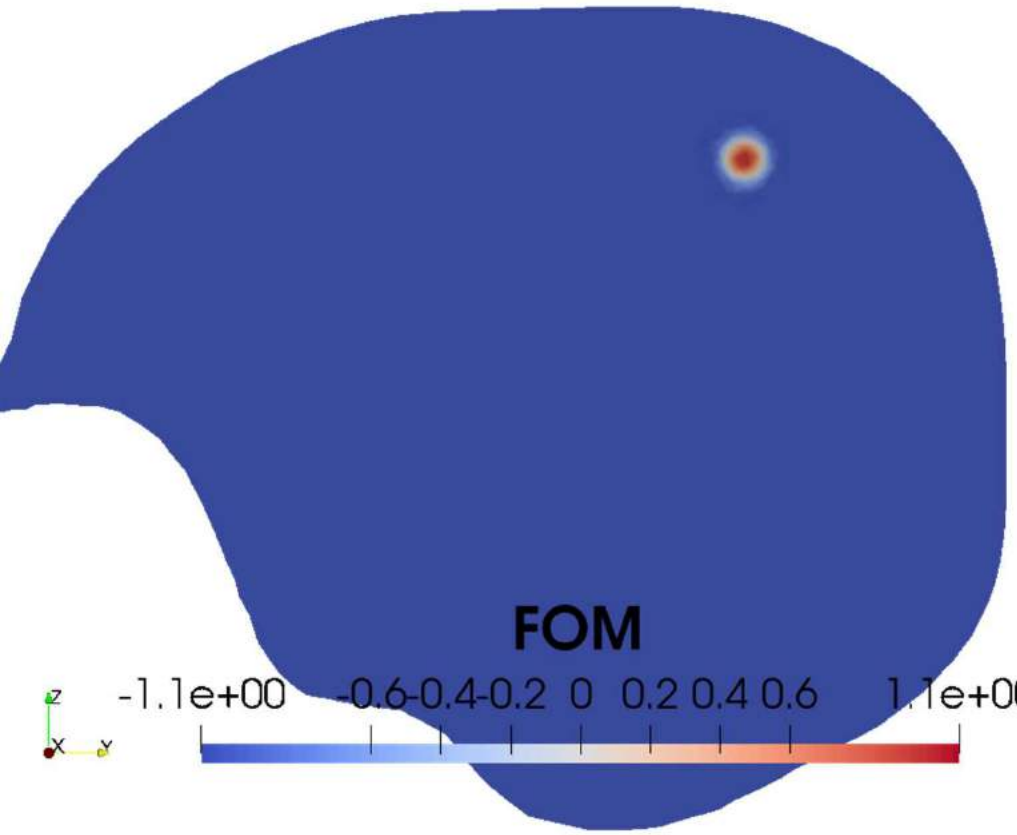

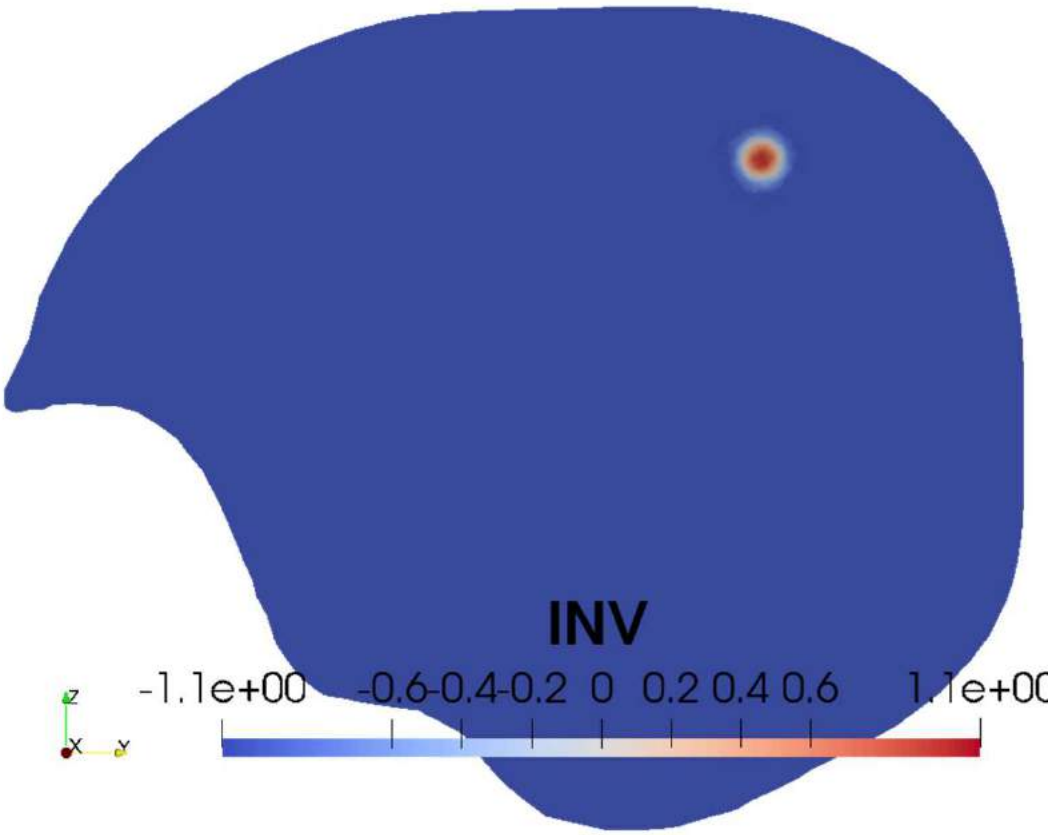

Simulation	Elapsed time
Full Order Model	920 s
Reduced Order Model	5190 s
Reduced Order Model - Neural Network	5 s
Parameter Estimation	5 s

Acknowledgements

Collaborators:

Donato Cerrone
Giulia Pozzi — **MOX**, Politecnico di Milano
Davide Riccobelli
Paolo Zunino
Beatrice Grammatica
Andrea Manzoni

Giorgio Scita, Stefano Marchesi — **IFOM**
Francesco Acerbi, Alberto Bizzi — **IRCSS Besta**

Funding

MFAG AIRC Grant, INSERM CancerPhysics
MIUR PRIN 2017 + PRIN 2020 + Dipartimento di Eccellenza 2023-2027
Regione Lombardia, NEWMED project

NEW TRENDS IN BIOMATHEMATICS

Applications in Oncology and Immunology

ONE-DAY WORKSHOP
June 21, 2024, 8:30 a.m.

Aula Magna - Ingegneria "*Italo Falcomatà*"
Università degli Studi Mediterranea
Via R. Zehender, 1 - Reggio Calabria

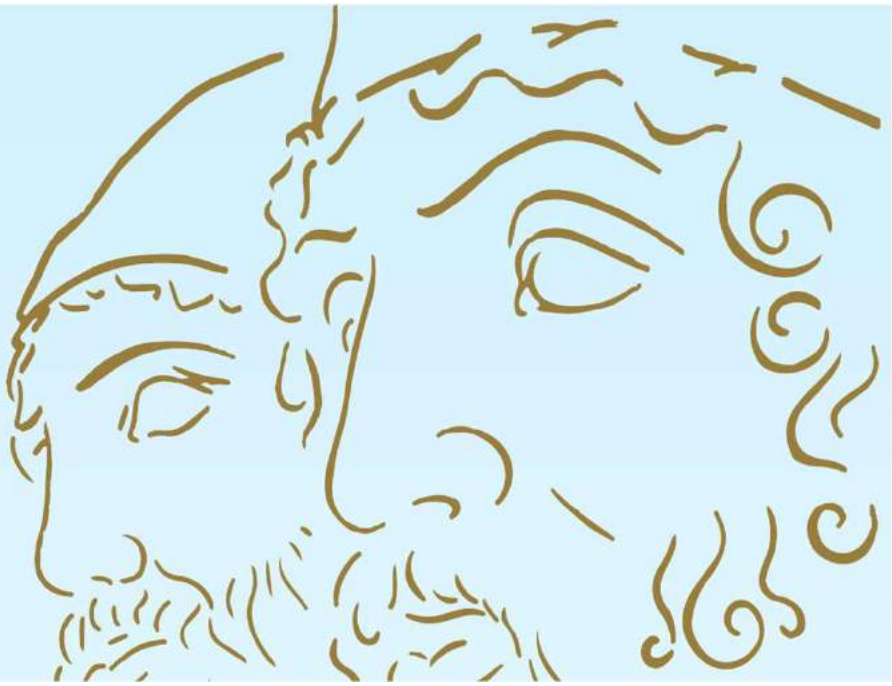

T cell therapy against cancer: A predictive diffuse-interface mathematical model informed by pre-clinical studies

Pasquale Ciarletta

MOX Laboratory, Dept. Mathematics, Politecnico di Milano

CNRS, Sorbonne Université, Paris

MODELLISTICA E CALCOLO SCIENTIFICO
MODELING AND SCIENTIFIC COMPUTING

POLITECNICO MILANO

5 Types of Cancer Immunotherapy Treatments

VS Hospitals™
Care. Cure. Compassion.

Monoclonal Antibodies (MABS)

01

- Immune system can recognize cancer cells that it wasn't able to previously.
- Over 75 drugs approved to date.

Immune - Checkpoint Inhibitors

02

- Releases immune system's molecular brakes called "checkpoints".
- At least 6 drugs approved so far.

Cancer Vaccines

03

- Two types; Preventative and treatment.
- Possibly will use artificial intelligence for personalized medicine.

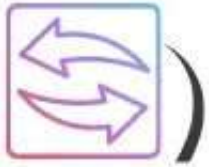

Adoptive Cell Transfer (ACT)

04

- Pretty new with only two drugs approved.
- Uses gene editing.

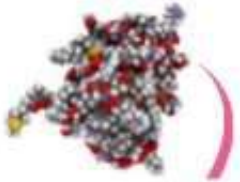

Cytokines

05

- Man made versions of some proteins that boost immune system.
- Kind of complicated stuff.

The 3R principle in medical research

Replace

An animal experiment is only approved if no suitable alternative method exists, such as computer simulations or cell culture experiments.

Reduce

Only the smallest number of animals necessary for an experiment may be used. A clever study design provides a statistically significant result with a minimum number of animals.

Refine

Housing and experimental conditions are being constantly optimized in order to subject laboratory animals to as little stress as possible. This includes always choosing the most animal-friendly experimental method, promoting non-invasive procedures, and treating any pain the animal may be in.

In-silico modeling for boosting 3R

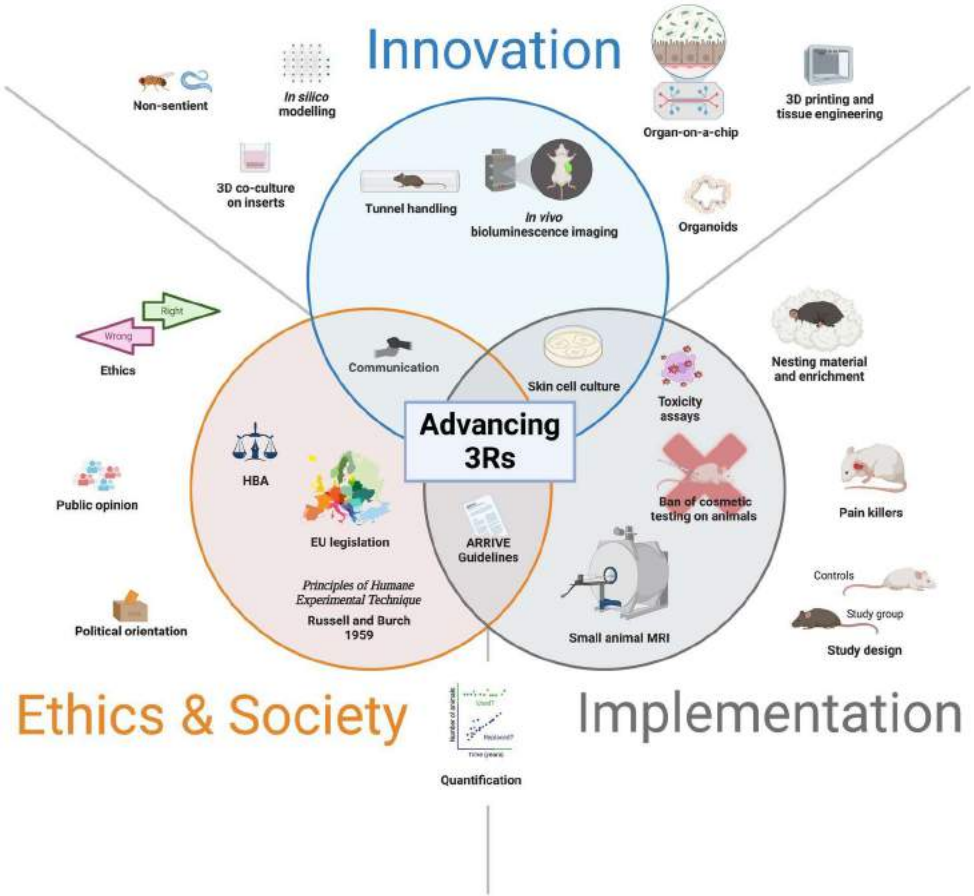

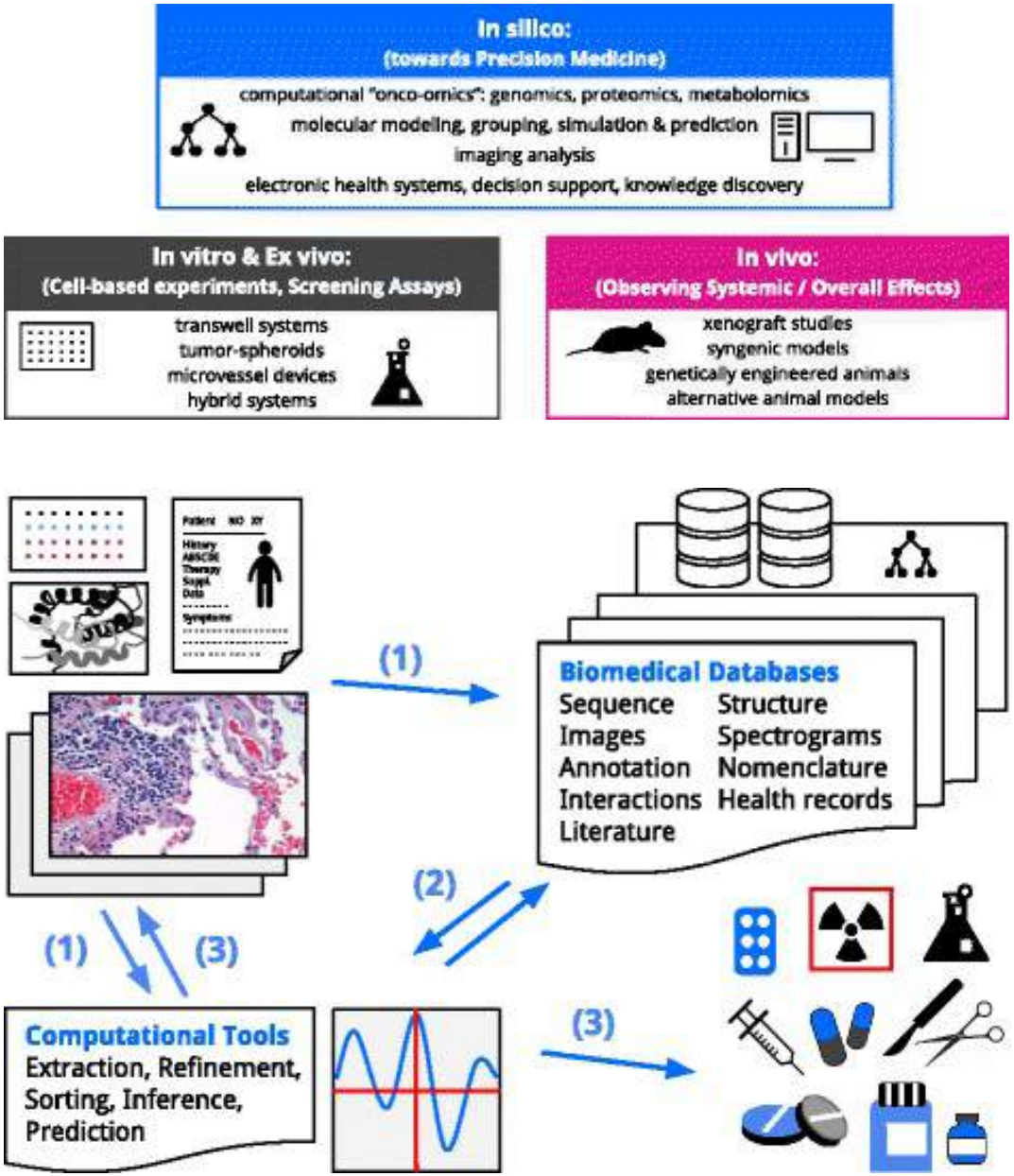

Adoptive cellular immunotherapy

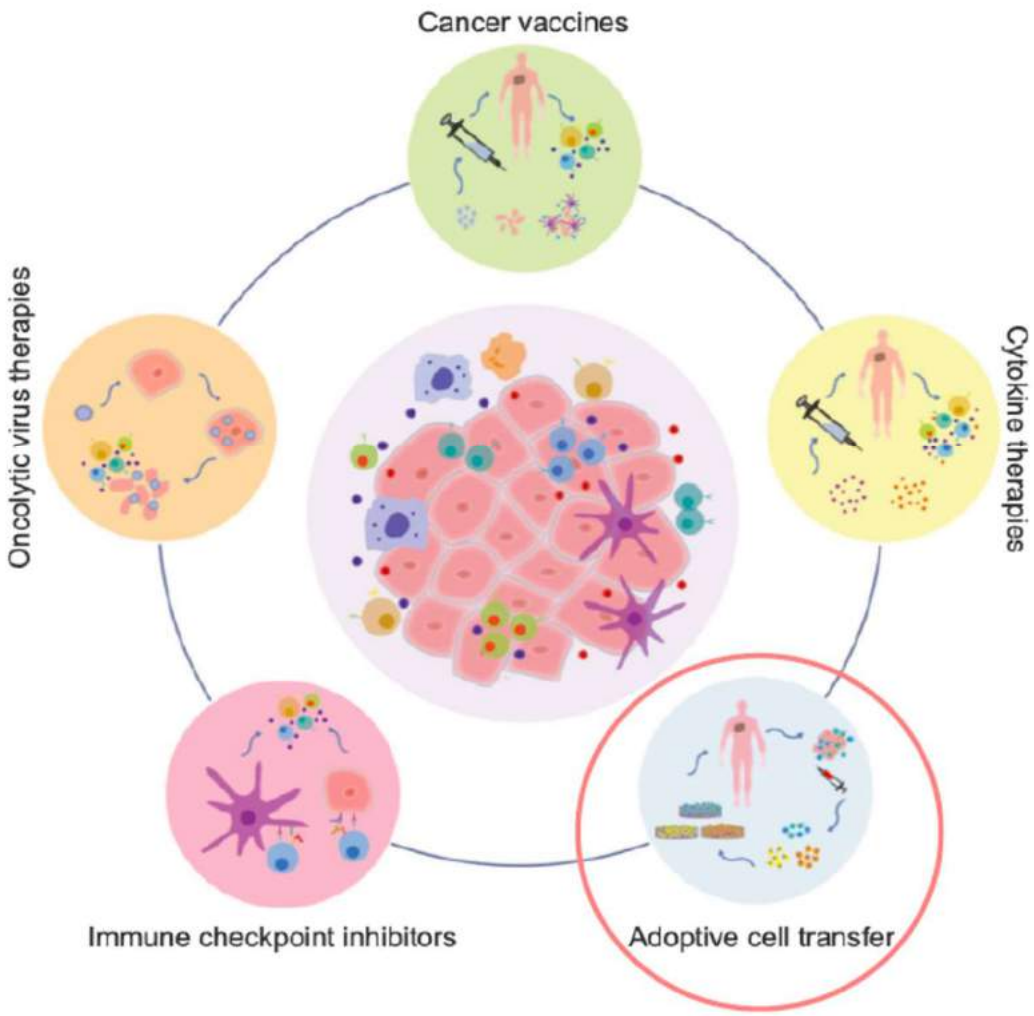

The therapy is based on the use of a specific type of immune system cells, called *T lymphocytes*.

Main steps of adoptive cell therapy:

- T lymphocytes isolation from the patient
- Cell expansion and genetic manipulations
- Re-infusion back to the patient

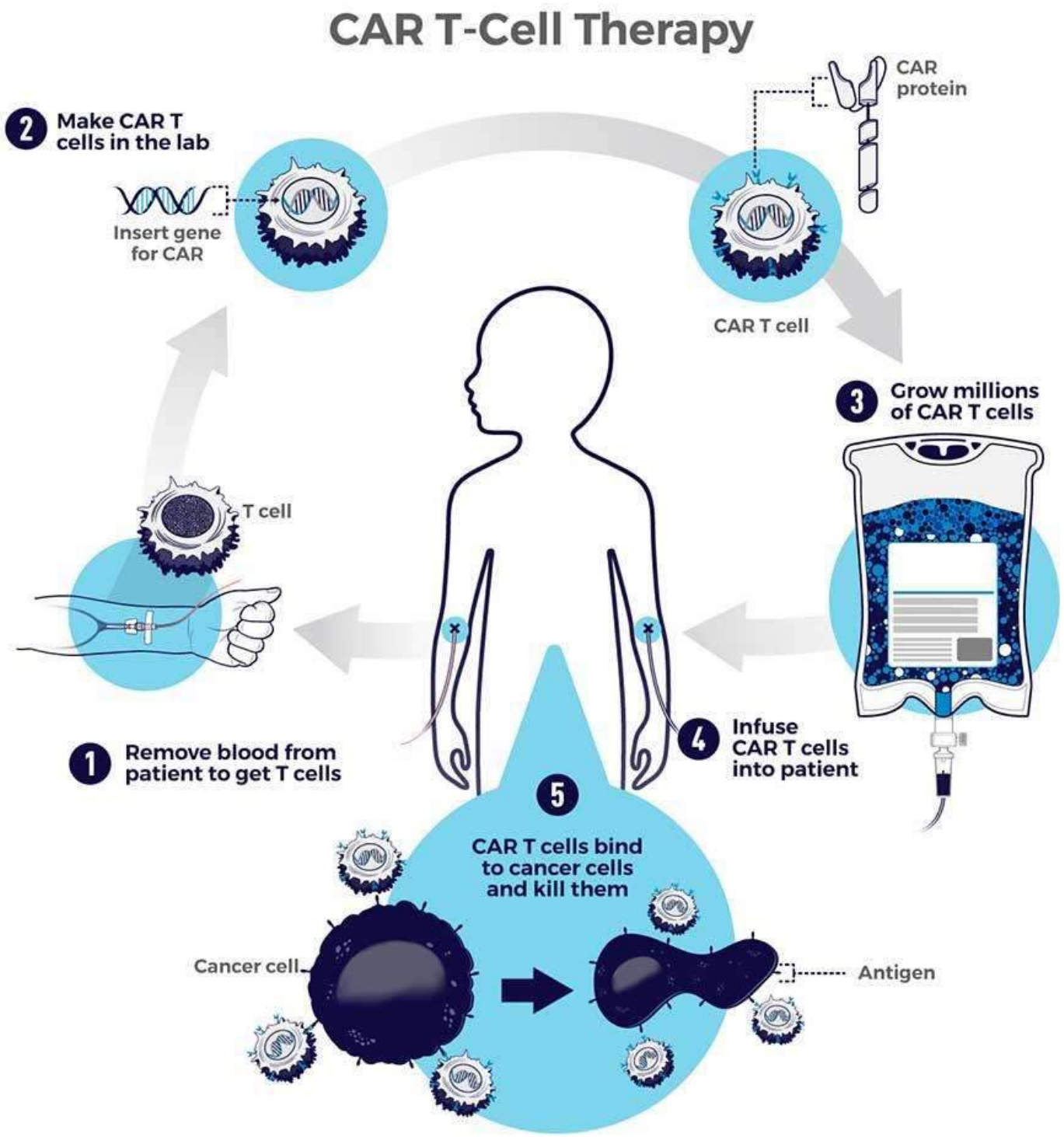
CAR T-Cell Therapy
CAR protein
2 Make CAR T cells in the lab
Insert gene for CAR
CAR T cell
3 Grow millions of CAR T cells
T cell
1 Remove blood from patient to get T cells
4 Infuse CAR T cells into patient
5
CAR T cells bind to cancer cells and kill them
Cancer cell
Antigen

Clinical collaboration

- Anna Mondino (*head of lymphocytes activation unit*)
- Linda Chaabane (*coordinator of 7T pre-clinical imaging facility*)

I.R.C.C.S. Ospedale San Raffaele
Gruppo San Donato

28 mm x 20 mm

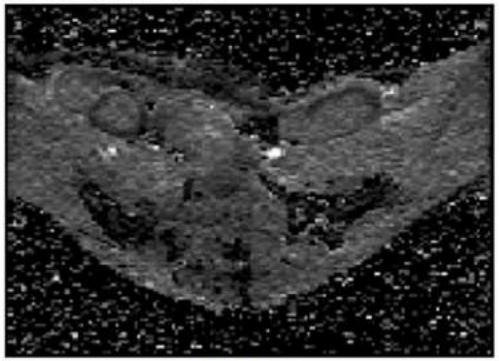

DWI

28 mm x 20 mm

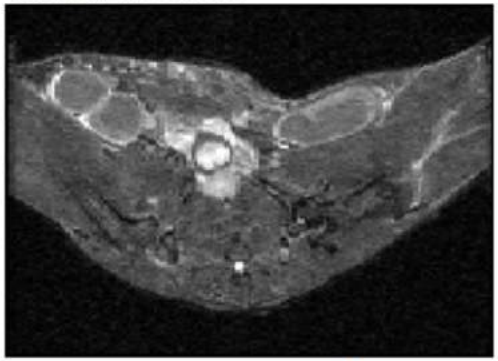

transverse slice

35 mm x 35 mm

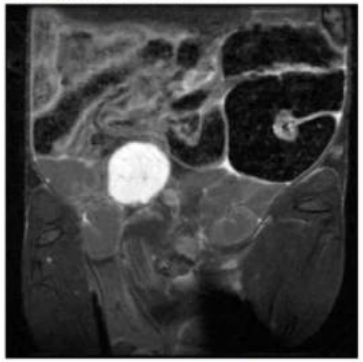

coronal slice

22 mm x 30 mm

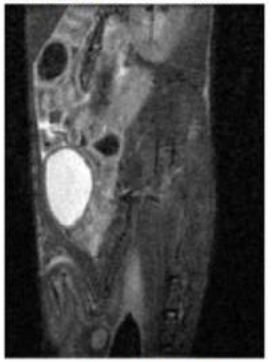

sagittal slice

→ tumor site detection

→ image segmentation

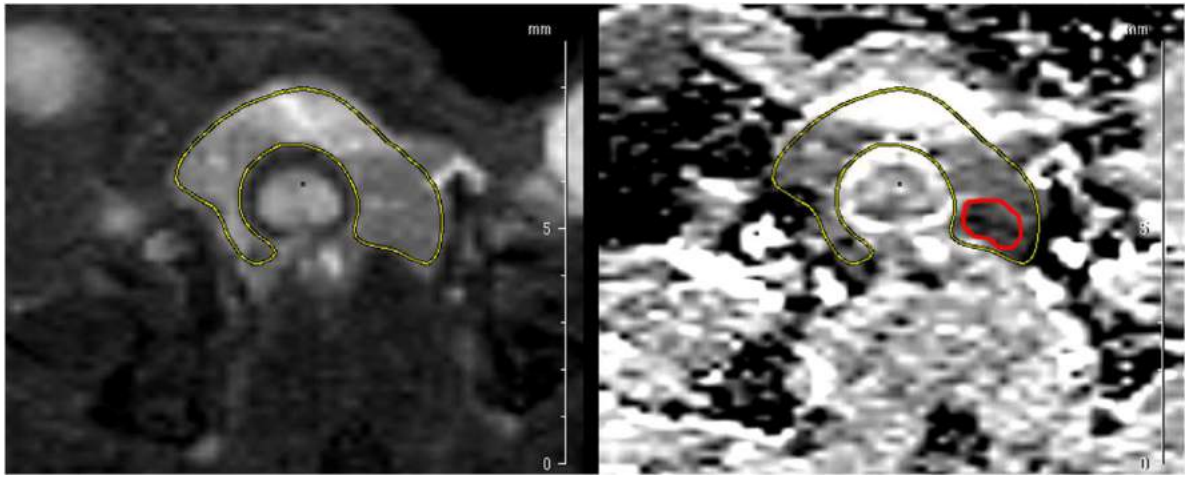

The chemo-physical fields

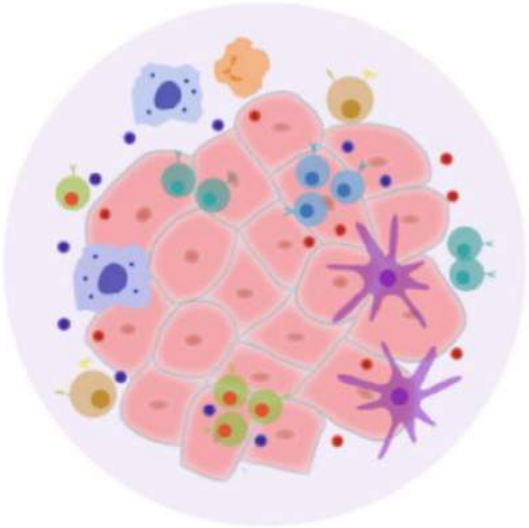

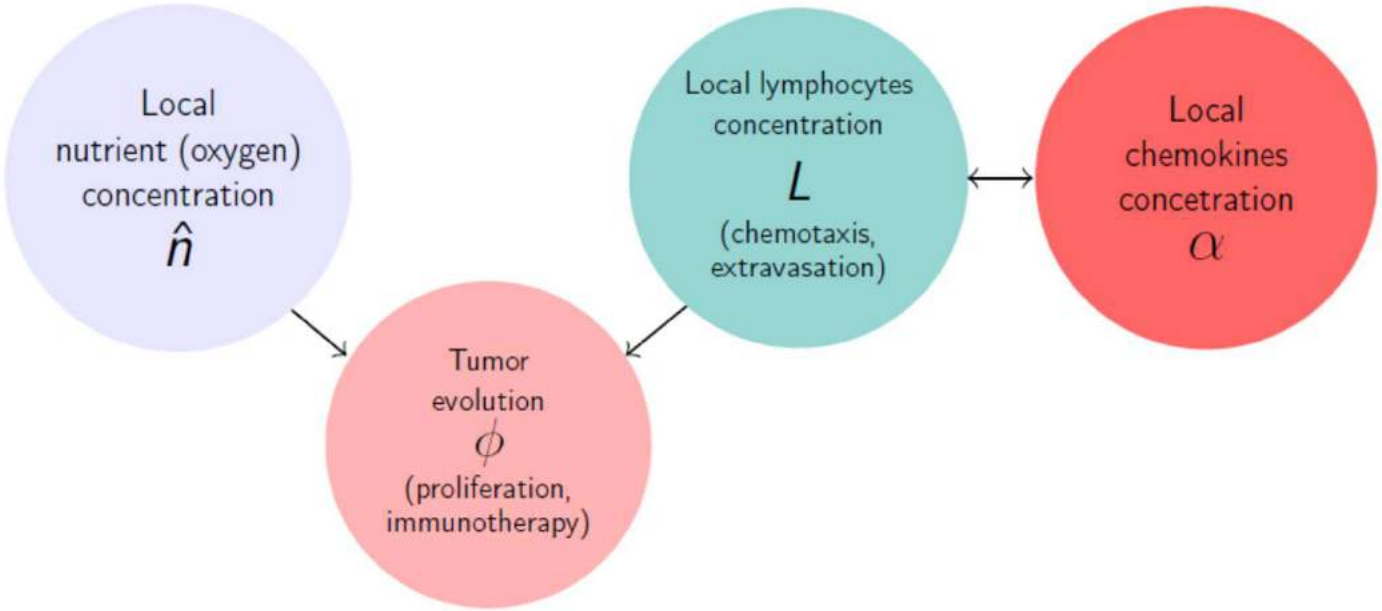

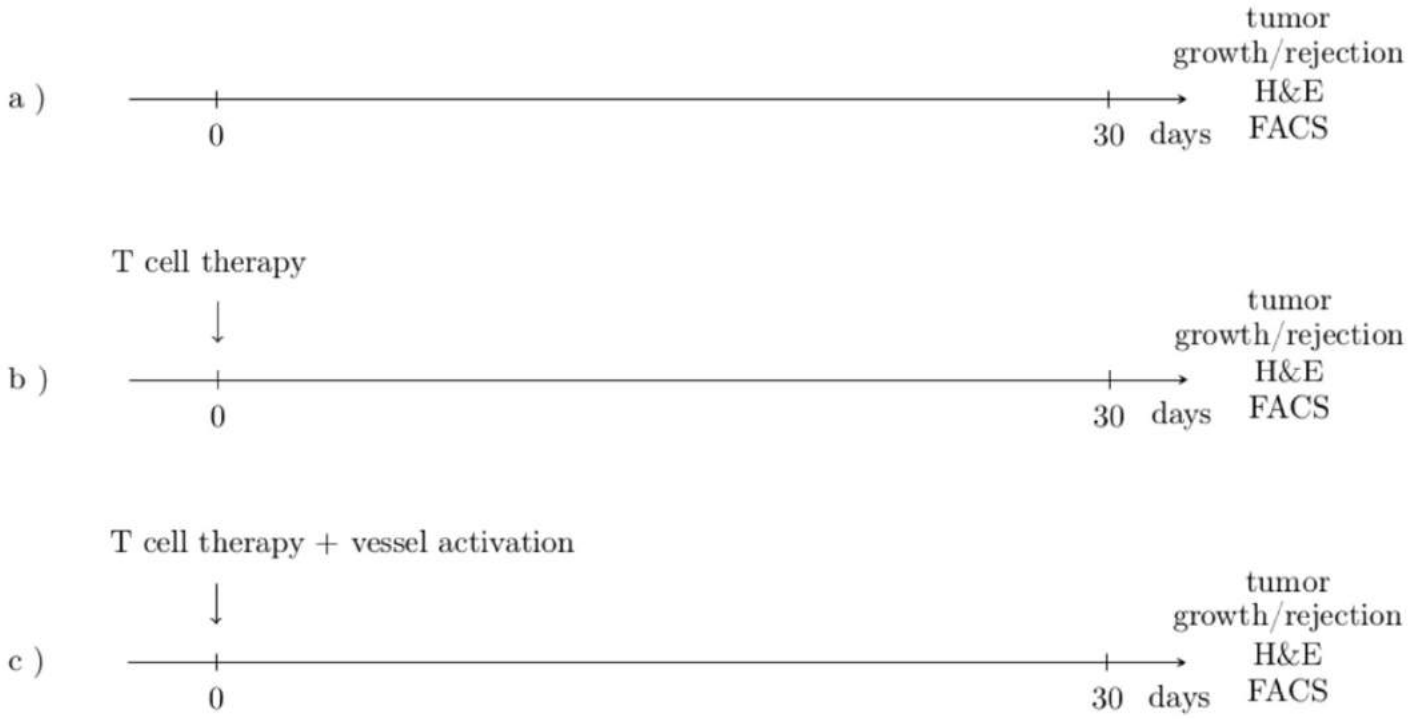

Balance equation for the tumour mass

In absence of therapy, the growth tumor mass:

- is regulated by the local interactions among healthy and tumor cells;
- is favored where there is an abundance of oxygen (peripheral ring);
- is limited where there is a lack of oxygen (core).

$$\begin{cases} \frac{\partial \phi}{\partial t} = \nabla \cdot (m(\phi)\nabla \mu) + \frac{\Gamma}{\gamma} \\ \mu = \kappa \Psi'(\phi) - \epsilon^2 \Delta \phi \end{cases}$$

The term Γ depends on tumor cells metabolism:

$$\Gamma = \nu\gamma\left(\frac{n}{n_s} - \delta\right)h(\phi) = \nu\gamma\left(\hat{n} - \delta\right)h(\phi)$$

where $h(\phi) = \frac{1}{2}(1 + \phi)$ defines the tumor region.

Reaction-diffusion equations for other chemical species

The nutrient:

- is released by the capillaries into the organ;
- diffuse against the concentration gradient;
- is consumed by the tumor;

$$\frac{\partial \hat{n}}{\partial t} = \underbrace{\nabla \cdot (D_n \nabla \hat{n})}_{\text{diffusion}} + \underbrace{S_n(1-\hat{n})\frac{1}{3}(2-\phi)}_{\text{release}} - \underbrace{\delta_n \hat{n} h(\phi)}_{\text{consumption}}$$

In order to reproduce the mechanism of action of the adoptive cell therapy, we introduce a new *Michaelis-Menten* type term $I(\phi, t)$ in the evolution equation for ϕ:

$$I(\phi, t) = k_f(t)h(\phi) = d\frac{\hat{L}^\lambda}{\xi(\hat{V}) + \hat{L}^\lambda}h(\phi)$$

where $\hat{L} = \dfrac{L}{L_i}$ and $\xi(\hat{V}) = s\hat{V}^\lambda = s\left(\dfrac{V}{V_0}\right)^\lambda$.

Physical parameters for tumour growth and oxygen diffusion

	Parameter description	Value	Ref or formula
ν	Tumor cells proliferation rate	0.17 - 0.25 day^{-1}	[44]
M_0	Tumor inter-phase friction	1.37 - 3.99 (kPa·day)/mm^2	[45]
r	Tumor cell radius	0.01 mm	[46]
χ	Tumor interstitial fluid pressure	1553.2 Pa	[47]
ϵ	Diffuse interface thickness	0.79 mm·$\sqrt{\text{Pa}}$	$2\text{r}\sqrt{\chi}$
κ	Prostate Young modulus	$6.227 \cdot 10^4$ Pa	[48]
δ	Hypoxia threshold	0.15	[49]
D_n	Oxygen diffusion coefficient	155.52 mm^2/day	[49]
l_n	Oxygen penetration distance	0.1 mm	[50]
δ_n	Oxygen consumption rate	15552 day^{-1}	D_n/l_n^2
n_s	Oxygen concentration in vessels	0.07 mM	[51]
S_n	Oxygen supply rate	10^4 day^{-1}	[52]

Table 1: Values or ranges of values for the physical parameters in the tumor model.

Reaction-diffusion equations for lymphocytes and chemokines

The local concentration of the lymphocytes depends on:

- the diffusion phenomenon;
- the exchange with the vessels regulated by the chemokines concentration;
- the movement of lymphocytes towards highly inflamed regions.

The local concentration of chemokines, in turn, depends on the lymphocytes concentration.

$$\frac{\partial L}{\partial t} = D_L \Delta L - \underbrace{\nabla \cdot \left(\frac{\chi L}{(\beta + \alpha)^2} \nabla \alpha \right)}_{\text{chemotaxis}} + \underbrace{S_L \frac{\alpha - \alpha_i}{\alpha} [L - L_r]_+}_{\text{extravasation/uptake}}$$

$$\frac{\partial \alpha}{\partial t} = D_\alpha \Delta \alpha + \underbrace{L h(\phi)}_{\text{production}} - d_\alpha \alpha$$

Physical parameters for immune-system dynamics and therapy

	Parameter description	Value	Ref
D_L	Lymphocytes diffusion coefficient	$7 \cdot 10^{-3}$ mm^2/day	[53]
χ	Lymphocytes chemotactic coefficient	$2 \cdot 10^1$ molecules/(mm·day)	[-]
β	Sensitivity function parameter	10^3 molecules/mm^3	[-]
S_L	Lymphocytes release/uptake rate	0.08 - 0.45 day^{-1}	[-]
α_i	Inflammation threshold	$6.022 \cdot 10^2$ molecules/mm^3	[-]
L_r	Lymphocytes reference value	$5 \cdot 10^2$ cells/mm^3	[-]
D_α	Chemokines diffusion coefficient	0.01 - 1 mm^2/day	[53]
k_α	Chemokines production rate	$2.88 \cdot 10^4$ - $4.32 \cdot 10^6$ molecules/(cells·day)	[53]
d_α	Chemokines consumption rate	$1.155 \cdot 10^{-2}$ day^{-1}	[53]

Table 2: Values or ranges of values related to the local immune-system dynamics.

	Parameter description	Value	Ref
d	Saturation level of fractional tumor cell kill	1.43 - 7.9 day^{-1}	[40–42]
λ	Exponent of fractional tumor cell kill	0.12 - 0.9	[40–42]
s	Steepness coefficient of fractional tumor cell kill	0.14 - 5.07	[40–42]
L_i	Critical T cell concentration	$4 \cdot 10^4 - 6 \cdot 10^4$ cells/mm^3	[18]

Table 3: Ranges of values referred to the tumor lysis process by means of the therapy.

Numerical implementation

We extract the geometry from the MRI images by processing them via *3DSlicer* (image segmentation) and *VMTK toolkit* (geometry and mesh generation).

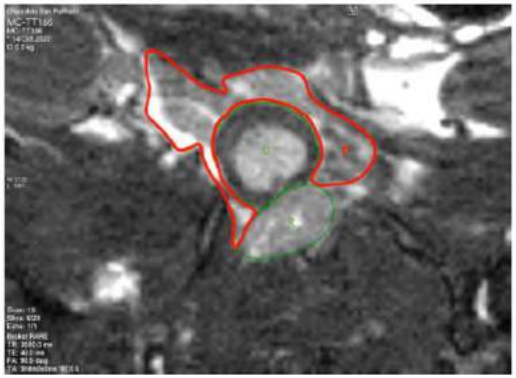

Prostate profile (red) from MRI.

Mesh: $\simeq 2 \cdot 10^5$ elements.
Geometry: 6.6 mm x 4.7 mm x 1.4 mm.

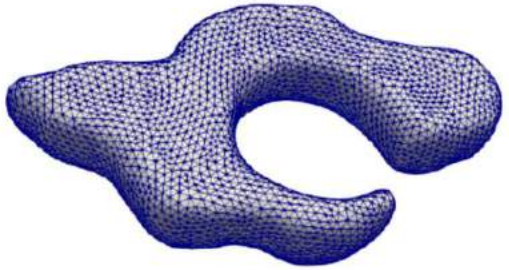

3D geometry with surface mesh

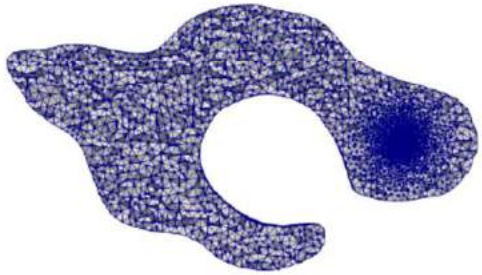

Internal mesh refined in the tumor site

0. extract tumor shape and position from the imaging data;

while(t $\leq$ 30 days):

1. solve the evolution eq. for the chemokines concentration;
2. solve the evolution eq. for the lymphocytes concentration;
3. compute the **immunotherapy** contribution;
4. solve in monolithic way the tumor and oxygen equations;
5. update time and tumor field.

Simulation results

Simulation results: tumour and nutrient concentrations

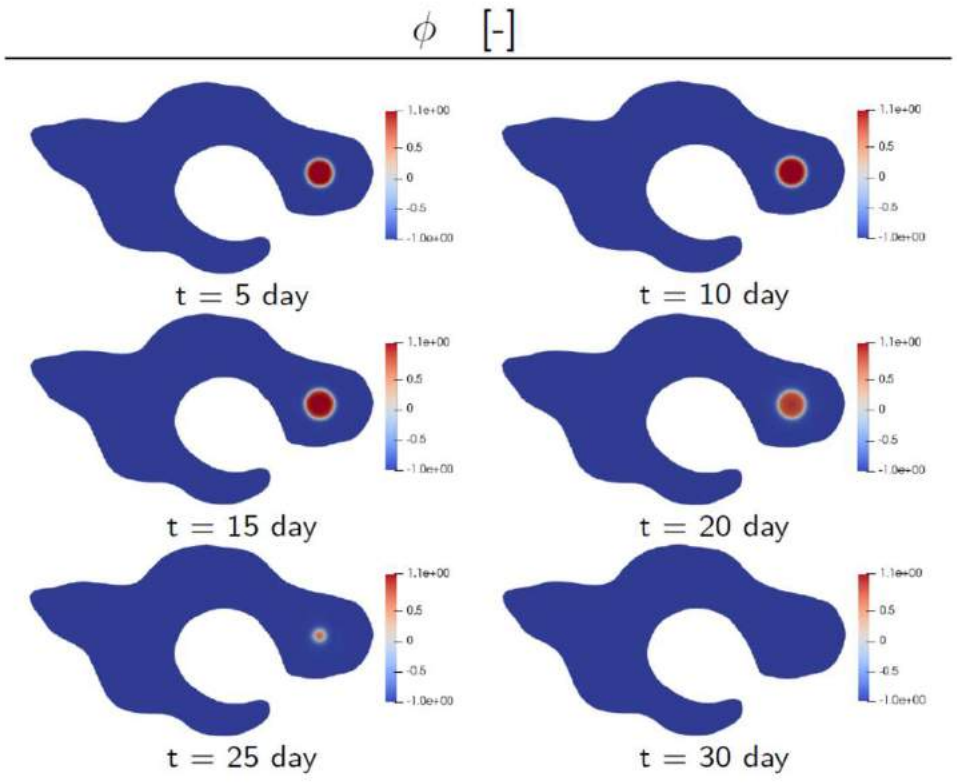

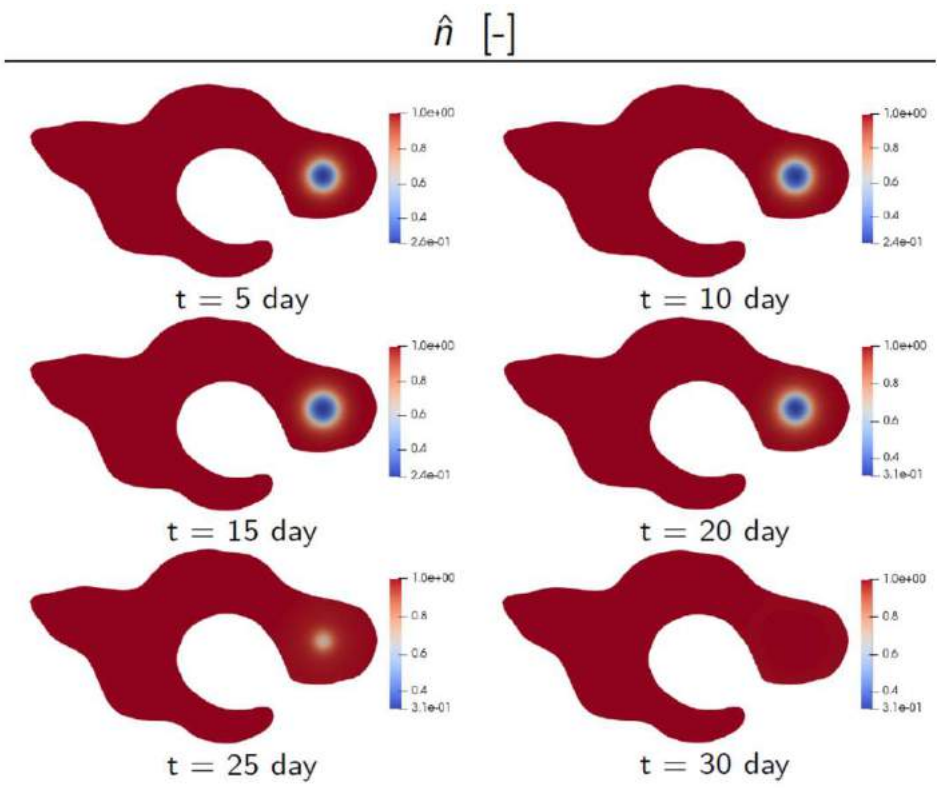

Simulation results: lymphocytes dynamics

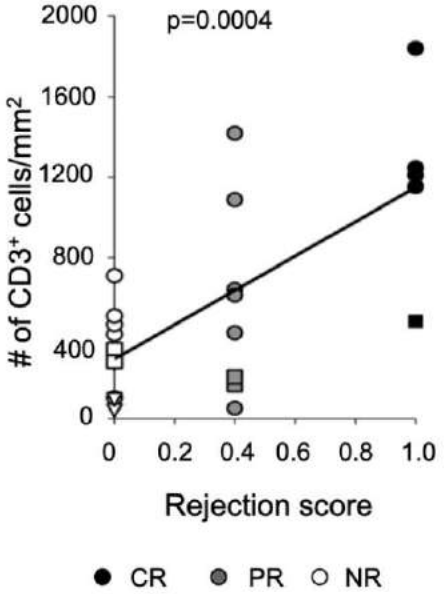

Cell concentration in cell/mm^3:

$$\rightarrow L_i = \frac{L_{PR}}{d_L} = 4{\cdot}10^4 \text{ - } 6{\cdot}10^4 \text{ cells/mm}^3$$

where L_{PR} is the PR cell concentration and d_L is the cell diameter.

L [cell/mm^3]

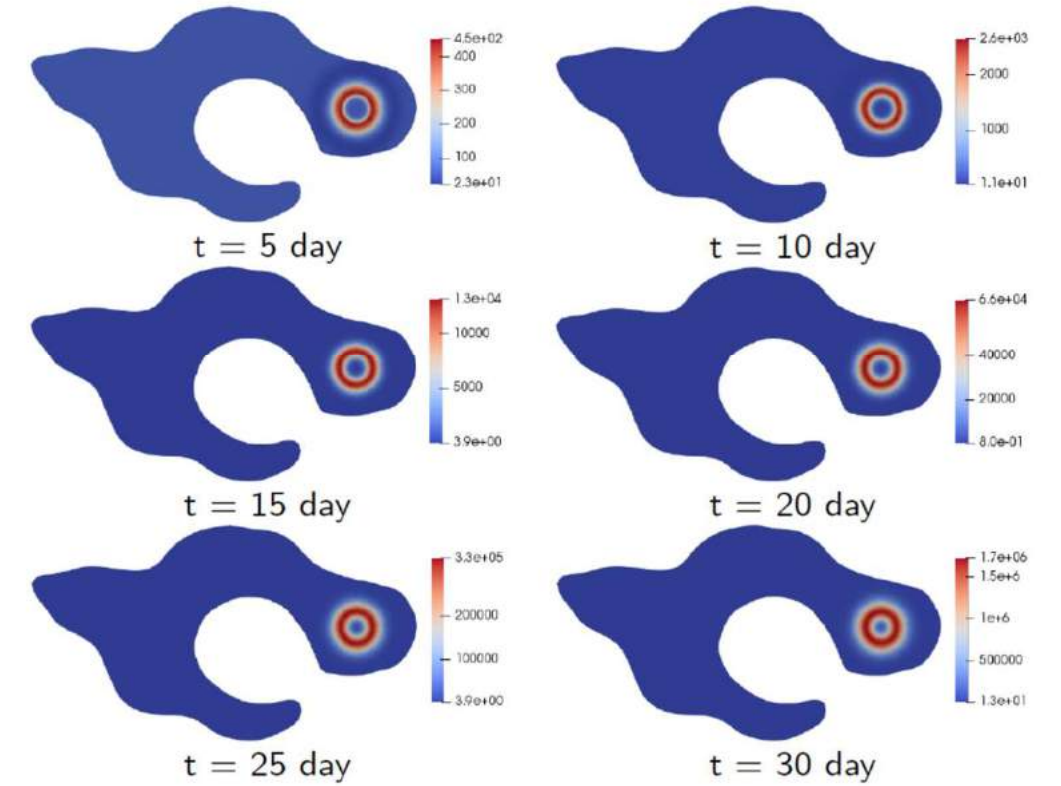

Evalutating the efficiency of immunotherapy

day	no therapy	immunotherapy	immunotherapy + host conditioning
5	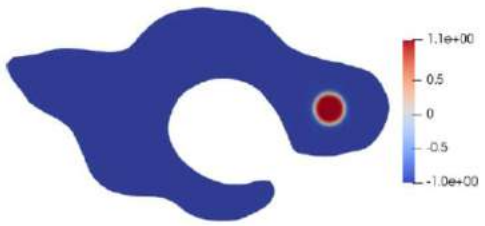	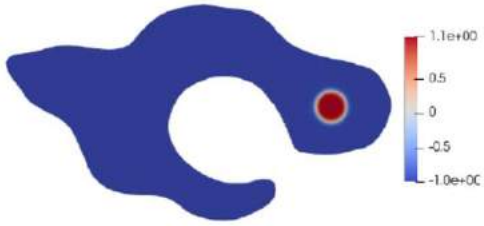	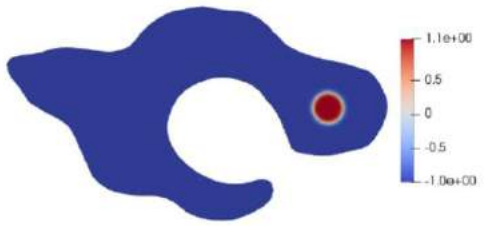
10	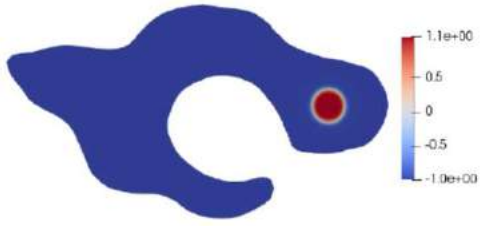	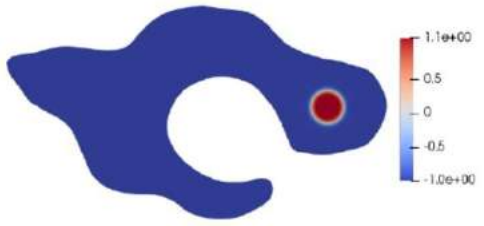	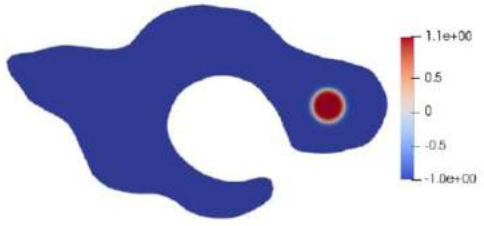
20	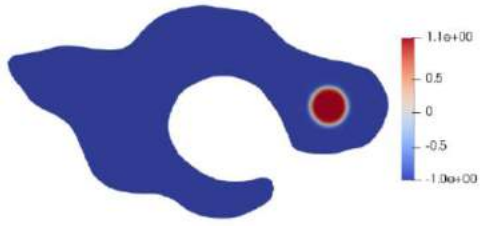	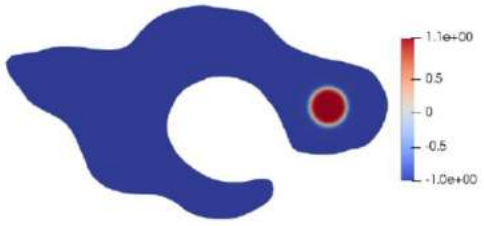	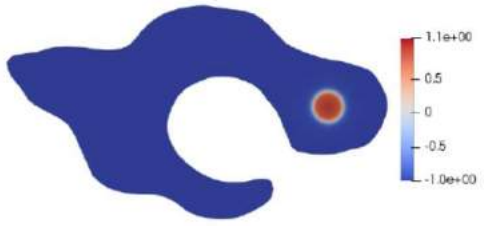
30	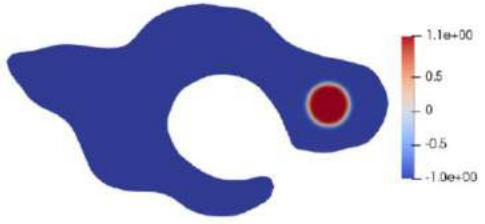	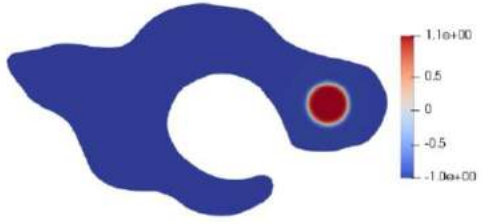	

Table 4: Axial slices representing tumor evolution in time within different therapeutic scenarios.

Simulation results: the threshold effect on L

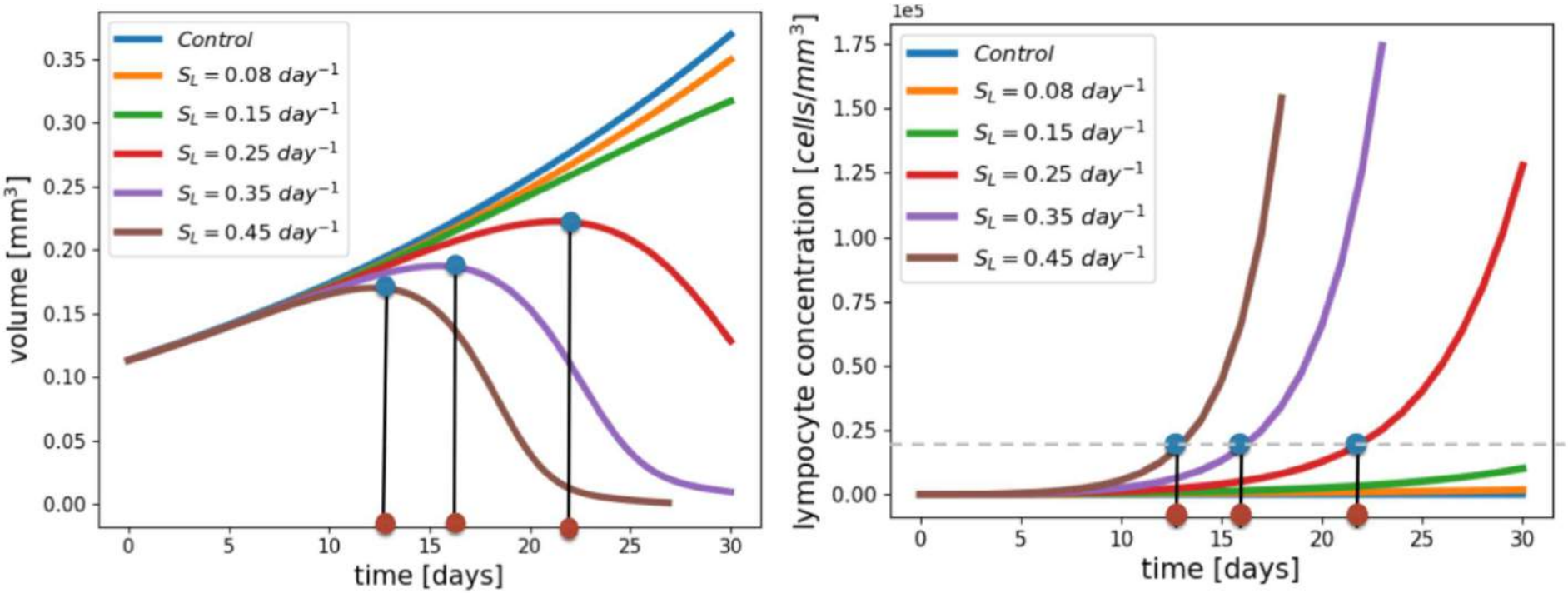

Figure 6: Temporal evolution of the tumor volume (left) and of the associated maximum value of lymphocytes concentration (right) for distinct therapeutic scenarios: (blue) the free growth in absence of therapy, (orange-green) immunotherapy only - case a) and (red-purple-brown) host conditioning strategies in addition to immunotherapy - case b), with the corresponding values of S_L shown in the legend. The blue circles indicate the curve values at the initial times (red circles) of growth inversion.

Future developments

Further developments can be:

- include more than one tumor mass and remove the spherical-shape approximation;
- include possible preferential direction in tumor expansion;
- model the lymphocytes growth saturation;
- more accurate validation using future experimental data;
- include data on lymphocytes tracking to evaluate the therapy level of toxicity.

Acknowledgements

Collaborators:

Giulia Pozzi **MOX**, Politecnico di Milano
Paolo Zunino
Beatrice Grammatica

Anna Mondino, Linda Chaabane **San Raffaele Hospital**, Milan


Contents lists available at ScienceDirect

Journal of Theoretical Biology

journal homepage: www.elsevier.com/locate/yjtbi

ELSEVIER

T cell therapy against cancer: A predictive diffuse-interface mathematical model informed by pre-clinical studies

G. Pozzi [a], B. Grammatica [a], L. Chaabane [b], M. Catucci [c], A. Mondino [c], P. Zunino [a], P. Ciarletta [a,*]

Funding

MFAG AIRC Grant, INSERM CancerPhysics
MIUR PRIN 2017 + PRIN 2020 + Dipartimento di Eccellenza 2023-2027
Regione Lombardia, NEWMED project

RegioneLombardia

Inserm
Institut national de la santé et de la recherche médicale

Fondazione CEN CentroEuropeo Nanomedicina

GNFM INdAM

AIRC